

Phase coherence and spin squeezing in a two component Bose-Einstein condensate

Dissertation Submitted to
the Department of Engineering Physics
and the committee on graduate studies
of **Tsinghua University**
in partial fulfillment of the requirements
for the degree of
Doctor of Philosophy

Yifan Li
September, 2021

Supervised by

Prof. Dr. Chuanxiang Tang

Prof. Dr. Li You

Prof. Dr. Philipp Treutlein

Dr. Tilman Zibold



A Ph.D dissertation carried out at Tsinghua University and University of Basel
under support of Chinese Scholarship Council

公开评阅人和答辩委员会名单

公开评阅人名单

张文献	教授	武汉大学
吕嵘	教授	清华大学

答辩委员会名单

主席	易俗	教授	中国科学院理论物理研究所
委员	唐传祥	教授	清华大学
	张熙博	研究员	北京大学
	吕嵘	教授	清华大学
	郑盟锟	副教授	清华大学
	刘永椿	副教授	清华大学
秘书	杨硕	副教授	清华大学
	黄馨瑶	助理研究员	清华大学

摘要

原子干涉仪在精密物理量测量中具有广泛的应用。内态原子干涉仪的测量精度受到其演化时长的限制，而后者取决于原子的相干时间，因此探究原子系综中的退相干机制十分重要。同时，内态干涉仪的相位灵敏度还会受到系统中粒子数的限制，例如对于使用 N 个不关联粒子的干涉仪，其相位灵敏度极限为 $\Delta\phi = 1/\sqrt{N}$ ，即标准量子极限（SQL），实验上可以利用自旋压缩等资源来超越标准量子极限。

本文的工作基于在原子芯片上制备的铷 87 原子的玻色爱因斯坦凝聚体（Bose-Einstein condensate），并使用两个超精细基态能级 $|F = 1, m_F = -1\rangle$ 和 $|F = 2, m_F = +1\rangle$ 作为干涉仪的两个模式。这样一个双分量的玻色爱因斯坦凝聚体系统非常适合研究原子系综内的退相干问题，以及多体系统中的量子纠缠。

我们在实验上利用拉姆齐干涉仪测量了这一系统中的相位相干性随着时间的衰减，发现相干性主要受限于碰撞相互作用引起的相移和原子随机损耗。我们建立了一个基于主方程的理论模型，并用蒙特卡罗波函数法求解，定量地证实了这一退相干机制。该理论模型考虑了系统中的碰撞相互作用、原子数的涨落和原子损耗的随机性，得到的理论结果与实验结果吻合良好。我们的结果阐明了双分量玻色爱因斯坦凝聚体中的退相干机制，也为进一步抑制系统中的原子退相干提供了一种思路。

本论文的另一个研究重点是制备可用于量子精密测量的纠缠态。我们在实验上研究了超冷原子系综中的自旋压缩。自旋压缩为量子干涉仪提供了资源，能够使其获得超出标准量子极限的相位灵敏度，同时也可以应用在量子信息和量子隐形传态等其他领域。在本文中，我们利用单轴扭曲机制来制备自旋压缩，获得了 $\xi^2 = -9.8(5)$ dB 的自旋压缩态，表明系统中有超过 128 个原子的纠缠深度。这个结果与我们系统以前的结果相比有了显著的改进，并且稳定可重复。通过提高压缩比，我们演示了超出标准量子限 7 dB 的拉姆齐干涉仪。此外，这一结果显示了我们的系统在进一步研究 Einstein-Podolsky-Rosen 悖论方面的潜力。我们的实验结果对于量子计量学实验、芯片原子钟的发展和多体纠缠的研究等均具有启发意义。

关键词：旋量玻色-爱因斯坦凝聚体；原子内态干涉仪；相位相干性；量子计量；自旋压缩

ABSTRACT

Atom interferometers find a broad range of applications in precision measurements of physical quantities. Their precision is limited by the finite coherence time of the atoms, which fundamentally restricts the interrogation time. Therefore, it is important to understand the limitations to the temporal coherence in the atomic ensembles. On the other hand, the measurement precision is bounded by the particle number in the interferometer, for example, for N uncorrelated atoms, the phase resolution is limited by the atomic projection noise to $\Delta\phi = 1/\sqrt{N}$, known as the standard quantum limit (SQL). This limit can be overcome by employing quantum resources such as spin squeezing.

In this work, we perform internal-state interferometry with Bose-Einstein condensates (BEC) of Rubidium 87 atoms prepared on an atom chip. We use two hyperfine ground states $|F = 1, m_F = -1\rangle$ and $|F = 2, m_F = +1\rangle$ as the two modes of interferometer. Our experimental system (a two-component BEC) is ideally suited to experimentally addressing the questions about the decoherence mechanisms in the BEC, and provides a versatile and powerful platform for generating entanglement between atoms.

Using Ramsey interferometry we measure the temporal decay of coherence in this system and observe that the coherence is limited by the interplay of the collisional phase shift and the stochastic nature of atom loss. We verify the mechanism quantitatively by building a theoretical model based on a master equation and performing numerical simulation with the Monte Carlo wave-function method. Our model takes into account collisional interactions, atom number fluctuations and losses in the system, and it leads to theoretical results in good agreement with experimental results. Our results reveal the fundamental limit of phase coherence in this system and provide a starting point for future studies towards suppressing the decoherence in BECs.

Another focus of this thesis is the generation of metrologically useful entangled states. We experimentally study a special type of entanglement, the spin squeezing, in atomic BECs, and use the one-axis twisting mechanism to prepare spin-squeezed states. Spin squeezing provides a resource for the quantum interferometer to achieve a phase uncertainty beyond the SQL, and is also useful resource for application in quantum information. We present spin squeezed states with a Wineland spin-squeezing parameter of up to $\xi^2 = -9.8(5)$ dB, indicating an entanglement depth of more than 128 atoms in the

ABSTRACT

system. This result is improved significantly compared to previous results in our system. The improved spin squeezing in the system allows us to demonstrate a Ramsey interferometer operating 7 dB beyond the SQL. Furthermore, the reproducibly high level of spin squeezing shows the promising potential of our system to further investigate the Einstein–Podolsky–Rosen paradox with BECs. Our experimental results are relevant for experiments in quantum metrology, the development of chip-based atomic clocks, and further studies of many-body entanglements.

Keywords: two-component Bose-Einstein condensate; Ramsey interferometer; phase coherence; quantum metrology; spin squeezing

CONTENTS

摘要.....	I
ABSTRACT.....	II
CONTENTS.....	IV
CHAPTER 1 INTRODUCTION.....	1
CHAPTER 2 TWO COMPONENT BOSE-EINSTEIN CONDENSATE.....	5
2.1 Fundamentals of BECs.....	6
2.1.1 The occurrence of BEC.....	6
2.1.2 The Gross-Pitaevskii equation.....	8
2.1.3 Thomas-Fermi Limit.....	11
2.2 Two-component BEC.....	11
2.2.1 Ground states.....	13
2.2.2 Breathing dynamics.....	13
2.3 Collective spin description.....	14
2.3.1 Pseudo-spin description.....	14
2.3.2 Coherent spin dynamics.....	18
2.3.3 Quasi-probability distribution.....	19
2.3.4 Examples of collective spin states.....	20
2.4 Phase coherence in a Bose-Einstein Condensate.....	23
2.4.1 Spatial coherence.....	23
2.4.2 Temporal coherence.....	24
2.5 Quantum metrology.....	26
2.5.1 Standard quantum limit.....	26
2.5.2 Entanglement enhanced interferometer.....	27
2.5.3 Strategies of preparing non-classical correlations.....	28
CHAPTER 3 EXPERIMENTAL SYSTEM.....	30
3.1 Overview of the apparatus.....	30
3.1.1 Vacuum chamber.....	30
3.1.2 Atom chip.....	31

CONTENTS

3.1.3 Laser system	33
3.1.4 Current sources and their noise characterization.....	36
3.1.5 Microwave and radio-frequency electronics.....	39
3.2 Preparation of a ^{87}Rb Bose-Einstein Condensate on an atom chip	41
3.3 Manipulation of atoms	44
3.3.1 Theory of atom-field interaction	45
3.3.2 Rabi Oscillations	50
3.3.3 State-dependent potential	53
3.4 Precise detection of atom numbers.....	55
3.4.1 Imaging systems.....	55
3.4.2 Absorption Imaging.....	55
3.4.3 Image acquisition and fringe removal.....	56
3.4.4 Calibration of the imaging system	58
3.4.5 Detection Noise.....	60
CHAPTER 4 LIMIT OF PHASE COHERENCE IN A TWO-COMPONENT BEC .	62
4.1 Atom losses in a two-component BEC	63
4.1.1 Atomic collisions.....	63
4.1.2 Density-dependent losses	64
4.1.3 Atom loss coefficient measurement	66
4.2 Measurement of the phase noise.....	69
4.2.1 Visibility and contrast.....	69
4.2.2 Calculation of phase noise	73
4.3 Noise analysis.....	75
4.3.1 Intrinsic noise	75
4.3.2 Technical noise	81
4.4 Simulation via Monte Carlo wave-function method.....	83
4.4.1 Master equation in a stochastic formulation.....	84
4.4.2 Semi-stationary solution.....	85
4.4.3 Scattering length.....	88
4.5 Comparison of experiment and theory.....	88
CHAPTER 5 NON-CLASSICAL RAMSEY INTERFEROMETER	92
5.1 Preparation of spin-squeezed state	92
5.1.1 One-axis twisting Hamiltonian	93

CONTENTS

5.1.2 Sequence to prepare the spin-squeezed state	93
5.1.3 Spin demixing-remixing dynamics	95
5.2 Characterization of spin-squeezing	98
5.2.1 Spin-squeezing parameters.....	98
5.2.2 Squeezing Tomography	100
5.2.3 Entanglement in spin-squeezed states	102
5.3 Exploration towards better spin squeezing.....	104
5.3.1 Microwave potential configurations	104
5.3.2 Relaxed trapping potential	107
5.3.3 Spin-Echo technique	109
5.3.4 Atom number stability	110
5.3.5 Summary	110
5.4 Non-classical interferometer with a spin-squeezed state	111
CHAPTER 6 CONCLUSIONS AND OUTLOOKS.....	113
6.1 Conclusions	113
6.2 Outlook	114
6.2.1 Control of the phase coherence with state-dependent potential.....	114
6.2.2 EPR entanglement between two spatially separated BECs.....	115
BIBLIOGRAPHY	118
APPENDIX A TYPICAL TRAPS ON ATOM CHIP	126
APPENDIX B ENTANGLEMENT DEPTH	130
ACKNOWLEDGEMENTS	132
声 明.....	136
个人简历、发表的学术论文与科研成果.....	137
指导教师学术评语.....	138
答辩委员会决议书.....	139

CHAPTER 1 INTRODUCTION

Quantum interference, one of the most fundamental and challenging principles in quantum mechanics, forms the basis of high-precision measurement and quantum information processing. Interferometry is widely used in different fields, especially when measuring precisely physical quantities, such as the strength of a field or time, which is important for both fundamental science and engineering. In a typical interferometer, particles from a single source are split into two paths that travel in different paths (or modes) and the physical quantity of interest is mapped onto a phase difference accumulated between the two paths (modes). This phase difference is later determined by the interference fringes produced after the two paths are recombined. This conceptual working scheme applies for different types of interferometers: from the Laser Interferometer Gravitational-wave Observatory (LIGO)^[1] where laser (photons) are used, to atomic clocks^[2] where atoms interfere.

Atom interferometers based on ultracold atoms, particularly Bose-Einstein condensates (hereafter abbreviated as BEC), are of special interest thanks to the well-developed techniques for trapping and controlling neutral atoms. In this thesis, I present works mainly related to internal-state atomic interferometer using a BEC trapped in a magnetic potential on an atom chip^[3]. The atom chip provides a good platform for the atomic interferometer since it offers the possibility of precise manipulation of neutral atoms close to the chip surface^[4]. Two internal (spin) states of ^{87}Rb atoms are used as interferometric modes, and they are split and recombined using two-photon microwave and radio frequency Rabi pulses^[5-6]. Such a two-component BEC has a lot of interesting properties and provides a promising platform for quantum metrology^[7] as well as other quantum technologies, with all internal and motional degrees of freedom of the atoms under experimental control at the quantum level.

Understanding the limit of the measurement precision of the internal interferometer and improving it is always the most interesting and challenging topic in this discipline. Phase coherence is of primary importance to perform interferometers since its finite duration poses fundamental limitations on the possible interrogation time for interferometers. In addition, understanding these phase property is essential for experiments that make use of a BEC as a source of coherent matter waves, for example the “atom laser” ex-

periments^[8-9] and the atomic clocks with BEC^[6]. For these reasons, investigating the fundamental limits of phase coherence in a two-component BEC is of crucial importance for the internal state interferometer. Moreover, in the experiments exploring the many body entanglement using BEC, phase noise during the state preparation affects the fidelity of the prepared non-classical states. Due to these reasons, phase coherence in a BEC has attracted a lot of research interest. A considerable attention has been given to this topic and theoretical studies point out different decoherence mechanisms, while some long standing predicted decoherence is not reported experimentally.

Our experimental system is well suited for investigating the decoherence mechanism because the relative phase between different components becomes easily observable from interference measurements. In addition BEC as a nearly isolated system, allows us to investigate the decoherence intrinsic to the system, rather than arising from the interactions with the environment. We take the advantage of such a two-component BEC and investigate the phase uncertainty as a function of time. We find the dominant decoherence is due to the interplay between the elastic atomic collisions and the random nature of the atom losses. The mechanism is confirmed quantitatively by building a theoretical model based on a master equation and numerically solving it with the Monte-Carlo wave function method. The results of the associated studies are published in Ref. [10].

Besides phase coherence, the phase uncertainty of a two-mode interferometer is also limited by the quantum projection noise due to the fundamental randomness of the measurement outcomes on superposition state. Performing with N uncorrelated or classically correlated atoms, the measurement precision can only reach the standard quantum limit (SQL), equal to $1/\sqrt{N}$ ^[11]. This is a classical limit and can be overcome using resources of quantum correlations such as spin squeezing. With finite resources such as a given particle numbers N , one important goal is to go beyond the SQL, which is the main task of quantum metrology. Quantum metrology “studies how to exploit quantum resources, such as squeezing and entanglement to overcome this classical bound (SQL)”^[7]. Extensive researches have been carried out on quantum enhanced interferometer based upon different systems, such as photon polarization entanglement^[12-13], the trapped-ion internal entanglement^[14-15], and neutral atoms^[16-19]. Non-classical states of atomic ensembles, have been proposed in 1993^[20], immediately found applications in quantum technologies as an essential resource for quantum metrology such as atomic clocks^[21-26] and interferometers to measure the magnetic field beyond the classical limit^[19]. Apart from the potential ap-

plications on metrology, entanglement, as a fundamental concept of quantum physics^[27], still presents many fundamental challenges, in particular when applied to many-body systems of indistinguishable particles.

In our system, we explore spin-squeezed states^[20], a special kind of entanglement states known as useful resources for quantum metrology. We create spin squeezing through one axis twisting (OAT) dynamics^[20]. This non-linear interaction naturally arises in our system due to elastic collisions between the atoms^[28]. A key feature of our experiment is that we can make use of a state-dependent potential to effectively turn on the nonlinear interaction by spatially separating the two states and turn it off when they are recombined^[29]. However, it is always complicated to engineer the entanglement in a many-body system, and optimization of the experiment is desired. Part of the achievements of this thesis is that a more reliable and better level of spin squeezing is realized due to the improvements of the experiment on several aspects. Apart from several technical improvements and the optimization of the routine for the preparation of spin squeezing, we have also gained a better understanding of the squeezing mechanisms in the system. With these improvements, we create spin-squeezed states with a Wineland spin squeezing parameter^[11] of up to $-9.8(5)$ dB compared to a classical state and realize an entanglement-enhanced interferometer with a sensitivity of 7 dB in variance below to SQL. The sub-SQL sensitivity is maintained for an interrogation time up to 20 ms. Afterwards the previously mentioned limit of phase coherence emerges and finally destroys the entanglement.

In this thesis, we present experimental research on two component BECs from two aspects. We investigate the temporal phase coherence in this system and clarify the fundamental limit of it, the experiments presented help to deepen the understanding of the phase coherence in a many-body system. We also prepare a spin-squeezed state, and demonstrate non-classical Ramsey interferometry using the spin squeezed state as input. The experiments were carried out at the university of Basel in Switzerland with the support from Chinese Scholarship Council.

The thesis is structured in the following way. In chapter 2, we will introduce some fundamental concepts in the field of two-component BEC, discuss the collective spin description of a many-body system and give a general introduction to quantum metrology. In chapter 3, we present the experimental apparatus in detail and discuss the experimental techniques for manipulating the internal and external states of the atoms. In chapter 4, we present the experimental and theoretical study of the phase coherence in the system, ana-

lyze the phase noise and point out the main decoherence mechanism. chapter 5 presents the strategies of preparing and improving the spin squeezing in our system, and demonstrate a non-classical interferometer with a phase sensitivity beyond the SQL by 7 dB. Finally chapter 6 concludes the thesis and gives an outlook of on-going and potential future works in our experiment.

CHAPTER 2 TWO COMPONENT BOSE-EINSTEIN CONDENSATE

In atomic physics, Bose-Einstein condensate (BEC) is an interesting state of matter which is formed when a gas of bosons at low density is cooled to a temperature very close to absolute zero. Under such condition, a large fraction of bosonic atoms condense into the same single-particle state. The phase transition to BEC is of great significance since it provides a powerful technique to amplify and to observe the microscopic quantum mechanical phenomena, particularly wave function interference.

BEC phase transition was first predicted in 1925 by Albert Einstein and Satyendra Nath Bose^[30]. In 1995, BEC was realized in dilute gases of alkali atoms, first reported in a single internal state of rubidium^[31], later in single state of sodium^[32] and lithium^[33]. Since then BEC has been the subject of intense research developing rapidly under the combined support of laser cooling^[34-35], magnetic trapping and evaporative cooling^[36] of atoms. The first BEC experiments involving multiple hyperfine species were performed with atoms in the $|F = 1, m_F = -1\rangle$ and $|F = 2, m_F = 2\rangle$ internal states of ^{87}Rb ^[37]. Their experiments demonstrated the possibility of producing long-lived condensate systems in superposition of different internal states, and that the low temperature behaviors of the ground state atoms in the two spin states are different. Later, experiments using magnetically trapped two-component BECs with atoms in states $|F = 1, m_F = -1\rangle$ and $|F = 2, m_F = 1\rangle$ were demonstrated^[5,38]. At about the same year, BEC trapped in magnetic traps on atom chips was realized^[39] and soon attracted great attention and triggered a rapid growth of the field of chip based experiments^[3,5-6,29,40].

In this thesis, the phenomenon of BEC is not itself studied in detail, but rather used as a tool for exploring the physics in many-body systems. Specially, in our experiment, the internal (spin) degree of freedom is introduced to the BEC, atoms are allowed to occupy two hyperfine energy levels. Such a two-component BEC has a lot of interesting properties and provides promising testing ground for quantum metrology and other quantum technologies, with all internal and motional degrees of freedom of the atoms under unprecedented control at the quantum level.

This chapter starts by introducing some general concepts that are fundamental to our understanding of the BEC in the dilute atomic alkali gases, including the definition and

critical temperature of a BEC, the effective interatomic potential in an interacting system, the time-independent and time-dependent Gross-Pitaevskii equations and the Thomas-Fermi limit. Then from section 2.2, a two-component BEC containing two coexisting hyperfine species, which is used in our experiments, will be discussed in detail. The coupled Gross-Pitaevskii equation and its application in our system is discussed; the collective spin description of the system is introduced in section 2.3; and previous studies about phase coherence are summarized in section 2.4. In the end, the basic concepts of quantum metrology are introduced in section 2.5.

2.1 Fundamentals of BECs

The phenomena of BEC have been extensively studied over the past two decades both theoretically and experimentally^[41-42]. In this section, we shall only present some basic results that are of use for later chapters in this thesis in order to give an intuitive description of BEC.

2.1.1 The occurrence of BEC

An intuitive and simple picture of the BEC phase transition can be obtained from the quantum wave nature of particles. Ideal bosons undergo BEC phase transition when the spatial extent of the wave packet of individual boson, described by the thermal de Broglie wavelength, starts to overlap with each other. For a uniform three-dimensional gas consisting of non-interacting particles in the thermodynamic limit, the de Broglie wavelength λ_{th} at a temperature T is defined as:

$$\lambda_{\text{th}} = \frac{\hbar}{\sqrt{2\pi m k_B T}}, \quad (2.1)$$

where \hbar is the Planck constant, k_B is the Boltzmann constant, and m is the mass of each boson. This wavelength depends on the temperature, and increases when the system is cooled down. The BEC occurs when the temperature is low enough so that λ_{th} is on the order of the interparticle distance $n^{-1/3}$, where n is the particle density. In more accurate words, BEC phase transition occurs when quantity $n\lambda_{\text{th}}^3$ (referred to as the *phase-space density*) satisfies

$$n\lambda_{\text{th}}^3 = \zeta\left(\frac{3}{2}\right) \approx 2.6124, \quad (2.2)$$

where $\zeta(\cdot)$ being the Riemann zeta function. At this point, the *quantum degeneracy* sets in and the quantum effects become significant. The corresponding transition temperature

T_c is referred to as *critical temperature* and is given by

$$T_c = \left(\frac{n}{\zeta(3/2)} \right)^{2/3} \frac{2\pi\hbar^2}{mk_B} \approx 3.3125 \frac{\hbar^2 n^{2/3}}{mk_B}, \quad (2.3)$$

The BEC phase transition can also be understood from the quantum statistics point of view. In a system, N bosons are distributed over p accessible momentum states, and obey the Bose-Einstein rule that the occupation number of any single-particle state is not restricted. The phase transition to BEC in a system of bosons occurs when at least one of these single-particle states is *macroscopically occupied*, *i.e.*, its occupation number N_0 is of order N . At this point the degeneracy condition $p \ll N$ is satisfied. As the temperature of the ensemble determines the accessible number of states, by cooling down the particles in the system to $T < T_c$, bosons can condense to a single particle wave function. In the ideal case, the temperature is $T = 0$, the complete gas of bosonic particles is then fully condensed $N_0 = N$ with all particles occupying an identical single-particle wave function. However, given that the absolute zero of temperature cannot be reached, the fraction of atoms that are condensed in the ensemble is given by

$$\frac{N_0}{N} = 1 - \left(\frac{T}{T_c} \right)^3. \quad (2.4)$$

As suggested by Eq. (2.3), the critical temperature depends strongly on the density of particles, which is in turn determined by the trapping potential. In our experiment, rubidium-87 (^{87}Rb) atoms are confined in a magnetic trap which can be regarded as harmonic with the quadratic form $V = m(\omega_x^2 x^2 + \omega_y^2 y^2 + \omega_z^2 z^2)/2$. In this case, the critical temperature T_c from Eq. (2.3) becomes

$$T_c^0 = \frac{\hbar\omega_{\text{ho}}}{k_B} \left(\frac{N}{\zeta(3)} \right)^{1/3} \approx 4.5 \left(\frac{\omega_{\text{ho}}/2\pi}{100 \text{ Hz}} \right) N^{1/3} \text{ nK}, \quad (2.5)$$

where $\omega_{\text{ho}} = (\omega_x \omega_y \omega_z)^{1/3}$ is the geometric mean of the trap frequencies.

It is noteworthy that Eq. (2.5) only holds in the case of the thermodynamic limit, *i.e.*, the atom number N is macroscopic and the size of the volume of the system is infinite. However, in a realistic case, the thermodynamic limit cannot be really reached since the number of atoms in the harmonic trap is not truly macroscopic (so far BEC experiments have been carried out with a maximum number of about 10^7 atoms). In addition, there are interatomic interactions, which is also expected to reduce the condensate fraction and thus lower the transition temperature as compared to Eq. (2.5). A more accurate transition temperature for our experimental situation is given by introducing correction terms taking

into account these effects, which results in the expression^[43]

$$T_c \simeq \left(1 - 0.73 \frac{\omega_a}{\omega_{\text{ho}}} N^{-1/3} - 1.33 \frac{a_s}{a_{\text{ho}}} N^{1/6} \right) T_c^0, \quad (2.6)$$

where $\omega_a = (\omega_x + \omega_y + \omega_z)/3$ is the arithmetic mean of the trapping frequencies, a_s is the scattering length characterizing the s -wave interaction strength, and $a_{\text{ho}} = (\hbar/m\omega_{\text{ho}})^{1/2}$ is the harmonic oscillator length scale. In Eq. (2.6) the term proportional to $N^{-1/3}$ accounts for finite number of atoms, while the term proportional to $N^{1/6}$ corrects for the effect of interactions. As an example for our typical experimental parameters, $N = 1000$ atoms in a trap of frequencies $2\pi \times (114, 714, 714)$ Hz, we find $T_c \simeq (1 - 0.0982 - 0.0162) 174.31 \text{ nK} \approx 154.4 \text{ nK}$. From this we note that the finite-size correction contributes approximately six times larger than the interaction corrections, and together they result in a reduction of the transition temperature by 11%.

2.1.2 The Gross-Pitaevskii equation

Throughout this work, we model our BEC as “zero temperature”, since the number of non-condensed particles is much smaller than the number of condensed particles, and any thermal excitation can be ignored. This implies that the temperature must be low enough with respect to the critical temperature, which is confirmed experimentally. For our typical experimental parameters, there is no thermal fraction observed. To clarify, the imaging system is capable of observing such thermal fractions if one creates a BEC with a higher temperature on purpose.

For discussion convenience, in this section we only consider cases in which the hyper-fine degree of freedom can be ignored. We thus consider a system of N identical spinless bosons characterized by spatial coordinates \mathbf{r}_i ($i = 1, 2, \dots, N$) with some arbitrary inter-particle interactions and subject to some external potential confining the particles in some finite region of space. The many-body wave function is written as $\Psi_N(\mathbf{r}_1 \mathbf{r}_2 \dots \mathbf{r}_N)$, symmetric under the exchange of any two particle coordinates. In interacting gases a rigorous description for the BEC is then given by the many-body ground-state wave function Ψ_N solving the Schrödinger equation of the system, with the many-body Hamiltonian given in second quantization form^[41]

$$\hat{H} = \int d\mathbf{r} \hat{\Psi}^\dagger(\mathbf{r}) \left(-\frac{\hbar^2}{2m} \nabla^2 + V(\mathbf{r}) \right) \hat{\Psi}(\mathbf{r}) + \frac{1}{2} \int d\mathbf{r} d\mathbf{r}' \hat{\Psi}^\dagger(\mathbf{r}) \hat{\Psi}^\dagger(\mathbf{r}') U(\mathbf{r}-\mathbf{r}') \hat{\Psi}(\mathbf{r}') \hat{\Psi}(\mathbf{r}), \quad (2.7)$$

where $\hat{\Psi}(\mathbf{r})$ and $\hat{\Psi}^\dagger(\mathbf{r})$ are the boson field operators that annihilate and create a particle

at the position \mathbf{r} , respectively, $-\frac{\hbar^2}{2m}\nabla^2$ describes the kinetic energy of the atoms, $V(\mathbf{r})$ describes the confinement potential and $U(\mathbf{r}' - \mathbf{r})$ is the two-body interatomic interaction. The ground state of the system, as well as its thermodynamic properties, can be directly calculated starting from the Hamiltonian Eq. (2.7).

However, finding such solution is in general extremely complicated. An important simplification of the problem results from simplifying the atom-atom interactions by neglecting all $l \neq 0$ partial waves and only considering spherically symmetric s -wave collisions characterized by the s -wave scattering length a_s . This simplification can be taken under the condition that the gas is cold and dilute, *i.e.*, low temperature and low densities, as in our experiments where we use BEC of ^{87}Rb at a few hundreds of nano kelvin). In this regime, this approximation is valid since the thermal de Broglie wavelength is much larger than the effective range of the interatomic (van der Waals) potentials. Therefore, the true interaction potential of two atoms may be replaced by an effective contact interaction in the form of a delta function,

$$U(\mathbf{r}' - \mathbf{r}) = \frac{4\pi\hbar^2 a_s}{m} \delta(\mathbf{r}' - \mathbf{r}) = g\delta(\mathbf{r}' - \mathbf{r}), \quad (2.8)$$

where a_s is the s -wave scattering length, m is the mass of the atoms, and g is referred to as the coupling strength. For ^{87}Rb , the interactions are repulsive with $a_s \approx 5$ nm.

Another important approximation that greatly simplifies the complex problem of pairwise interactions is obtained by the Hartree-Fock ansatz (referred as the mean field approximation in case of BEC at zero temperature). It assumes that the many-body wave function is a product of the same single-particle wave functions and neglects any excitations ($T=0$).

$$\Psi_N(\mathbf{r}_1, \dots, \mathbf{r}_N) = \prod_{i=1}^N \phi(\mathbf{r}_i) \quad (2.9)$$

where $\phi(\mathbf{r}_i)$ are the normalized single-particle wave functions of the confining potential. Thus the atomic density is $n(\mathbf{r}) = |\Psi(\mathbf{r})|^2$, satisfying the normalization $\int |\Psi(\mathbf{r})|^2 d\mathbf{r} = N$. This ansatz together with the consideration of the effective interaction potential, result in the Gross-Pitaevskii equation (GPE):

$$\left[-\frac{\hbar^2}{2m}\nabla^2 + V(\mathbf{r}) + g(N-1)|\phi(\mathbf{r})|^2 \right] \phi(\mathbf{r}) = \mu\phi(\mathbf{r}), \quad (2.10)$$

where $g(N-1)|\phi(\mathbf{r})|^2$ describes the interaction between atoms. For any particle, the effect of the interaction with all other $N-1$ particles takes the form of an extra potential energy that scales with the atomic density $|\phi(\mathbf{r})|^2$, and is independent of the details of the

pairwise interaction but only characterized by the effective interaction strength g . On the right hand side of the equation, there is μ which is equal to $\delta\langle H\rangle_N/\delta N$. It is noteworthy that μ is not the energy per particle $\langle H\rangle_N/N$, rather the energy needed to remove a single particle from the BEC, *i.e.*, the chemical potential.

In the literature, it is common to rewrite the single particle equation Eq. (2.10) in terms of the order parameter defined by $\Psi(\mathbf{r}) = \sqrt{N}\phi(\mathbf{r})$. And since a BEC usually contains more than 10^3 atoms in our experiment, the difference between $N - 1$ and N can be neglected, it then yields

$$-\frac{\hbar^2}{2m}\nabla^2\Psi + V\Psi + g|\Psi|^2\Psi = \mu\Psi, \quad (2.11)$$

where the order parameter is normalized so that $\int |\Psi(\mathbf{r})|d\mathbf{r} = N$. Eq. (2.11) is strictly equivalent to the single particle GPE Eq. (2.10). The order parameter, apart from its normalization, is actually the single-particle wave function which the Bosons are condensed into. Although the order parameter itself possesses a well defined phase, this overall phase of the wave function has no physical significance in the stationary case, unless the internal state degree of freedom is introduced in which case the relative phase between its hyperfine components becomes a quantity of physical significance.

To describe dynamical behaviours, we need to consider the time-dependent version of the many-body wave function $\Psi_N(\mathbf{r}_1, \dots, \mathbf{r}_N, t) = \prod_{i=1}^N \phi(\mathbf{r}_i, t)$, or the time-dependent order parameter $\Psi(\mathbf{r}, t) = \sqrt{N(t)}\phi(\mathbf{r}, t)$, where $\phi(\mathbf{r}, t)$ is the single particle wave function. The time-dependent GPE can be derived by substituting this ansatz into the time-dependent many-body Schrödinger equation. We then have the time-dependent version of the Eqs. (2.10) and (2.11), in form of the single-particle wave function or the order parameter

$$i\hbar\frac{\partial}{\partial t}\phi(\mathbf{r}, t) = \left[-\frac{\hbar^2}{2m}\nabla^2 + V(\mathbf{r}) + g(N-1)|\phi(\mathbf{r}, t)|^2 \right] \phi(\mathbf{r}, t). \quad (2.12)$$

$$i\hbar\frac{\partial\Psi(t)}{\partial t} = -\frac{\hbar^2}{2m}\nabla^2\Psi(t) + V\Psi(t) + g|\Psi(t)|^2\Psi(t). \quad (2.13)$$

Unlike the time-independent GPEs, the two versions of the time-dependent GPE Eqs. (2.12) and (2.13) are not strictly equivalent unless the atom number N is conserved over time. Therefore Eq. (2.13) implies Eq. (2.12), but not vice versa. In this chapter we only consider the dynamics on short time, so that atom losses from the BEC can be neglected. However if we care for the long time dynamics, atom losses cannot be neglected and have to be accounted for. The corresponding GPE which includes atom losses will

be introduced later in chapter 4.

From the fact that the time evolution of the stationary wave function is $\phi(\mathbf{r}, t) = \phi(\mathbf{r})e^{i\theta(t)}$, we can see from the Eqs. (2.10) and (2.12) that the time evolution of the wave function is actually governed by the chemical potential

$$\phi(\mathbf{r}, t) = \phi(\mathbf{r})e^{-i\mu t/\hbar}. \quad (2.14)$$

This reflects the fact that interactions, which are included in μ by the GPE mean-field description, influence the time evolution of the phase.

GPEs provide a very convenient way for numerical calculations of the stationary solution and the dynamical behaviours. It has been applied extensively in solving problems in a large variety of systems, with good quantitative agreements with experiment, particularly in BECs of the alkali atoms.

2.1.3 Thomas-Fermi Limit

For large condensates, the kinetic energy can usually be neglected compared to the interaction energy, leading to a density profile that takes a form of an inverted parabola. This is the so-called Thomas-Fermi limit. In a harmonic trap, the Thomas-Fermi density profile is given by

$$|\phi(\mathbf{r})|^2 = \frac{15}{8\pi} N \left(\frac{m\bar{\omega}_g}{2\mu} \right)^{3/2} \max \left[1 - \left(\frac{x^2}{R_{\text{TF},x}^2} + \frac{y^2}{R_{\text{TF},y}^2} + \frac{z^2}{R_{\text{TF},z}^2} \right), 0 \right], \quad (2.15)$$

where $R_{\text{TF},i} = \sqrt{2\mu/(m\omega_i^2)}$ is the Thomas-Fermi radius along direction $i \in \{x, y, z\}$ ^[41], and ω_i is the corresponding trap frequency. The chemical potential found in this regime is

$$\mu = \frac{\hbar\bar{\omega}_g}{2} \left(15 \frac{(N-1)a_s}{a_{\text{ho}}} \right)^{2/5}. \quad (2.16)$$

In our experiment the BEC is not exactly under the Thomas-Fermi regime, however, it helps to provide an intuitive picture when mainly considering the interactions.

2.2 Two-component BEC

In our experiment, a BEC of 1000 ± 40 ⁸⁷Rb atoms is prepared and trapped in a cigar-shaped magnetic potential. For the interferometric experiments presented in this thesis, we use two hyperfine states $|1\rangle \equiv |F = 1, m_F = -1\rangle$ and $|2\rangle \equiv |F = 2, m_F = 1\rangle$ as two modes, and we always prepare the atoms in a superposition of two states as a starting

point. These two hyperfine states are of special interest for several reasons. A key feature is that they are both magnetically trappable and have nearly identical magnetic moment. Therefore atoms experience nearly identical magnetic trapping potentials. Moreover, their first order differential Zeeman shift vanishes at a magnetic field of ≈ 3.23 G, making superpositions of the two states largely insensitive to magnetic field fluctuations^[38]. In our experiment, the two states can be coupled via a two-photon Rabi processes with a microwave and radio frequency field. A more detailed discussion of these two states can be found in section 3.3.

This system is used in recent experiments on many-particle entanglement and quantum metrology^[7] as well as compact atomic clocks^[6,26]. In this system, the particles are allowed to occupy two internal states. This introduced hyperfine (spin) degree of freedom immediately leads to complications of the physical pictures presented in the last section. The s -wave interaction strength for inter-species and intra-species collisions a_{11} , a_{22} and a_{12} are different from each other, leading to different interactions for the atoms in the two states. The condensate wave functions is dramatically affected by the presence of interspecies interactions.

For convenience, we define the order parameters for each internal state $\Psi_i(\mathbf{r}) = \sqrt{N_i}\phi_i(\mathbf{r})$, with the internal state (spin) index $i \in \{1, 2\}$ representing states $|1\rangle$ or $|2\rangle$. Then Eqs. (2.11) and (2.13) are extended to a set of two coupled equations. The time-dependent two-component GP equations (2CGPE) in terms of the order parameters read^[28,42]

$$i\hbar \frac{\partial \Psi_1(t)}{\partial t} = -\frac{\hbar^2}{2m} \nabla^2 \Psi_1(t) + V_1 \Psi_1(t) + g_{11} |\Psi_1(t)|^2 \Psi_1(t) + g_{12} |\Psi_2(t)|^2 \Psi_1(t), \quad (2.17)$$

$$i\hbar \frac{\partial \Psi_2(t)}{\partial t} = -\frac{\hbar^2}{2m} \nabla^2 \Psi_2(t) + V_2 \Psi_2(t) + g_{22} |\Psi_2(t)|^2 \Psi_2(t) + g_{12} |\Psi_1(t)|^2 \Psi_2(t), \quad (2.18)$$

where $g_{ij} = 4\pi\hbar^2 a_{ij}/m$ characterizes the s -wave scattering interactions between components i and j ($i, j \in \{1, 2\}$). For the two hyperfine states used in our experiments^[44],

$$a_{11} = 100.40a_0, \quad a_{22} = 95.44a_0, \quad a_{12} = 98.01a_0.$$

The three involved scattering lengths are nearly identical and differ from each other by no more than 5%. This causes a lot of interesting properties of our two-component BEC's behavior.

Typically, in our experiment, the magnetic trapping potential has approximately identical and tighter trapping frequencies along two directions (radial directions) and a shallower confinement along the third direction (axial direction). The condensate is thus with

an elongated shape. For convenience of numerical simulation, we take a cylindrical coordinate system (r, z, θ) when calculating the GPEs. The GPE simulation codes involved in this thesis are based on a cylindrical GPE package, which was developed in our group based on Wolfram MATHEMATICA by Roman Schmied.

2.2.1 Ground states

As a simplest example of the application of GPE in our system, the ground-state density profile for the two components can be found by solving the time independent version of 2CGPE Eq. (2.17) and (2.18). The density profile is calculated as $\int 2\pi|\Psi_i(r, z)|^2 r dr$ along axial (z)-direction and $\int 2\pi|\Psi_i(r, z)|^2 r dz$ along radial (r)-direction, both with a unit of atom/ μm . In Figure 2.1, the ground state densities of the two components are plotted, assuming 500 atoms populated in each state. The two wave functions differ from each other due to the fact that the self-interaction related scattering lengths are not exactly identical, $a_{11} \neq a_{22}$.

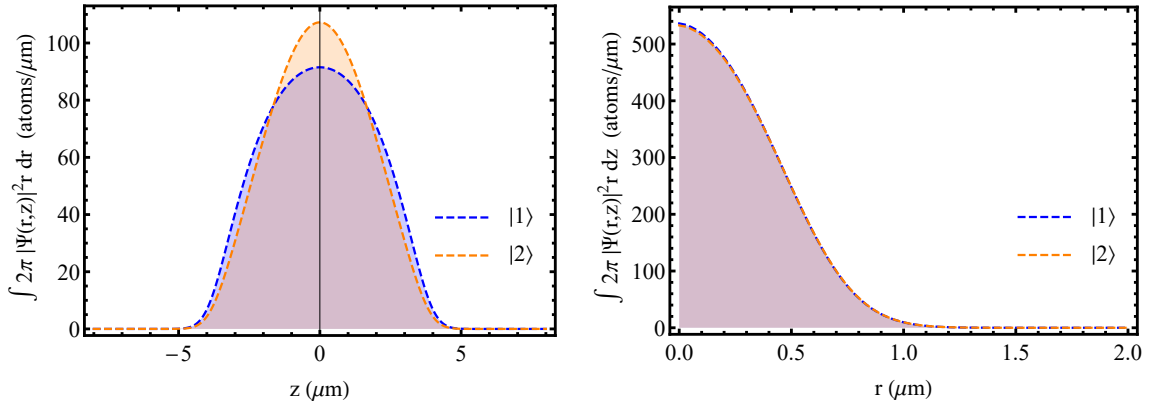


Figure 2.1 **Comparison between density profiles of both components.** Wave functions are simulated assuming the system in the ground state, with 500 atoms in each state, and for a trap with trapping frequency $\omega_r/2\pi = 714$ Hz and $\omega_z/2\pi = 114$ Hz. The density profiles are plotted as a cross section along the axial (z) and along the radial (r) direction, with normalization to total atom numbers.

2.2.2 Breathing dynamics

As mentioned before, in our interferometric measurements, a superposition of two spin states is always prepared as a starting point of the experiment. In the end of the evaporative cooling sequence, what we obtain is a BEC with all the atoms in the ground state $|1, -1\rangle$. Therefore a sudden $\pi/2$ Rabi pulse is always needed to transfer abruptly atoms of one internal state into a coherent superposition of two internal states. In other words, half the atoms will be driven to state $|2, 1\rangle$ while remaining the wave function as the ground

state wave function in state $|1, -1\rangle$. From this instant on, the system is not in the ground state any more, the equilibrium is broken immediately and the dynamics of the spatial mode of the two components is triggered. Since these two states have slightly different values of scattering lengths, the sudden change in self-interaction leads to periodic spatial dynamics of the condensate wave function, which is called “breathing dynamics”. The same demixing-remixing process of the two components is also observed in other experiments and this type of dynamical behavior makes possible a variety of two species BEC studies, for example to extract the values of scattering length^[45].

This dynamics can be very well described based on the time-dependent coupled GPEs Eqs. (2.17) and (2.18). To simulate the experiment, the initial state is calculated with half of the atoms in each internal state, and all with the ground state wave function of $|1\rangle$. The two internal states evolve according to the GPE. This leads to an oscillation of the wavefunctions, as shown in Figure 2.2. The two condensates are created with complete spatial overlap initially, and in subsequent evolution they undergo relative motions that tend to preserve the total density profile. As a consequence of the spatial dynamics, the overlap between the two components is modulated and reduced to a value smaller than 1, and will decrease the contrast of interferometric fringe.

2.3 Collective spin description

2.3.1 Pseudo-spin description

In our system, the degrees of freedom of atoms are restricted to only two hyperfine states, here denoted as $|1\rangle$ and $|2\rangle$. The external potentials (in our case the magnetic trap potential) for the two states are identical due to the same magnetic moment of the two states. Moreover, the self-interaction strength g_{11} and g_{22} are very similar due to the nearly identical intra-species scattering length. These reasons lead to very similar single particle wave functions for the two states, as already shown in section 2.2.1. The previously mentioned effect of breathing dynamics is weak in our system because of low atom density and can be ignored, as confirmed by the 2CGPE simulation and independent experiments^[29]. Therefore we assume the atoms condense in a single spatial mode, and the spatial shape of the wave functions does not alter the spin dynamics.

Under these assumptions, each atom can be described as a pseudo-spin-1/2 particle by identifying state $|1\rangle$ with spin up and state $|2\rangle$ with spin down^[7]. We will see that, with this pseudo-spin description in this section, a quantum state can be visualized geo-

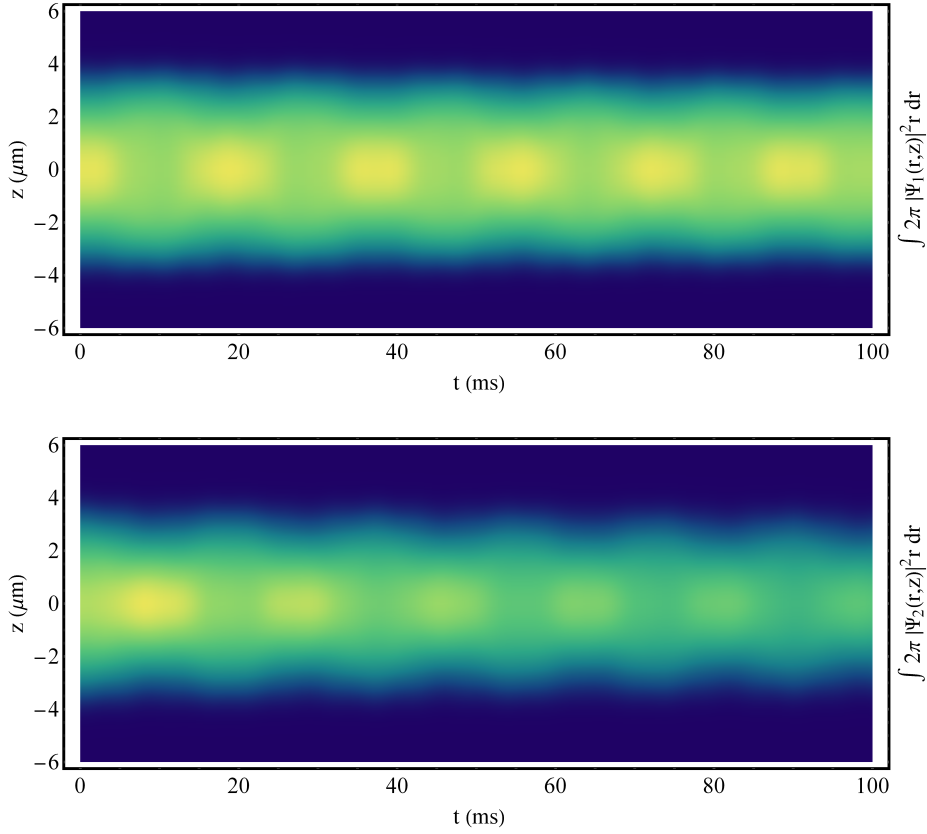


Figure 2.2 **The breathing dynamics simulated by 2CGPE.** The color represents the atomic density along the z direction, shown as a function of time after the $\pi/2$ Rabi pulse. The atom losses are taken into consideration in this simulation.

metrically on a so called Bloch-sphere, and the quantum behavior of an N -atom ensemble can then be regarded as collective. For convenience, all spins will be expressed in units of \hbar in this section, such that we can write $\hbar = 1$ in the pseudo-spin space.

2.3.1.1 Single spin

For a single particle, we define the spin operators of the particle as \hat{s} , satisfying $\hat{s} = \frac{1}{2}\hat{\sigma}$, where $\hat{\sigma} = \{\hat{\sigma}_x; \hat{\sigma}_y; \hat{\sigma}_z\}$ is the Pauli vector. In this way, we map the two-level atom onto a spin-1/2 system. The spin components \hat{s}_x and \hat{s}_y describe the coupling between the two states and \hat{s}_z describes difference between the probabilities that the atom is in the two states.

A pure state can be written as a superposition of the two states $|1\rangle$ and $|2\rangle$ with only two parameters,

$$|\theta, \phi\rangle = \cos(\theta/2)|1\rangle + e^{i\phi} \sin(\theta/2)|2\rangle. \quad (2.19)$$

In this way, a pure state of a single spin can then be represented geometrically as a point

on the surface of a Bloch sphere, as shown in Figure 2.3, with coordinates $0 \leq \theta \leq \pi$ and $0 \leq \phi < 2\pi$ representing the polar and azimuthal angle, respectively. The parameter θ determines the relative population between the two levels and ϕ describes the relative phase. The Cartesian coordinates of the point $\mathbf{s} = \frac{1}{2}\{\sin \theta \cos \phi; \sin \theta \sin \phi; \cos \theta\}$ is the spin direction with a spin length of $|\hat{\mathbf{s}}| = \frac{1}{2}$.

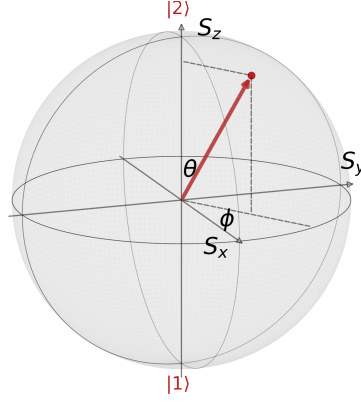


Figure 2.3 **Bloch sphere.** The state of a two-level system can be described by a single spin-1/2 (red arrow) and can be shown as a point on the surface of a Bloch sphere.

A mixed state of a single spin $\frac{1}{2}$ can be written by a density matrix,

$$\hat{\rho} = \sum_i p_i |\psi_i\rangle\langle\psi_i| = (1 + \hat{\mathbf{s}} \times \hat{\boldsymbol{\sigma}})/2 \quad (2.20)$$

where $0 \leq p_i \leq 1$ is the statistical weight of the i th pure state $|\psi_i\rangle$, and $\sum_i p_i = 1$. One can tell if a system is in a pure state or a mixed state by the trace of $\hat{\rho}^2$. For a mixed state $\text{Tr}(\hat{\rho}^2) = \frac{1}{2} + 2|\langle\mathbf{s}\rangle|^2 < 1$, where $\langle\mathbf{s}\rangle = (\langle\hat{s}_x\rangle, \langle\hat{s}_y\rangle, \langle\hat{s}_z\rangle)$ is the expectation of the spin vector, while for a pure state $\text{Tr}(\hat{\rho}^2) = 1$. Therefore, if the system in a pure state, the spin length $|\langle\hat{\mathbf{s}}\rangle| = \frac{1}{2}$; if system in a mixed state, the spin length $|\langle\hat{\mathbf{s}}\rangle| < \frac{1}{2}$. Therefore all the pure states are on the surface of Bloch sphere, while the mixed states are inside the Bloch sphere, with an additional degree of freedom given by the length of the spin vector $0 \leq r \leq 1$.

2.3.1.2 Multiple spins

For an ensemble of N particles, we can introduce a similar concept of pseudo-spin space. We define the collective spin vector $\hat{\mathbf{S}} = \{\hat{\mathbf{S}}_x, \hat{\mathbf{S}}_y, \hat{\mathbf{S}}_z\}$, which is defined as a sum of the individual spins,

$$\hat{\mathbf{S}}_{(x,y,z)} = \frac{1}{2} \sum_{l=1}^N \hat{\boldsymbol{\sigma}}_{(x,y,z)}^{(l)} = \sum_{l=1}^N \hat{\mathbf{s}}_{(x,y,z)}^{(l)}, \quad (2.21)$$

where $\hat{\sigma}^{(l)}$ ($\hat{s}^{(l)}$) is the Pauli vector (spin operator) of the l th particle. The collective spin operators have a linear degenerate spectrum spanning the 2^N dimensional Hilbert space. In this thesis, we restrict our discussion to indistinguishable bosons satisfying the particle exchange symmetry, allowing a formidable simplification of the Hilbert space from 2^N to $N+1$ dimensions. Following the Schwinger's oscillator model of angular momentum^[46], we introduce the bosonic creation \hat{a}^\dagger (\hat{b}^\dagger) and annihilation \hat{a} (\hat{b}) operator for the modes $|1\rangle$ ($|2\rangle$). The number operator is then defined as

$$\hat{N}_1 \equiv \hat{a}^\dagger \hat{a}, \quad \hat{N}_2 \equiv \hat{b}^\dagger \hat{b}. \quad (2.22)$$

We denote the total atom number operator as $\hat{N} = \hat{a}^\dagger \hat{a} + \hat{b}^\dagger \hat{b}$. In this case,

$$\hat{S}_x = \frac{\hat{a}^\dagger \hat{b} + \hat{b}^\dagger \hat{a}}{2}, \quad \hat{S}_y = \frac{\hat{a}^\dagger \hat{b} - \hat{b}^\dagger \hat{a}}{2i}, \quad \hat{S}_z = \frac{\hat{a}^\dagger \hat{a} - \hat{b}^\dagger \hat{b}}{2}. \quad (2.23)$$

We see that \hat{S}_z is half the difference in the populations of the two modes, which can be measured experimentally, therefore is the most important observable in an interferometric measurement. The operators satisfy the angular momentum commutation relations:

$$[\hat{S}_x, \hat{S}_y] = i\hat{S}_z, \quad [\hat{S}_z, \hat{S}_x] = i\hat{S}_y, \quad [\hat{S}_y, \hat{S}_z] = i\hat{S}_x, \quad (2.24)$$

Therefore, an arbitrary pair of orthogonal spin operators obeys the Heisenberg uncertainty relation, for example,

$$(\Delta \hat{S}_y)^2 (\Delta \hat{S}_z)^2 \geq \frac{1}{4} \langle \hat{S}_x \rangle^2. \quad (2.25)$$

Similar to a single spin, the state of the multiple spins introduced in Eq. (2.21) assumes a convenient graphical representation on the surface of a generalized Bloch sphere with radius $N/2$. The components of the collective spin operator have expectation values

$$\langle \hat{S}_x \rangle = \frac{N}{2} \cos(\phi) \sin(\theta) \quad (2.26a)$$

$$\langle \hat{S}_y \rangle = \frac{N}{2} \sin(\phi) \sin(\theta) \quad (2.26b)$$

$$\langle \hat{S}_z \rangle = \frac{N}{2} \cos(\theta). \quad (2.26c)$$

Any unitary transformation of a single spin $\frac{1}{2}$ can be considered as a rotation $e^{-i(\theta/2)\hat{\sigma}_n}$ on the Bloch sphere, where \mathbf{n} and θ are the rotation axis and rotation angle, respectively. With multiple spins, each locally rotated about the same axis \mathbf{n} and angle θ , the transformation is $\bigotimes_{l=1}^N e^{-i(\theta/2)\hat{\sigma}_n} = e^{-i\theta\hat{S}_n}$. Most of the interferometric transformations discussed in this thesis can be modelled by this collective rotation. Take the Ramsey interferometer as an example, the three rotations (first $\pi/2$ Rabi pulse, then the phase accumulation, and finally another $\pi/2$ Rabi pulse) involved correspond to an unitary transforma-

tion $e^{i(\pi/2)\hat{S}_x}e^{-i(\theta)\hat{S}_z}e^{-i(\pi/2)\hat{S}_x} = e^{-i(\theta)\hat{S}_y}$, therefore the whole interferometer sequence is equivalent to a collective rotation around the y axis on the generalized Bloch sphere^[47].

2.3.2 Coherent spin dynamics

In section 2.2, a mean-field description of the two-mode BEC has been given by two-component GPE. However, there are interactions between atoms induced by elastic collisions, which result in correlations that are beyond the mean-field description and cannot be captured by the GPE. In order to describe the collisional interactions in the two-component BEC, we use the collective spin description introduced before, and the Hamiltonian of the system can be written as^[28,48-50]

$$\hat{H} = \nu\hat{S}_z + \hbar\chi\hat{S}_z^2 + \text{const} . \quad (2.27)$$

The collective Hamiltonian contains a constant term, a nonlinear term with rate χ and a linear term with rate $\nu = \hbar((\mu_1 - \mu_2) - 2\chi\langle\hat{S}_z\rangle + \tilde{\chi}(\hat{N} - \langle N \rangle))$, where μ_i ($i = 1, 2$) are the chemical potentials of the atom in mode $|i\rangle$, given by

$$\mu_i = \frac{\partial H}{\partial N_i} = \langle\phi_i|(-\frac{\hbar^2}{2m}\nabla^2 + V)|\phi_i\rangle + \sum_{j=1,2} g_{ij}N_j \int |\phi_i|^2|\phi_j|^2 d\mathbf{r}^3, \quad (2.28)$$

where ϕ_i is the mode function normalized to 1, and \hat{N} is the total particle number operator. The first part on the right hand side describes the kinetic and potential energy of the component, and the second part describes the interaction energies including the self-interaction and the interaction with the other spin mode. The coefficients χ and $\tilde{\chi}$ are given by^[49]

$$\tilde{\chi} = \frac{1}{2\hbar} \left(\frac{\partial\mu_1}{\partial N_1} - \frac{\partial\mu_2}{\partial N_2} \right), \quad (2.29)$$

$$\chi = \frac{1}{2\hbar} \left(\frac{\partial\mu_1}{\partial N_1} + \frac{\partial\mu_2}{\partial N_2} - \frac{\partial\mu_1}{\partial N_2} - \frac{\partial\mu_2}{\partial N_1} \right). \quad (2.30)$$

The derivatives in Eqs (2.29) and (2.30) are to be evaluated at the mean values of atom numbers $\langle N_1 \rangle$ and $\langle N_2 \rangle$. Furthermore, if the mode functions are independent of N , the above equations simplify to

$$\tilde{\chi} = \frac{1}{2\hbar}(u_{11} - u_{22}), \quad (2.31)$$

$$\chi = \frac{1}{2\hbar}(u_{11} + u_{22} - 2u_{12}), \quad (2.32)$$

where $u_{ij} = g_{ij} \int |\phi_i|^2 |\phi_j|^2 d\mathbf{r}$, is the density overlap between mode i and j .

In this thesis, both the linear and the nonlinear terms in the Hamiltonian Eq. (2.27)

will be discussed in detail. The linear term contains an N -dependent phase rotation with rate $\tilde{\chi}\hat{N}$, and constitutes a dominant factor of decoherence in the system in the presence of random atom losses, see chapter 4. The nonlinear interaction $\chi\hat{S}_z^2$ is known as the *one-axis twisting* Hamiltonian, which is crucial for preparing a spin-squeezed state, see chapter 5. As one can see from the definitions of the coefficients, both $\tilde{\chi}$ and χ depend on the second derivatives of the total energy $\frac{\partial^2 H}{\partial N_i \partial N_j}$. The linear term $\tilde{\chi}\hat{N}\hat{S}_z$ arises naturally from difference of the interaction energies between the two spin states, therefore depends on total atom number and the intraspecies scattering lengths a_{11} and a_{22} through the interaction strengths g_{11} and g_{22} . The nonlinear term $\chi\hat{S}_z^2$ accounts for the interaction of each atom with all the other atoms, with the strength χ of this nonlinear interaction depends on all the scattering lengths a_{ij} and on the wave-function overlaps $\int |\phi_i|^2 |\phi_j|^2 d\vec{r}^3$. For our interferometer states $|1\rangle$ and $|2\rangle$, the scattering lengths are similar: $a_{11} = 100.40a_0$, $a_{12} = 98.01a_0$ and $a_{22} = 95.44a_0$ ^[44], leading to a small χ for overlapping clouds. In our experiment, χ can be modified by changing the wave-function overlap, as done in this work.

2.3.3 Quasi-probability distribution

The wave function that appears in Schrödinger's equation for the two-mode system is usually written in the form of a linear combination of the Dicke states (discussed later in section 2.3.4.1), with the coefficients describing the probability distribution in the Dicke basis. However, an intuitive and graphical description of the collective spin given in the phase space is more convenient and is needed when studying the dynamics of a spin system. In order to link the wave function to a probability distribution in phase space, two quasi-probability-distribution functions for harmonic modes are introduced, known as Wigner function^[51] and Husimi Q-function^[52].

Wigner function is a complete description of the quantum state, equivalent to the density matrix. Conventionally Wigner function is defined on the planar phase space, whereas in order to visualize a quantum state of a two-mode system on the Bloch sphere (as in our case), a spherical Wigner function was derived^[53]

$$W(\vartheta, \phi) = \sum_{k=0}^{2S} \sum_{q=-k}^k \rho_{kq} Y_{kq}(\vartheta, \phi), \quad (2.33)$$

where ϑ and ϕ are the polar and azimuthal angles on the Bloch sphere, respectively, and the weights ρ_{kq} are related to the density matrix elements $\rho_{mm'} = \langle S, m | \hat{\rho} | S, m' \rangle$ in the

$|S, m\rangle$ -basis, where $\hat{\rho}$ is the density matrix, by the transformation coefficients t_{kq}

$$\rho_{kq} = \sum_{m=-S}^S \sum_{m'=-S}^S t_{kq}^{Smm'} \rho_{mm'}. \quad (2.34)$$

Unlike the real probability distributions, Wigner function can be negative, and the negativity of Wigner function is a definite indicator that a state is distinctly non-classical. In Figure 2.4, the spherical Wigner functions of four different quantum states are plotted. The spherical Wigner function $W(\vartheta, \phi)$ is similar to the traditional Wigner function defined on the planar phase space of a harmonic oscillator. It can be seen as a quasi-probability distribution, and the ‘‘center of mass’’ of W corresponds to the expectation value of \mathbf{S} .

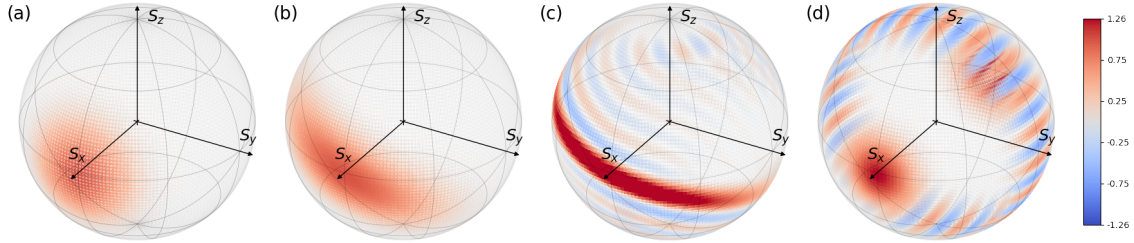


Figure 2.4 Bloch sphere representations of different quantum states. (a) Wigner function of a coherent spin state $|CSS : \pi/2, 0\rangle$, calculated for $N = 20$ atoms. The projection on the z -axis describes the population difference $(N_2 - N_1)/2$ and the angle ϕ in the xy -plane corresponds to the phase of the system. The mean spin direction is along x -direction and the spin uncertainty in the direction perpendicular to mean spin is isotropic, $(\Delta\hat{S}_y)^2 = (\Delta\hat{S}_z)^2 = \frac{N}{4}$. (b) Wigner function of a spin-squeezed state, prepared with one-axis twisting at $\chi t = 0.03$. (c) Wigner function of a spin-squeezed state, prepared with $\chi t = 0.1$. (d) Wigner function of a Schrödinger cat state.

Another well known quasiprobability in phase space is the Husimi Q distribution, first introduced by Kôdi Husimi in 1940^[52]. It can be constructed by

$$Q(\rho) = \frac{1}{\pi} \langle S, m | \hat{\rho} | S, m' \rangle$$

where $|S, m\rangle$ is the Dicke state basis. It is the simplest quasiprobability distribution to calculate compared to others.

2.3.4 Examples of collective spin states

There are various relevant quantum states of a collective spin ensemble. Some collective spin states are of particular importance when it comes to the interferometric measurements. In this section we discuss Dicke states, coherent spin states, spin-squeezed states and Schrödinger cat states, which are the states of significance and that will be encountered in the later chapters.

2.3.4.1 Dicke state

A simultaneous eigenstate of \hat{S}^2 and \hat{S}_z is called a Dicke state, or an angular momentum eigenstate. It is defined by

$$\begin{aligned}\hat{S}^2|S, m\rangle &= s(s+1)|S, m\rangle, \\ \hat{S}_z|S, m\rangle &= m|S, m\rangle,\end{aligned}$$

where the Dicke states are denoted with the symbol $|S, m\rangle$. Under the particle exchange symmetry, S takes the largest value $S = N/2$ and Dicke states are thus $|N/2, m\rangle$, with $m = -N/2, -N/2 + 1, \dots, N/2 - 1, N/2$. These states form a complete basis for the $N + 1$ dimensional subspace. It is easy to prove that

$$\langle S_x \rangle = \langle S_y \rangle = 0, \quad \langle S_z \rangle = m.$$

Therefore its mean spin is along the z direction. A Dicke state $|N/2, m\rangle$ can be characterized by m , the specific relative atom number between the two spins $m = \langle \hat{S}_z \rangle$, *i.e.*, there are $N/2 + m$ atoms in state $|1\rangle$ and $N/2 - m$ atoms in state $|2\rangle$.

A special type of Dicke states is with $m = 0$, meaning that there are half of the atoms in each internal state, and such Dicke states are known as a twin-Fock state^[54]. Twin-Fock states are of significant importance in the field of quantum metrology, and have been demonstrated in experiments using techniques such as non-destructive measurement or controlling collision dynamics^[55-57].

2.3.4.2 Coherent spin state

Coherent spin states can be written as a tensor product of N identical and independent spin-1/2 states:

$$|\theta_0, \phi_0\rangle = \otimes_{k=1}^N (\cos(\theta_0/2)|1\rangle + e^{i\phi_0} \sin(\theta_0/2)|2\rangle).$$

It is easy to prove that the mean spin is

$$\langle S \rangle = N \langle s \rangle = S(\sin \theta_0 \cos \phi_0, \sin \theta_0 \sin \phi_0, \cos \theta_0),$$

which means all the individual spins point on average along a specific direction (θ_0, ϕ_0) . It is clear that the coherent spin state is a direct product state, that is, there is no entanglement between atoms. For an arbitrary state, the fluctuation of any collective spin component perpendicular to the mean spin can be calculated:

$$(\Delta S_\perp)^2 = \langle S_\perp^2 \rangle - \langle S_\perp \rangle^2 = \sum_l (\Delta s_\perp^l)^2 + \sum_{k \neq l} [\langle s_\perp^l s_\perp^k \rangle - \langle s_\perp^l \rangle \langle s_\perp^k \rangle] \quad (2.35)$$

where the first term is the sum of all the individual spin fluctuations, and the second term actually considers the correlation. For the coherent spin state, the atoms are independent of each other, the second term thus yields 0 and the fluctuation of any collective spin component perpendicular to the mean spin is simply the sum of the individual spin fluctuations. In other words, along any quadrature perpendicular to the mean spin direction, the noise is always isotropic and equal to $N/4$. This is the so-called *projection noise*.

The coherent spin state can also be understood from a statistical point of view. A coherent spin state can be expressed as the binomial distribution, under the basis of Dicke states:

$$|\text{CSS}; \theta, \phi\rangle = \sum_{m=-S}^S \left[\binom{N}{x} p^x (1-p)^{N-x} \right]^{\frac{1}{2}} e^{-im\phi} |S, m\rangle, \quad (2.36)$$

with $N = 2S$, $x = S + m$ and $p = (\cos \frac{\theta}{2})^2$. Figure 2.4(a) shows the spherical Wigner function of a coherent spin state, with $N = 20$ and $\theta = \pi/2$.

2.3.4.3 Spin-squeezed state

As mentioned above, the fluctuation distribution of a coherent spin states is isotropic along different quadratures. One can “squeeze” such a state so that the spin fluctuation in a particular direction perpendicular to the mean spin is decreased, at the price of increasing the fluctuation in another direction. This is the spin-squeezed state (SSS). It was first proposed by M. Kitagawa and M. Ueda^[20] and has been extensively studied in different systems due to its significant importance in the applications of precision measurement^[7]. The SSS still obey the Heisenberg uncertainty relationship with such an anisotropy fluctuation profile, while the metrological advantage of spin-squeezed state is evident since it allows a quantity of interest such as relative phase accumulated between two modes to be resolved with a precision beyond the classical limit, *i.e.*, the standard quantum limit (SQL). Compared to other highly non-classical states, spin-squeezed states are relatively robust against particle losses, making them especially suited for practical applications. Experimentally, such states can be prepared using different schemes. For our experiment, by evolving a coherent spin state on the equator, $|\text{CSS}; \pi/2, \phi\rangle$, with the one-axis twisting Hamiltonian $\chi \hat{S}_z^2$ for a time^[20], we can achieve a spin-squeezed state. As the spin-squeezing is one of the main focuses of this thesis, the concept of SQL and the mechanisms applied to prepare SSS will be discussed in details later.

2.3.4.4 Schrödinger cat state

Schrödinger cat states, which are the coherent superposition of two (or more) coherent states. They highlight a counterintuitive feature of quantum mechanics which is the possibility of a superposition of macroscopically distinct states. One typical cat state, known as a Greenberger–Horne–Zeilinger state (GHZ state), refers to the possibility that multiple atoms are in a superposition of all spin up and all spin down and can be written as $\frac{1}{\sqrt{2}}(|S, -S\rangle + |S, +S\rangle)$. Schrödinger cat states are optimal for quantum metrology since they allow to reach the Heisenberg limit for phase estimation, *i.e.*, $\sigma\phi = 1/N$ which is the best allowed by quantum mechanics. Experimentally, such states can be prepared by evolving a coherent spin state on the equator, $|\text{CSS}: \pi/2, \phi\rangle$, with the one-axis twisting Hamiltonian $\chi\hat{S}_z^2$ at $t = \pi/(2\chi)$. A characteristic feature of strong entanglement in an N -atom cat state is a band of N fringes in the Wigner function. Unfortunately, cat states are extremely fragile, as it can be easily destroyed by noise and a single loss of particle.

2.4 Phase coherence in a Bose-Einstein Condensate

Phase coherence, as the essential factor underlying BEC, is studied both experimentally and theoretically from two aspects: the spatial coherence and the temporal coherence.

2.4.1 Spatial coherence

The first interference between two independent BECs was reported in a double-well potential, where atoms are released to spread and overlap^[58]. This experiment, to some extent equivalent to a Young's double-slit experiment, for the first time showed that the two independent BECs interfere. Then the atom interferometry has been demonstrated with BECs in double-well potentials^[40,59-60] and classical Josephson arrays of tunnelling coupled condensates^[61-62]. Ever since then, the phase coherence over a long range across BEC (phase coherence in spatial domain) has become a particular interest because it fundamentally determines the formation of the interference pattern between two BECs. Moreover, the phase property of BEC is also related to some quantum phenomena such as superconductivity and superfluidity, and can be exploited in different applications such as quantum information.

There have been many efforts to explore the spatial coherence across a condensate for a variety of systems. The first experimental measurement of the spatial coherence of a BEC was demonstrated in 1999^[63] by creating and interfering two spatially displaced

fractions of the original BEC. Followed was a series of experimental investigations of the coherence of BEC focused on the spatial domain: the uniformity of the spatial phase has been demonstrated which implies the coherence length of the condensate is equal to its size^[63-64], the spatial correlation function has been determined^[65], and the decoherence was studied in different systems: from three-dimensional BEC^[66] to condensates in two-dimensional optical lattice^[67], and the one-dimensional Boson gases^[68-69].

To briefly summarize, for a trapped pure three-dimensional BEC, one expects the phase to be spatially uniform because the condensate is in a stationary state of the system with no angular momentum. However, due to some technical noise (for example the spatial gradients of the external fields) and the mean field interactions, one might expect differences in the phase between different regions of the condensate. In these reports, the mean-field atom-atom interactions play an important role and are responsible for the decoherence in the spatial domain. Besides, the occurrence of phase fluctuations due to thermal excitations is studied in elongated BEC^[66].

2.4.2 Temporal coherence

Given the well-developed techniques in preparing and manipulating atomic Bose-Einstein condensates, the interferometric schemes based upon ultracold atoms stimulate great interests. For any type of these precision measurements with BECs, a first fundamental problem is how long its coherent time is since it poses limit on the duration of the interferometric sequences. Considerable theoretical attention has been devoted to the matter of the relative phase between two independent condensates: how the relative phase is established by measurement^[70-71], and how it evolves in presence of atomic interactions^[72-73] and in presence of particle losses^[74]. The phase property of a uniform single-component BEC has also been extensively studied. Theoretical studies make different predictions for the phase spreading over time^[75-76]. Depending on how the system is initially prepared, the phase spreading can be ballistic (*i.e.*, phase variance grows with $\sim t^2$) or diffusive (*i.e.*, phase variance grows with $\sim t$). Phase diffusion at finite temperature^[77] and fluctuations in the atom number^[9] are also expected to limit the coherence time of a BEC. Theoretical studies of BEC temporal coherence have predicted different decoherence mechanisms resulting from both homogeneous and inhomogeneous effects^[76,78].

2.4.2.1 Inhomogeneous effects

In trapped ensembles, atoms explore inhomogeneous shift of the energy difference between two spin modes, due to the magnetic trapping potentials, the atomic interactions, and other technical noises such as the inhomogeneity of the external magnetic field. Atoms therefore evolve at different rates on the generalized Bloch sphere, leading to the decoherence of the BEC. Previous experiments have mostly investigated inhomogeneous effect in magnetically trapped BECs^[79-81]. For the two internal states we are interested in, temporal coherence caused by the inhomogeneous effects has been studied in similar systems including thermal^[6,25,80-82] and degenerate ensembles^[5,38,79,83]. A main decoherence mechanism in these experiments can be described by the spatial dynamics of the condensate wave functions within the mean-field theory. For example, experiments in Ref^[81] have shown that, in absence of atom losses, the phase of a BEC undergoes collapses and revivals in time caused by elastic interactions due to the atom-atom collisions. There are other earlier experiments investigating the “atomic laser” which is formed by continuously extracting atoms from a BEC. These atoms, with positive scattering lengths, will develop phase variations over time since it expands due to the atom-atom (mean-field) interaction^[84].

Various mechanisms have been exploited to reduce the inhomogeneous dephasing. A mutual compensation scheme^[85] has been demonstrated to extend the coherence time by adjusting the trap-induced inhomogeneity to compensate the mean-field inhomogeneity. The spin echo techniques have been successfully employed in experiments to reverse the mean-field inhomogeneous dephasing and spatial demixing^[81,86]. The spin self-rephasing mechanism induced by the identical spin rotation effect has been used to extend the coherence time^[86-87].

2.4.2.2 Homogeneous effects

Theory predicts decoherence also from homogeneous effects^[76], which arises from elastic and inelastic collisions. The elastic collisions cause energy shifts, and experiments necessarily involve inelastic collisions that cause phase jumps. Both effects are density-dependent, therefore are more severe in chip trap than in systems such as atomic vapor cells and atomic fountains. Theoretical models were built to describe the phase dynamics of BEC in presence of collisional losses^[76,78].

Despite the long-standing theoretical interest on the homogeneous effects, it was not

easy to observe them because the technical noise usually dominates in previous experiments. As an intrinsic effect arises from within the many-body system itself, the homogeneous effects can only be revealed with the almost perfect isolation of the system from the environment, in combination with a very high preparation and detection fidelity. Therefore a detailed experimental study of the predicted homogeneous phase decoherence mechanism^[76,78], which fundamentally limits the BEC coherence, has not yet been reported. In chapter 4, we will for the first time study the homogeneous decoherence caused by the interplay between elastic atom-atom interaction and the stochastic collisional losses in detail.

2.5 Quantum metrology

This section illustrates how the standard quantum limit arises in interferometry and how it can be overcome using resources such as spin-squeezing or entanglement.

2.5.1 Standard quantum limit

Consider a Ramsey interferometer performed with N uncorrelated (or classically correlated) atoms, with two modes labeled as $|1\rangle$ and $|2\rangle$. The atoms are initially in state $|1\rangle$ and prepared in an equal superposition $(|1\rangle + |2\rangle)/\sqrt{2}$ by a resonant Rabi $\pi/2$ pulse corresponding to the first beam splitter of the interferometer. During the subsequent interrogation time, $|1\rangle$ and $|2\rangle$ acquire a relative phase θ , such that the state evolves to $(e^{-i\theta/2}|1\rangle + e^{i\theta/2}|2\rangle)/\sqrt{2}$. The phase θ encodes the quantity to be measured. Finally, a second $\pi/2$ pulse (the second beam splitter) is applied so that the information of the phase θ is projected onto the z -component of the spin. The output state of the Ramsey interferometer is then $|\psi\rangle = \cos(\theta/2)|1\rangle + \sin(\theta/2)|2\rangle$ and the phase θ is usually estimated, for instance, by measuring the normalized population difference $\hat{n} = \frac{\hat{a}^\dagger \hat{a} - \hat{b}^\dagger \hat{b}}{N}$ in our case.

The standard quantum limit can be understood from the binomial statistics of the N uncorrelated particles. Consider there are N uncorrelated atoms and we measure the spin of them one by one. Each measurement has only one outcome with the probability of being either spin up $p = \cos(\theta/2)^2$ or spin down $1 - p$. Each measurement is independent of each other, thus measured number of spin up satisfying a binomial statistics $N_1 \sim B(N, p)$. The expect value of the outcome is $\langle N_1 \rangle = N \cos(\theta/2)^2$, with variance $\sigma_{N_1}^2 = N p(1 - p) = \frac{N(\sin \theta)^2}{4}$. Therefore the interferometer signal is the expectation value $\langle \hat{n} \rangle = \cos \theta$, with a maximum slope of 1 at $\theta = \pi/2$. The noise at the output will be determined by the variance

$\sigma_n^2 = \frac{4}{N^2} \sigma_{N_1}^2 = \frac{(\sin \theta)^2}{N}$, correspondingly the phase uncertainty of the measurement in terms of standard deviation can be calculated with the error propagation:

$$\sigma_\theta = \frac{\sigma_{\hat{n}}}{d\langle \hat{n} \rangle / d\theta} \geq \frac{1}{\sqrt{N}}. \quad (2.37)$$

This is precisely the standard quantum limit $\sigma_{\theta, \text{SQL}}$.

In some other cases, the observable can also be atom number imbalance $\hat{M} = \hat{N}_1 - \hat{N}_2 = \hat{a}^\dagger \hat{a} - \hat{b}^\dagger \hat{b}$ between the two states, but the precision limit of measurement is the same.

2.5.2 Entanglement enhanced interferometer

The SQL, as a classical limit, can be overcome with resources of non-classical correlations between the constituent particles of a many-body system. Non-classical correlations^[27,88] are identified with different families, namely entanglement (or non-separability), Einstein-Podolsky-Rosen (EPR) correlations, and Bell (or nonlocal) correlations. These states provide resources allowing a system to perform better than with classical correlations, not only in quantum metrology^[16-19,22-23], but also in tasks such as quantum teleportation^[89].

Particularly, the spin-squeezed state^[20] mentioned before is a typical type of entangled state. Compared to a classical state, it is squeezed so that the variance in some spin quadrature is reduced, enabling to achieve better precision in interferometric measurement of $\sigma_\theta < 1/\sqrt{N}$. Therefore spin squeezed state of ultra-cold atomic ensembles find applications in quantum-enhanced metrology.

In order to achieve phase uncertainty beyond SQL, not only the spin variance must be reduced, the interferometric slope (or contrast) $C = d\langle \hat{n} \rangle / d\theta$ also should remain high. The maximum value the contrast could reach is actually determined by the *length of the mean spin* $C_{\text{max}} = \frac{|\langle \vec{S} \rangle|}{N/2}$, where $|\langle \vec{S} \rangle| = \sqrt{\langle \hat{S}_x \rangle^2 + \langle \hat{S}_y \rangle^2 + \langle \hat{S}_z \rangle^2}$. Usually, we choose the frame of the Bloch sphere so that x is the direction of the mean spin, then $C = \frac{\langle \hat{S}_x \rangle}{N/2}$. The contrast can be, for example, affected by the anti-squeezing. One can intuitively understand it by imagining an elongated state wrapping around the pole on the Bloch sphere, see Fig 2.4 (b)(c), the length of the mean spin is largely reduced due to spin noise along the anti-squeezed quadrature, $|\langle \vec{S} \rangle| < N/2$, leading to a much smaller contrast. The overall phase uncertainty is finally decided by the spin variance and the spin length together. In order to characterize *metrologically useful spin squeezing*, the parameter ξ is

defined by Wineland in Reference [11] as

$$\xi^2 = \frac{N \text{Var}(\hat{S}_\theta)}{\langle \hat{S}_x \rangle^2}, \quad (2.38)$$

where θ is a rotation angle around x (the direction of the mean spin length). This angle can be freely chosen and optimized in order to measure spin component along the squeezed direction. Again using linear error propagation, the phase uncertainty of a spin-squeezed state is

$$\sigma_\varphi = \xi/\sqrt{N}. \quad (2.39)$$

Thus, the SQL corresponds to $\xi = 1$ and a state with $\xi < 1$ is useful for sub-SQL interferometry. Thus, the squeezing parameter ξ is a measure for *metrologically useful* squeezing.

2.5.3 Strategies of preparing non-classical correlations

In experiments with cold and ultracold atomic ensembles, a variety of spin-squeezed and other non-classical states have been prepared using different schemes. For a detailed overview of such states and techniques, we refer to Ref. [7]. The main techniques adopted to create non-classical states rely on either elastic collisional interactions between atoms^[17,29,90], or the quantum spin-mixing dynamics^[55,91-96], the light mediated coherent interaction between atoms^[23-24,97-99], and the quantum non-demolition measurements^[21-22,100]. These allow the preparation of spin squeezed/over-squeezed states, Dicke states, twin-Fock states and in principle Schrödinger cat states. Using the above mentioned techniques, demonstrations of entanglement-enhanced interferometry have been reported, and found applications to sense magnetic fields^[19,98,101].

One-axis twisting (OAT) can be used to prepare spin-squeezing in the ultracold systems, as used in this thesis and previous work in our group. The one-axis twisting Hamiltonian was first introduced in^[20] and written as $\hat{H}_{\text{OAT}} = \hbar\chi\hat{S}_z^2$. The spin dynamics of a quantum state under OAT is thus described by $e^{-i\chi\hat{S}_z^2 t}$, which introduces a rotation around z -axis with a \hat{S}_z -dependent rate and leads to a “twisting” of the quantum state. For ⁸⁷Rb states, the twisting strength χ for a system using internal states $|F = 1, m_F = -1\rangle$ and $|F = 2, m_F = +1\rangle$ of ⁸⁷Rb (as in our case) is typically very small because of the nearly identical scattering lengths. Different techniques have been developed to tackle this problem. One way is to tune χ by modifying the relative scattering length a_{ij} via *Feshbach resonance*^[17], but no such resonance is available for our state pair.

An alternative way, which is used in this thesis, is to modify χ by controlling the

wave-function overlap via a *spin-dependent trap potential*^[102]. In previously works of our group^[29,103], χ can be increased by three orders of magnitude by separating the wave functions of the two states. In our group, spin-squeezed states have been previously generated with $\xi^2 = -5.5$ dB in an ensemble of $N = 480$ ^{87}Rb atoms on an atom chip^[104-105], and an interferometer to detect magnetic field was operated 4.0 dB below the SQL^[19], using the same techniques as described in this thesis. In this work we have improved the spin squeezing to a level of $\xi^2 = -9.8(5)$ dB and the interferometer to -7 dB below SQL.

Non-demolition measurements (QND) are also used to demonstrate spin squeezing. QND measurement is a special type of measurement on quantum systems, in which the measured observables are conserved after the measurement. QND measurements have also been used to prepare spin-squeezed states, in a considerable amount of experiments, from optical dipole trap^[21-22], to the atom vapor cell^[100], and the cavity-based measurements^[23-24,97-99]. *The light mediated coherent interaction between atoms* is one of the important ways of realizing the QND^[97], where a typical model Hamiltonian is $\hat{H} = \hat{S}_z \hat{J}_z$, with \hat{S}_z the light Stokes operator and \hat{J}_z the atomic spin operator.

Some other experiments explored the creation of the *Twin-Fock state* in spin-1 system with $|m_F = \pm 1\rangle$ internal states. So-called twin-Fock states, which contain an equal number of particles in each of two modes, can be accessed via quantum spin-mixing dynamics^[55,91-96], or via adiabatic passage through the quantum phase transition^[56-57,106].

CHAPTER 3 EXPERIMENTAL SYSTEM

The experiments described in this thesis were all performed in the BEC lab in the group of Prof. Dr. Philipp Treutlein at the University of Basel, Switzerland, during my visit under the support of the Chinese scholarship council. In our experiments, we use a compact experimental apparatus based on an atom chip to generate a mesoscopic condensate of about 1000 ^{87}Rb atoms as a starting point of the phase measurement and quantum enhanced interferometric sequence. This apparatus has been developed a decade ago^[3] and has been used to explore different fields of physics since then, for example, to image microwave fields^[107], to measure the magnetic fields^[19] and to generate quantum correlated states^[104]. All the details about the former versions of the apparatus can be found in the earlier doctoral dissertations^[3,50,103,105,108].

In this chapter, I will first present our experimental apparatus, focussing mainly on the parts that have been upgraded, characterized or recalibrated during my Ph.D. project. Then I will discuss the generation, manipulation and detection of a BEC on our apparatus in more detail, including the typical sequence used to prepare a BEC, the techniques used to manipulate the internal and external degrees of freedom of atoms in our experiment, and the precise detection of atoms in different internal states.

3.1 Overview of the apparatus

The apparatus is composed of the vacuum chamber, the atom chip, the laser system, the microwave and radio frequency system, several current sources, the detection system, and the control system.

3.1.1 Vacuum chamber

Figure 3.1 shows the central part of our experimental apparatus. Our experiments occur in the vacuum chamber (science chamber), whose top wall is formed by an atom chip (see in Figure 3.1(b)) which is glued to the glass cell. To the backside of the atom chip a U-shaped wire (BigU) is attached, which produces the strong quadrupolar magnetic field needed in the magneto-optical trapping (MOT) stage of the experimental sequence. The U-shaped wire and the atom chip are water cooled by the attached water cooling copper

block, which is connected in series to a chiller ^① and stabilizes the water temperature at about 19 °C.

The bottom of the glass cell is connected via a glass-to-metal adapter to a six-way cross, which then connects to an ion pump, a Ti-sublimation pump, an ion pressure gauge, and electrical feed-throughs for the Rb dispensers. The vacuum pressure is continuously maintained at a few times 10^{-10} mbar by the ion pump, whereas the Ti-sublimation pump is activated once several months when the pressure approaches 10^{-9} mbar.

Outside the vacuum chamber, there is a coil cage with three sets of coils configured in Helmholtz pairs, which generate approximately homogeneous magnetic fields B_x , B_y , B_z needed in experiments. Surrounding the coil cage, several fiber output couplers provide all the laser beams needed for experiments, more details can be found in section 3.1.3. A microwave horn and a radio frequency antenna are put near the chamber to provide the oscillating signal used for the evaporative cooling and the manipulation of the internal state of the atoms, see section 3.3. All the aforementioned elements are enclosed inside a μ -metal magnetic shielding in order to minimize the effects of the magnetic noise in the surrounding environment, see Figure 3.1(a).

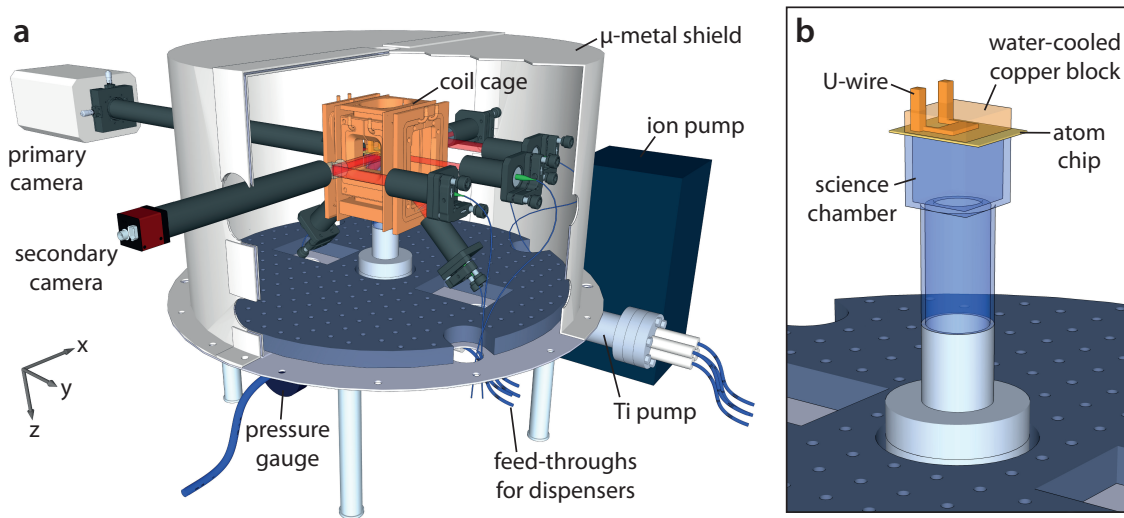


Figure 3.1 **Overview of the central part of the experimental apparatus.** (a) Schematic view inside the magnetic shielding, showing the vacuum chamber, the coil cage, the fiber couplers and imaging system. The microwave antenna and radio frequency horn are not shown. (b) The science chamber with the atom chip as top wall. Figure taken from Ref. [50].

3.1.2 Atom chip

The core of the apparatus is an atom chip. The atom chip used in our experiments was first designed and fabricated in Ref. [3] and since then it has been successfully used

^① ThermoCube 10-400LS

to explore new physics in experiments with trapped BECs^[19,29,102,104,109]. It is a multi-layer chip including a base chip and a science chip, both with patterned gold layers. The base chip is an ALN substrate providing mechanical support for the science chip. The mini-SMP connectors and standard 2.54 mm-pitched pin headers soldered on it serve as electric (DC and MW) connections. The science chip consists of micro-wires arranged in a two-layer structure, see Figure 3.2, through which we can send both DC currents and microwave currents in order to realize both DC and MW inhomogeneous magnetic fields. The top layer contains two parallel sets of wire structures (a five-wire and a six-wire structure). In the experiments present in this thesis we mainly use the three central wires of the five-wire structure, which constitute a MW co-planar wave guide. These wires can carry DC currents simultaneously fed via external bias tees.

For convenience, hereafter we define the coordinate system as shown in Figure 3.1, and we set the origin at the central wire of the five-wire structure so that the chip lies in the $x - y$ plane.

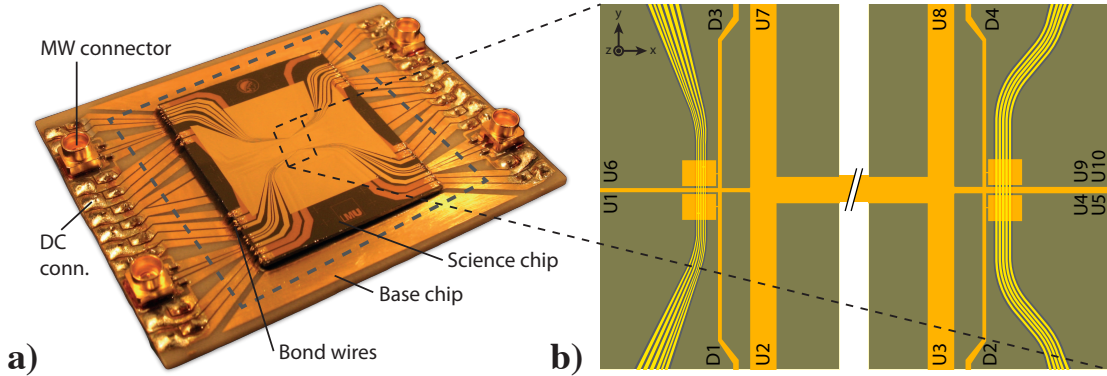


Figure 3.2 **a)** Photograph of the atom chip. The chip wires have rectangular cross-section. **b)** Drawing of the six- and five-wire structures, left and right respectively, at the chip center. A detailed illustration of the five-wire structure is given in Ref. [3,50].

Depending on the current configurations, we can generate different types of magnetic traps based on the atom chip^[3], details can be found in Appendix A. Two typical categories mainly used in our experiment are the *Ioffe-Pritchard trap* and the *Dimple trap*. Ioffe-Pritchard trap, as a two-dimensional quadratic trap, can be created by combining an on-chip wire structure that carries DC current and homogeneous bias fields perpendicular to the wire. For example, a wire along x -direction carrying current I_x that creates a magnetic field with concentric circular field lines whose centres lie on the wire, together with a bias fields that cancel the field at some distance from the wire, will form a two-

dimensional quadratic confinement. Dimple trap can then be created by adding another current-carrying wire along y direction, crossing the existing straight wire perpendicularly to modulate the field on axis $z = z_0$, therefore generate a three-dimensional trapping potential. Such Dimple traps can be describe as a harmonic potential. In our experiment, it is formed by three central wires of the five-wire structure on the science chip and a crossing wire (named ‘Long-Ioffe’) in the lower gold layer.

The atom chip helps to result in a very compact single-chamber apparatus. Conventional BEC apparatuses usually contain two or more vacuum chambers used for different cooling stages such as MOT and evaporative cooling, thus atoms need to be transferred in between chambers. However in our case, the proximity to the atom chip makes it possible to generate tight deep magnetic traps, allowing different stages of cooling to happen in the same chamber. Moreover, the BEC is finally trapped in chip-based magnetic potentials instead of optical dipole trap (as in conventional apparatuses), which is flexible to engineer with the chip.

3.1.3 Laser system

In our experiment, different laser frequencies are required for cooling, optical pumping and detection of the atoms, as shown in Figure 3.3. They are prepared on an optical table with a master (seed) laser, a tapered amplifier (TA) module, a slave laser and commercial optical elements. Figure 3.4 shows an up-to-date schematic of the optics in our experiment. All the lasers are operating at a wavelength of approximately 780 nm which corresponds to the Rubidium-87 D_2 line, see Figure 3.3.

The master laser is a home-built interference-filter stabilized diode laser, whose frequency is locked on the crossover transition $F = 2 \rightarrow F' = (1, 3)$ of a saturated absorption spectroscopy. The output light is injected into a tapered amplifier. After being amplified, the light is frequency-shifted by an acousto-optic modulator (AOM), through which we can adjust the laser frequency by controlling an analog voltage. The AOM is configured in double-pass way, so that the light approaches a frequency that is 15 MHz red detuned with respect to the $F = 2 \rightarrow F' = 3$ cycling transition (see Figure 3.3), which provides the *cooling light*. Apart from controlling the frequency of the cooling light, we also stabilize the power of the AOM driving RF with an analog PID Controller ^① to make sure the intensity of the cooling light stays constant. The output power of the TA is mostly used as cooling light during the MOT stage. The remainder is frequency-shifted to generate

^① Stanford Research Systems (SRS) SIM960

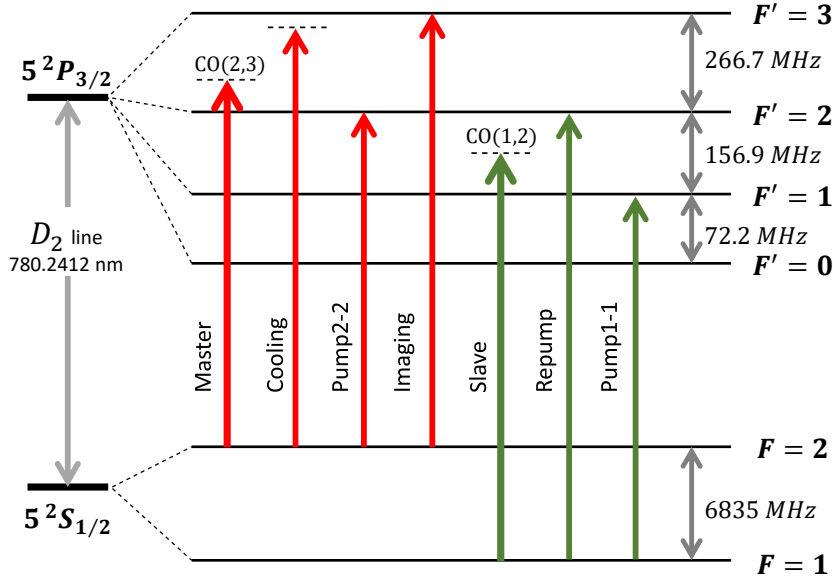


Figure 3.3 **Level scheme of the D2 line of ^{87}Rb .** The transitions used in our experiment are indicated. All frequencies are produced starting from a master laser (red) and a slave (green) laser, and shifted via acousto-optic modulators (AOMs).

Pump2-2 light (resonant to the transition $F = 2 \rightarrow F' = 2$) for optical pumping and *Imaging light* (resonant to the transition $F = 2 \rightarrow F' = 3$) for absorption imaging.

In practice, while driving the cyclic transition, there is also a possibility for the atoms to be excited to the $F' = 2$ state, then decay to the $F = 1$ state and thus escape from the trap. Therefore, we apply an optical repumping light (see Figure 3.3) resonant to the transition $F = 1 \rightarrow F' = 2$ to pump these atoms back into the cycling transition. The frequency of this transition is about 6.8 GHz away from the master laser, out of the modulation range of AOMs. To generate the light at this frequency, we use a second laser, which is frequency stabilized via an optical phase loop lock (OPLL) at a frequency difference of 6.705 GHz with the master laser. The light coming from this laser needs to be further frequency-shifted by AOMs to generate *Repump light* for the MOT stage, and also the *Pump1-1 light* resonant to the $F = 1 \rightarrow F' = 1$ transition for optical pumping stage.

After being frequency-adjusted, all the laser beams will pass through mechanical shutters that provide switching with high extinction ratio on the millisecond scale and are coupled into single-mode polarization-maintaining optical fibers. The MOT fiber and repump fiber are connected to a Schäfter & Kirchhoff fiber beam splitter with two input

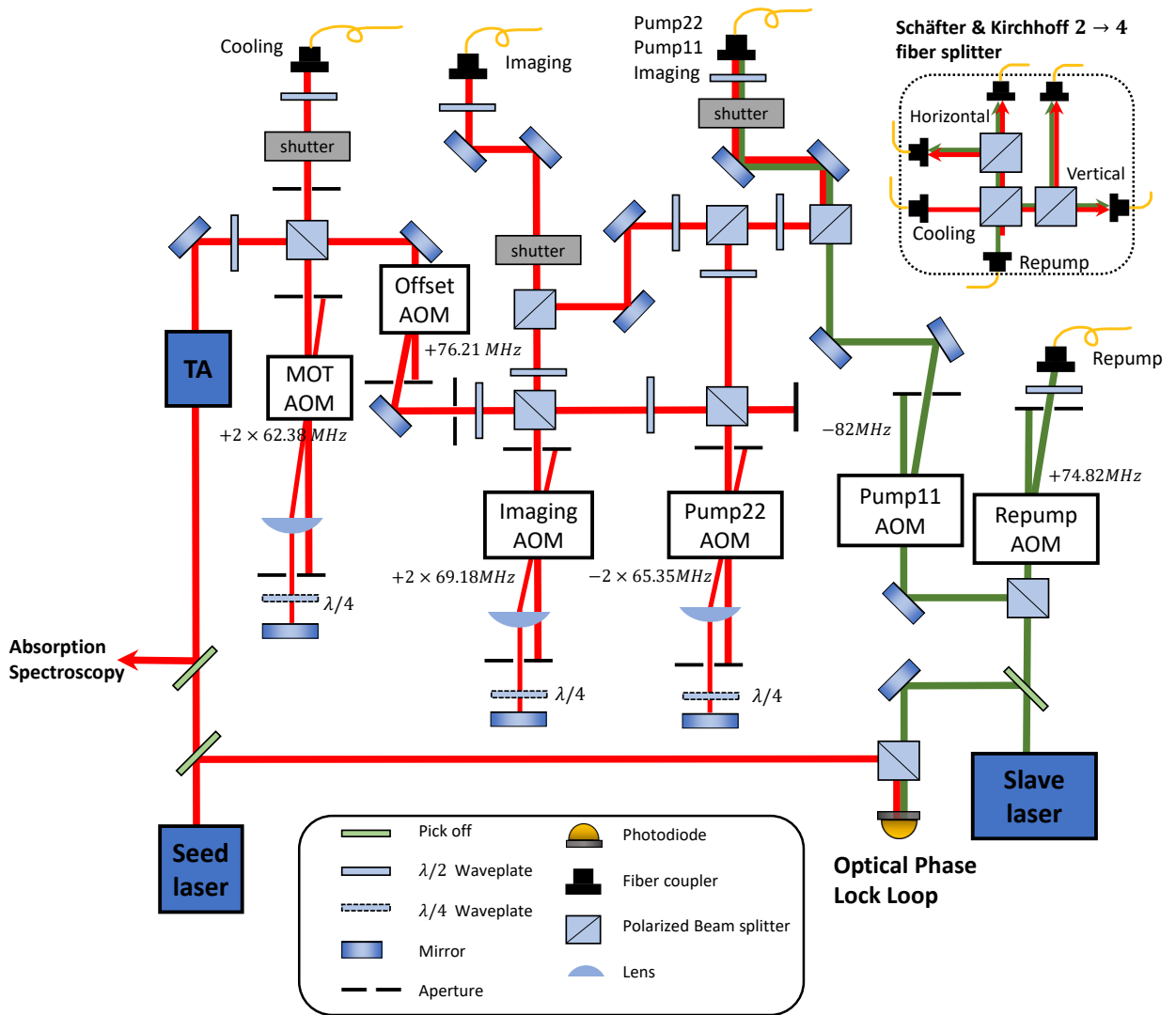


Figure 3.4 **Schematic of the laser system.** The typical seed laser output is around 30 mW. A part of it is picked up for the Rb saturated absorption spectroscopy and the rest is injected to a Tapered Amplifier (TA). The slave laser frequency is locked to the output from the master laser via an optical phase lock loop (OPLL) at 6705 MHz, which is designed and built by Simon Josephy. All output beams are coupled to polarization maintaining single-mode optical fibers. The cooling light and Repump light are sent to a Schäfer & Kirchhoff fiber splitter and split to 4 beams for the horizontal and vertical MOT beams. Frequency shifts by AOMs are indicated in the diagram.

ports and four output ports, result in four output beams which contain both cooling light and the repump light. They are brought inside the μ -metal shield to the vacuum chamber by fibers. After being out coupled and passing polarizing beam splitters and wave plates, they form two pairs of counter-propagating circularly polarized laser beams (diagonal and horizontal), which intersect at the center of the glass cell, as shown in Figure 3.5. On the base chip surrounding the micro-structures, a gold surface with high reflectance serves as a mirror. The two diagonal beams, pointing along $z \pm y$ directions, are reflected off

the chip surface and broad enough, providing cooling in both the y and z direction. Two horizontal beams provide cooling in the x direction. Together with the magnetic field generated by Helmholtz coils and the U-shaped wire, they form a mirror MOT as shown in Figure 3.5.

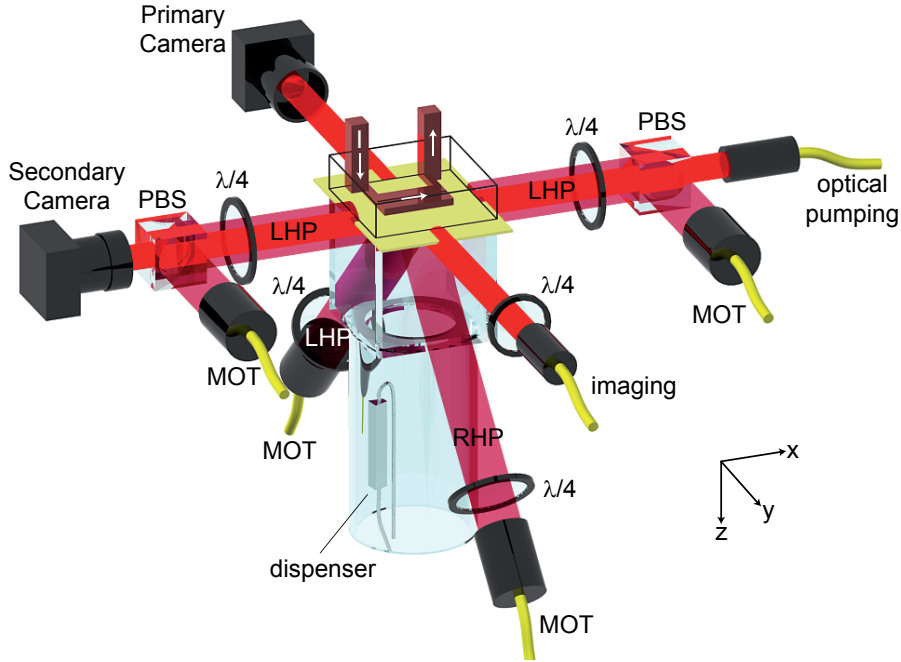


Figure 3.5 **Optics surrounding the science chamber.** Indicated are polarizing beam splitters (PBS), quarter-wave plates ($\lambda/4$), and right-hand and left-hand circular polarization of the MOT cooling beams (RHP and LHP, respectively). Figure adapted from^[3].

As a benchmark for laser powers, the typical output power of the master laser is around 30 mW. The tapered amplifier module is able to produce up to 3.5 W of output power at a current of 4.3 A. We use the amplifier at a lower working current of 2.5 A to amplify the laser power to around 1.7 W, which is sufficient for our use.

3.1.4 Current sources and their noise characterization

Current sources play an important role in our experiment apparatus. In our experiment, we need current sources that meet different requirements. The current sources used in the experiment are described in earlier theses [50,103,108,110]. Here we briefly summarized their up-to-date properties in Table. 3.1.

During the MOT stage, quadrupole fields are needed. The wires involved are two U-shaped wires (both are no more than a single turn), therefore large currents are required. A current of 52 A is sent through the external U-shaped wire (Big U), driven by a commercial

current source ^① which is unipolar and can provide current up to 70 A. For the U-shaped wire on the base chip (base-U) wire which is used to create a smaller MOT, a current of a few amperes is provided by another commercial current source ^②.

In the rest part of the sequence, currents are needed for the bias field coils to create (B_x, B_y, B_z), and for the other on-chip wires (including an Ioffe wire, a Long-Ioffe wire, a Dimple wire and three small co-planar wave guide wires) to generate all the static magnetic trapping potentials for the atoms. These wires and coils require currents from a few milliamperes to a few amperes. These currents are crucial since they determine the magnetic traps where the BEC is formed, and any current fluctuations will directly cause fluctuations in the atom number and decoherence of the BEC. Therefore current supplies with ultra-low noise and high stability are required.

For the bias fields we have three home-built bipolar current sources, which can output up to ± 5 A ^[110]. Besides, during some parts of the sequence we need to produce a stronger bias field in the y direction, so there is an additional set of coils driven by a commercial unipolar 15 A source ^③, which is disconnected after the BEC is created. For the chip wires Long-Ioffe, Ioffe, and Dimple, home-built current sources were developed with good noise performance, details can be found in Ref. [110]. The DC currents sent to the three small co-planar waveguide wires are used to create the final static traps where the main experiment is performed, therefore very critical (relative stability below 1×10^{-5} is required). They are generated by three battery-powered current sources ^④, which are designed to deliver up to ± 10 mA current, and have a short response time and a ultra low noise. Being powered by the battery provides a lower noise compared to the power supply based on switching or even linear converters. We recharge the battery whenever the current source is not used.

Some of the current sources have been operating for over a decade, and probably their performance has changed over time. Therefore, we characterize the noise and stability performance of all the aforementioned current sources ^⑤. For both measurements, a sampling resistor with small temperature coefficient ^⑥ is connected in series with the load as a current sensor (depending on the current sources we choose different resistance).

^① Delta Electronic SM45-75D

^② High Finesse BCS106

^③ FUG NLN 350M-20

^④ High Finesse BCS 002/10, later replaced by a home-built one developed in May, 2020

^⑤ The measurement are performed in July, 2020

^⑥ Vishay VCS332

Table 3.1 Characterization of current sources

coil(wire)	manufacturer	output range	high frequency noise	long-term stability drift
Bias field (x)	home-built	± 5 A	10^{-5}	2×10^{-5}
Bias field (y)	home-built	± 5 A	5×10^{-5}	10^{-5}
Bias field (z)	home-built	± 5 A	10^{-4}	10^{-5}
Bias field (y)	Fug	15 A	10^{-3}	10^{-3}
Long-Ioffe	home-built	± 1 A	10^{-4}	10^{-3}
Ioffe	home-built	± 3 A	4×10^{-4}	5×10^{-3}
Dimple	home-built	+0.5 A	10^{-3}	2×10^{-4}
Base U	High Finesse	± 10 A	2×10^{-5}	3×10^{-4}
three small wires	High Finesse	± 10 mA	10^{-3}	10^{-2}

The voltage drop across the sensing resistor is amplified by an ultra-low noise and high gain pre-amplifier^①. The high input impedance of the pre-amplifier ensures the accuracy of the current measurement, while its high-gain (up to 10^4) keeps the overall noise factor of the measurement system determined by the ultra-low input noise ($4 \text{ nV}/\sqrt{\text{Hz}}$) of the pre-amplifier. Since the current signal is composed of a large DC component (mean value) and small fluctuations, we have to take the large DC part out in order to apply high amplification gain and thus to have better sensitivity for the measurements.

We use two different configurations for the measurements of fast current noise and long term current drift. For the fast noise measurement, we use the AC coupling mode of the pre-amplifier module to filter out the DC component and amplify only the higher frequency noise. We configure the input filters as a 6 dB/oct rolloff band-pass filter, with cut-off frequencies set at 3 Hz and 30 kHz, and set the output impedance to 50 Ω . The output is then connected to an oscilloscope for a convenient check of AC current noise. For the long-term drift measurement, we switch the pre-amplifier to differential mode, apply an additional reference voltage signal^② to the second input port of the pre-amplifier module, and adjust the sign of second input ports to shift the mean value (DC part) of the signal to around zero. The output is then connected to a data logger^③ to be recorded. We typically record the current drifts for at least 12 hours. An example plot of the recorded long-term stability is shown in Figure 3.6, where the relative stability is

① Stanford Research Systems(SRS) low-noise voltage pre-amplifier SR560

② The reference voltage has been characterized by the membrane lab in our group and we trust its long-term stability to be better than the current sources.

③ Agilent DAQ970A

defined as $x_i^{\text{rel. stab.}} = (I_i - \bar{I})/\bar{I}$. The complete results of the noise characterization are shown in Table 3.1. Since the small-wire current sources showed an inadequate performance, we decided to develop a new generation of current sources on May, 2020. The new current sources have been implemented in the experiment, whereas for most of the experiments presented in this thesis we were still using the old ones.

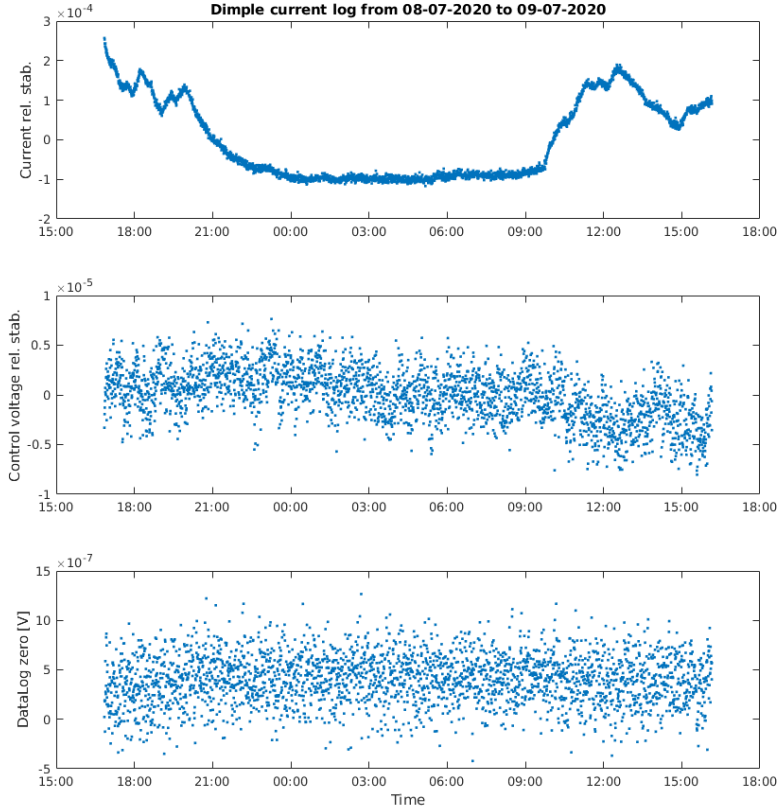


Figure 3.6 **An example for the result of the long term stability measurement over 24 hours.** Top panel shows the current drift of home-built current source for Dimple wire, the middle panel shows the long-stability of the analog signal from I/O card that is used as control voltage of the current source, and the bottom panel shows the record of the ground voltage of the data logger.

3.1.5 Microwave and radio-frequency electronics

In our experiment, we have a radio frequency system, an on-chip microwave system and an off-chip microwave system, for several purposes.

The off-chip microwave system is designed for the requirement of the homogeneous microwave field. To minimize the spatial inhomogeneity, a microwave horn ^① is placed inside the μ -metal shield, providing a homogeneous (with respect to the size of the cloud)

^① in fact, a mutilated coupler of the A-Info LB-OH-159-15-C-SF microwave horn

MW magnetic field near the chip. The MW signal of ≈ 6.8 GHz is provided by a Rohde & Schwarz SGS100A signal generator, and it is amplified and power stabilized (details see in Ref. [50]). The homogeneous MW field is mainly used to manipulate the internal state of the atoms. It allows to drive Rabi transitions between states $|1, m_F\rangle$ and $|2, m_F\rangle$, or “dress” the internal state with an off-resonant frequency. The manipulation of the atoms will be discussed in detail in section 3.3.

The on-chip microwave is mainly used for generating a large gradient of MW field near chip which we use to obtain the state-dependent potential (see in section 3.3.3). To do this, a ≈ 6.8 GHz signal generated by an Agilent E8257D is power amplified, stabilized and sent to the co-planar wave guide on the science chip through a bias tee, details see in Ref. [50]. The maximum field gradient depends on the size of the transmission-line conductors and the distance between the atomic cloud and the waveguide. Already milliwatts of microwave power result in sufficiently strong gradients needed for the experiment, with which trapping potential minima for the two states can be split on the micrometer scale.

The evaporative cooling requires a homogeneous RF field near the chip, emitted from a home-built RF coil. The coil is of square shape (3 cm side length) with 9 windings, connected in series with a 10Ω resistor. The RF signal is generated from a commercial function generator called VFG150^① using direct digital synthesis (DDS) at a sample rate of 200 MHz. The signal is sent to a RF switch^②, which is driven by the transistor–transistor logic signal (TTL) output from VFG in sync with the RF signal with a time resolution of 5 ns. After the switch, the RF signal is power amplified by a commercial amplifier^③ and fed to the RF coil. A 6 dB attenuator is inserted^④ in between the RF amplifier and the RF coil to weaken the back reflections resulting from the impedance mismatching. The back-reflections are unavoidable, given the fact that the antenna is a coil and that we use a very broad frequency range (2 to 14 MHz) over the sequence.

Coherent manipulation of atoms is crucial for our experiments. In order to obtain an adequate level of phase coherence in the manipulation of the atoms, we reference both MW and RF signals to a 10 MHz GPS-disciplined quartz clock as our local oscillator^⑤. The quartz oscillator provides very good short-term stability (Allan deviation better than 1×10^{-9} in 1 s), and it is synchronized with time signals obtained from GPS satellites to

① versatile function generator (VFG) 150

② MiniCircuits ZASWA-2-50DR

③ MiniCircuits LZY-22+, 100 kHz – 200 MHz, 43 dB gain, 30 W output power

④ MiniCircuits BW-S6W20+

⑤ SRS FS752

improve long-term stability (Allan deviation better than 1×10^{-12} in 1000 s).

To summarize this section, we present several parts of the experimental apparatus: the vacuum, the atom chip, the laser system which provides all the required lights, the low noise current sources providing current for the chip and coils, microwave (MW) and radio-frequency (RF) electronics. Besides, there are other electronics driving the acousto-optic modulators and shutters. And the whole apparatus is controlled, with the help of National Instrument (NI) I/O cards, which provide digital and analog outputs and can be programmed. The experiment can be run with a computer sequence, which programs the I/O card and also other devices such as the VFG.

3.2 Preparation of a ^{87}Rb Bose-Einstein Condensate on an atom chip

In our experiment, in order to create a BEC, the atoms experience several stages, namely the magneto-optical trap (MOT), optical molasses, optical pumping, a series of magnetic traps, and finally evaporative cooling by RF field.

The experiment starts by capturing Rb atoms from the background vapor with the MOT. In a MOT, the cooling results from the radiation pressure exerted by red-detuned laser beams, and the spatial confinement is due to the interplay between the space-dependent Zeeman shift and the frequency-dependent radiation pressure. In the first stage, “MOT-1”, the magnetic quadrupole field is created by sending a current of 52 A through the external U-shaped wire (named Big-U) behind the chip. To provide the radiation pressure forces, the cooling laser is $\approx 2.9\Gamma$ red-detuned from the resonance, where $\Gamma = 2\pi \times 6$ MHz is the natural linewidth of the cooling transition. The parameters in MOT-1 are optimized to collect as many atoms from the background gas as possible. In the subsequent stage called “MOT-2”, we turn off the current on the Big-U to release atoms, then re-capture them in a smaller MOT created by a current of 3.3 A in another U-shaped wire on the base chip (named Base-U), and with a laser detuning of -6Γ . The purpose of this stage is to compress the atomic cloud to achieve a higher density and to locate the MOT at a place closer to where we can produce the later magnetic traps. After the MOT-2, the magnetic field gradients are switched off and the cooling lasers are ramped to far red detuned (-15.5Γ) for an optical molasses stage. In our experiment, with a MOT loading time of approximately 14 s, around 3×10^5 Rb atoms are captured from the background gas and cooled to 4 μK at the end of Molasses.

After the molasses stage, atoms need to be pumped to a low-field seeking state to be ready for the subsequent magnetic trapping stages. By applying $\sigma-$ polarized pump 1-1 and pump 2-2 light, the atoms end up in the $|F = 1, m_F = -1\rangle$ state after scattering a few photons. Note that, alternatively, one can prepare the atoms in $|F = 2, m_f = 2\rangle$ by using the pump 2-2 light and the repump light both with $\sigma+$ polarization. However, this has the disadvantage that in the $F = 2$ manifold there are two magnetically trappable states. It is impossible to blow away atoms in unwanted state selectively since linewidth of the imaging transition being larger than the frequency difference between the two states, leading to a mixture of the two states. For this reason we choose $|F = 1, m_F = -1\rangle$ as the starting point of the BEC. Actually, some atoms might remain in $F = 2$ manifold after the optical pumping, so what follows is a “blow away” pulse, *i.e.*, a 70 μs pulse of resonant imaging light to push away atoms in the $F = 2$ by radiation pressure.

After the optical pumping, we re-capture the atoms with magnetic traps. The magnetic traps based on current-carrying wires are a common technique used in the next stages. In Appendix A, a detailed discussion of the typical magnetic traps involved in our experiment and their parameters can be found.

The first magnetic trap in the sequence is “Ioffe1”, which is relatively far away from the chip surface, approximately 140 μm . What follows is a transfer of the atoms through a series of other “Ioffe” traps. During the transfer, each next trap is tighter and closer to the chip surface, so that the atoms are compressed further as well as transferred towards the chip. In the last Ioffe trap, around $\approx 2 \times 10^5$ atoms are trapped at a temperature of 1.6 μK ^①.

The atoms are then loaded into Dimple traps. To further decrease the temperature, we perform evaporative cooling via RF ramps. RF fields are used to selectively remove hot atoms from the trap by inducing transitions between trappable and non-trappable spin states. The confined atoms in thermodynamic equilibrium obey a Maxwell-Boltzmann distribution of the velocities. These atoms inside the highest velocity tail of the distribution, tend to reach larger distances from the trap center and thus have on average larger Zeeman shift. Therefore they are closer to resonance with the RF field, easier to be transferred to untrappable state and thus removed from the trap. While these most energetic atoms escape, the equilibrium of the system is broken and a rethermalization of the remaining population takes place. When the frequency of the RF field is ramped down, the

① The atom number and temperature in Ioffe trap is measured after a hold time of 500 ms.

mean kinetic energy of the atom cloud gradually decreases with rethermalization, cooling the entire ensemble. A quick enough rethermalization is crucial for the evaporative cooling. Since it happens mainly through the atomic collisions, a high atomic density in the magnetic trap is required. For this reason, the traps in which RF cooling is performed are designed to be very tight and steep.

The first ramp takes place in “Dimple-5” (trap depth 4.8 MHz) with an exponential RF ramp (RF1) from 14 \rightarrow 2.2 MHz during 2 s. We then transfer atoms to the next trap “Dimple-6” (trap depth 1.2 MHz) to perform the second RF ramp (RF2) from 2.2 \rightarrow 1.84 MHz during 1 s. At the end of this RF ramp the atoms find themselves at a BEC of \approx 1700 atoms. Finally, we transfer the BEC to the final trap “Dimple-7”. To set the final atom number in the BEC, we apply another RF pulse (RF3) of 20 ms at a low power. The frequency of this RF pulse can be chosen to obtain the desired atom number in the BEC. The key parameters of the traps mentioned above are described in Appendix A.

During the whole process of the BEC preparation, there are a lot of parameters which could be optimized experimentally, but it is practically impossible to find a global optimum in such a complex process. For a straightforward comparison of the transfer efficiency (or cooling efficiency) from one stage to another, we usually measure and compare the atom numbers in three stages: molasses, the first Ioffe trap, and the BEC (after the second RF ramp), as a function of the MOT-1 loading time, see Figure. 3.7. The loading efficiency from Molasses to Ioffe trap is usually approximately 70%, independent of the MOT-1 loading time. The cooling efficiency from Ioffe trap to the BEC depends on the atomic density, therefore on the MOT-1 loading time. We take such loading measurement from time to time to ensure a high efficiency of BEC preparation.

After the BEC has been produced, we perform the main experiments in Dimple-7, with a trap frequency of (714, 714, 114) Hz. The chip trap usually provides a strong confinement for the BEC, therefore the interactions between atoms are so strong that the external degree of freedom in our experiment does not play an important role, which is contrary to other experiments such as in atomic fountains or beams.

The operations involved in the main experiments usually consist entirely of RF and MW pulses, which are used to manipulate the internal state of the BEC. After this, we take absorption images of atoms in the time of flight (TOF). From the images we can detect atom numbers precisely, which is the most important observable giving access to the spin state. The precise detection of atom numbers are described in section 3.4. After the main

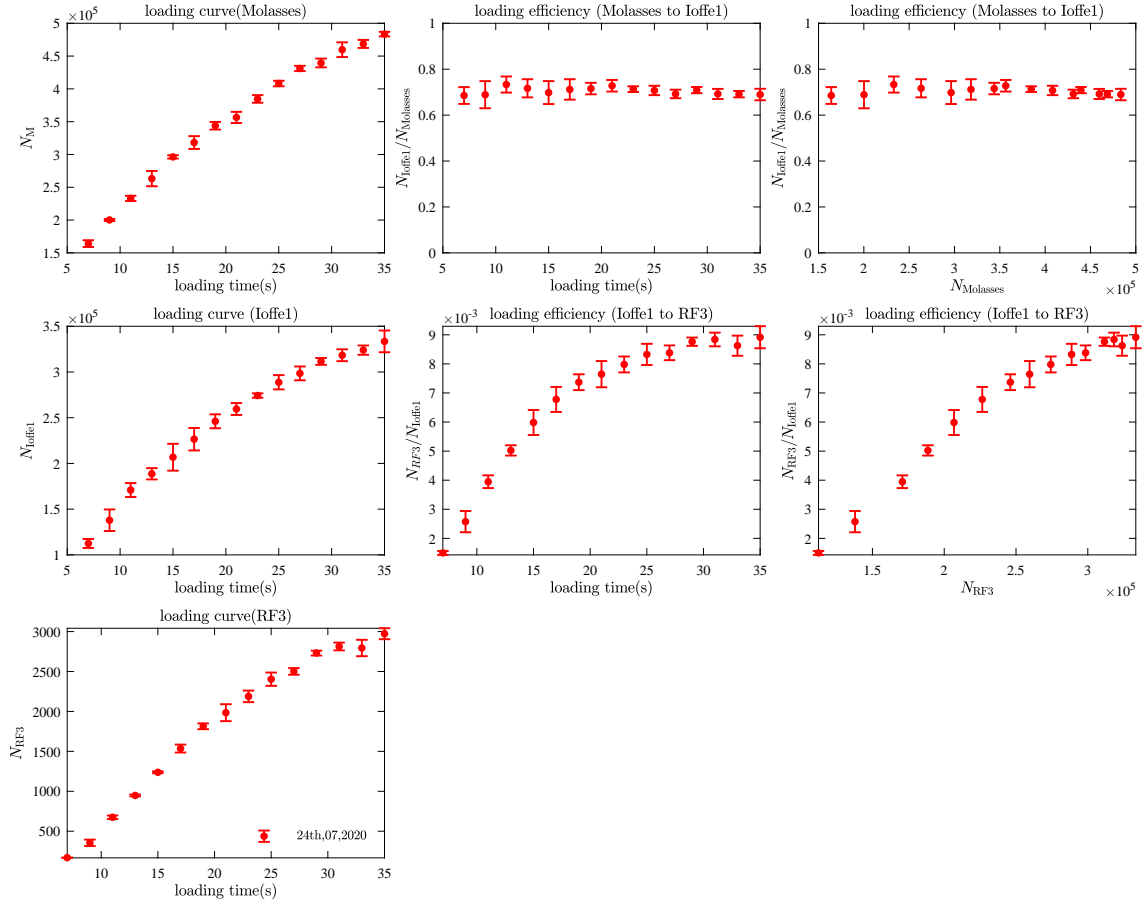


Figure 3.7 **Loading curves and loading efficiency curves.** The Left column is the measured atom number as a function of the MOT loading time in different stages (at the end of Molasses, first Ioffe trap and RF3 ramp); the middle column is the loading efficiency from one stage to another as a function of the MOT loading time; the right column shows the loading efficiency as a function of the atom number in the prior stage. The loading efficiency from stage ‘Ioffel’ to stage ‘RF3’ actually shows the efficiency of our evaporative cooling, which increases with the atom number in the Ioffe trap. The evaporative cooling rely on the atomic density, leading to a higher efficiency for larger atom numbers.

experiment and before we take the absorption images, a kick-out procedure is applied to accelerate the atoms away from the chip surface. This allows absorption imaging with a shorter TOF, such that the cloud size in the absorption image is small, reducing detection noise. The kick-out procedure is described in detail in Ref. [50]. The BEC is destroyed during the absorption imaging since atoms scatter photons and are heated. Therefore, for each shot of the experiment, the whole sequence has to be repeated.

3.3 Manipulation of atoms

The main experimental sequence relies on manipulating neutral ^{87}Rb atoms using both static and microwave electromagnetic fields. In this section, the basic theory about

the atom-field interaction is briefly introduced, then the techniques frequently used in the experiments are discussed, including the Rabi coupling, the two-photon Rabi transition used to couple our state pair, and the state-dependent trapping potential.

3.3.1 Theory of atom-field interaction

The atom-field interaction has been studied intensively in the textbooks, and it suffices here to briefly mention a few results that are needed for the understanding of our experiment. Our physical system is an ensemble of ultra-cold ^{87}Rb atoms placed in an external magnetic field \mathbf{B} and irradiated by MW and RF field with frequency ω_{mw} and ω_{rf} . We consider the energy of one single atom in presence of external fields, thus neglect the inter-atomic interactions for the moment. To describe the energy levels of an atom in such a system, one needs to consider the hyperfine energies, the static Zeeman effect and the dressing due to interaction between atoms and the MW/RF field.

3.3.1.1 Hyperfine splitting and static Zeeman effect

Atoms in a static magnetic field $\vec{\mathbf{B}}$ are described by the well-known Breit-Rabi Hamiltonian

$$H_{\text{BR}} = A_{\text{hfs}} \hat{\mathbf{I}} \cdot \hat{\mathbf{J}} + \mu_B (g_J \hat{\mathbf{J}} + g_I \hat{\mathbf{I}}) \cdot \vec{\mathbf{B}}, \quad (3.1)$$

The first term describes the hyperfine coupling between the nuclear and electron spin, and the second term describes the coupling of atoms and static magnetic field. Here A_{hfs} is the magnetic dipole constant of the manifold, μ_B is the Bohr magneton, $\hat{\mathbf{I}}$ and $\hat{\mathbf{J}}$ are the nuclear and electron angular momentum and g_I and g_J are the corresponding Landé g -factors. For ^{87}Rb , $2A_{\text{hfs}} = E_{\text{hfs}} = h \times 6.834682611 \text{ GHz}$, $g_J \approx 2$, and $g_I \approx -1 \times 10^{-3}$ [111].

For the ground states of a ^{87}Rb atom, $I = 3/2$ and $J = 1/2$. The diagonalization of the above Hamiltonian results in the eigenenergies [111-112]

$$E(F = \frac{3}{2} \pm \frac{1}{2}, m_F) = -\frac{A_{\text{hfs}}}{4} + g_I \mu_B m_F B \pm A_{\text{hfs}} \sqrt{1 + m_F x + x^2}. \quad (3.2)$$

where $x = 2(g_J - g_I) \mu_B B / A_{\text{hfs}}$, the magnetic quantum number m_F describes the projection of F onto the direction of \mathbf{B} . This Hamiltonian yields 8 eigenstates for the $5^2S_{1/2}$ ground states, grouped in two manifolds $|F = 1\rangle$ and $|F = 2\rangle$. The two manifolds are separated in energy by E_{hfs} . The hyperfine energy levels of the ground states in this regime is shown in Figure 3.8, with magnetically trappable states indicated.

Under a weak static magnetic field $\vec{\mathbf{B}}$ satisfying $\mu_B \vec{\mathbf{B}} \ll E_{\text{hfs}}$, we can simplify the

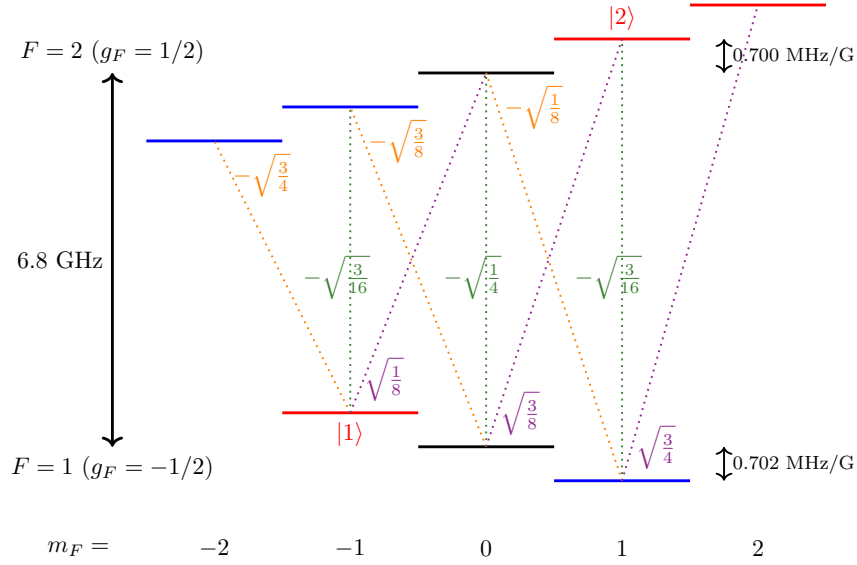


Figure 3.8 **Energy levels of hyperfine ground state manifold under a $B = 3.229$ G.** The trappable, untrappable and anti-trapped states are indicated with red, black and blue, respectively. We normally use two clock states $|1\rangle$ and $|2\rangle$ for interferometry. The microwave transitions with different polarization are indicated with dashed lines, with orange for σ^- , green for π and purple for σ^+ polarization. The labels show the matrix elements of the corresponding transitions.

above Zeeman splitting to the second order within each F -manifold,

$$E(F = 1) \approx -\frac{5}{8}E_{\text{hfs}} + a_1 m_F B - b_{m_F} B^2, \quad (3.3)$$

$$E(F = 2) \approx \frac{3}{8}E_{\text{hfs}} + a_2 m_F B - b_{m_F} B^2 \quad (3.4)$$

where the first order coefficients are

$$a_1 = g_I \mu_B - \frac{A_{\text{hfs}} x}{8} \approx -0.702 \text{ MHz/G}, \quad (3.5)$$

$$a_2 = g_I \mu_B + \frac{A_{\text{hfs}} x}{8} \approx 0.700 \text{ MHz/G}, \quad (3.6)$$

which gives the linear Zeeman shifts of 0.702 MHz/G and 0.700 MHz/G, in $F = 1$ and $F = 2$ manifolds, respectively. The second terms scale quadratically with the magnetic field with a coefficient of

$$b_{m_F} = \frac{A_{\text{hfs}} x^2}{8} \left(1 - \frac{m_F^2}{4}\right) \approx (72m_F^2 - 288) \text{ Hz/G} \quad (3.7)$$

In the 8 states, $|1\rangle \equiv |F = 1, m_F = -1\rangle$ and $|2\rangle \equiv |F = 2, m_F = 1\rangle$ are of special interest for two reasons. First, these two states are weak-field-seeking states, which can be trapped in the magnetic field (it is impossible to trap strong-field-seeking states since the maximum of magnetic field does not exist). Second, these two states experience nearly identical magnetic trapping potentials due to their nearly equal magnetic moments. Their

relative linear Zeeman shift is zero in a specific magnetic field $B_0 \approx 3.228917$ G, which is called the *magic field*. In the experiments described in next chapters, we prepare the atoms at the magic field so that the superposition of the two internal states $|1\rangle$ and $|2\rangle$ is robust against magnetic field fluctuations. These two states are well suited as so-called “clock states” and extensively used in other ^{87}Rb experiments aiming at the construction of atomic clocks. Coherence times of the superposition of the two states up to seconds^[5] and even one minute^[82] have been reported.

However, the clock states are not completely insensitive to the magnetic field. Near the magic field B_0 , the quadratic Zeeman effect also contributes to the differential energy shift of the states and the transition frequency between $|1, -1\rangle$ and $|2, 1\rangle$ (in the rotating frame) can be written as a function of the magnetic field

$$\Delta E/h = \frac{1}{h} (E_{|2,1\rangle} - E_{|1,-1\rangle} - E_{\text{hfs}}) \approx c + k(B - B_0)^2,$$

with $c = -4.497$ kHz, and a curvature $k = b_{m_F=-1} - b_{m_F=2} = 2\pi \times 431.35957$ Hz/G².

For our experiment it is very important to tune the static field in the x -direction to ensure that the magnetic field at the trap center is near the magic field of 3.23 G. Taking the advantage of the magnetic field dependence of the energy shift, we calibrate the external magnetic field by performing a spectroscopy of the transition $|1, -1\rangle \leftrightarrow |2, 0\rangle$. In the experiment, we prepare all the atom in state $|1, -1\rangle$ and use a weak MW pulse of 10 ms to probe the atoms. By varying the frequency of the MW pulse and counting the atoms remaining, we obtain the spectroscopy as shown in Figure 3.9, right panel. The resonant microwave frequency should match the theoretical value expected from the differential Zeeman shift when B_x is well calibrated. We can then adjust B_x by tuning the current being sent to the corresponding coil according to the resonant frequency.

3.3.1.2 Interaction with the microwave field

Let us take the interaction between the atom and microwave field into consideration. Under the exposure to a microwave field oscillating at a frequency of $\omega \approx 6.8$ GHz, the atom will interact with both the magnetic field and the electric field of the microwave. The magnetic field can drive magnetic dipole transitions between $|1, m_F\rangle$ and $|2, m'_F\rangle$ states, causing the AC Zeeman effect. The interaction with the microwave electric field causes the so-called AC Stark shift, which is identical for all the bare states $|F, m_F\rangle$ and is also much smaller than the AC Zeeman shift. In the remainder of this thesis we ignore the AC Stark shift and mainly consider the interaction between atoms and the microwave

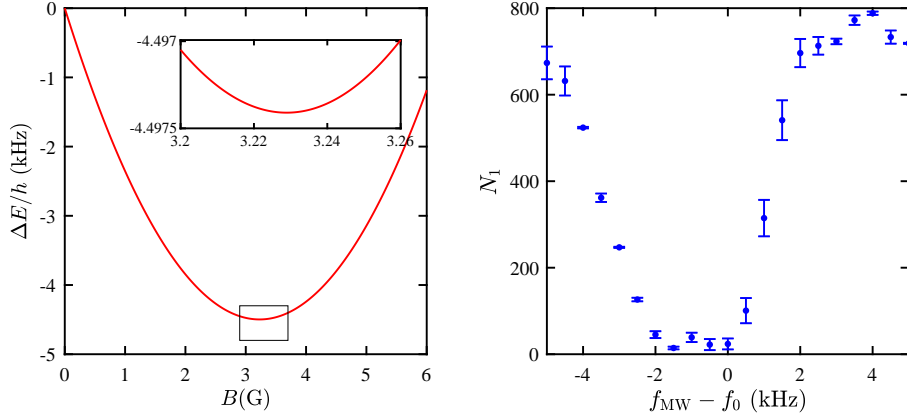


Figure 3.9 **Zeeman splitting and Rabi spectroscopy.** Left panel shows the magnetic field dependence of the energy difference due to Zeeman splitting between $|1, -1\rangle$ and $|2, 1\rangle$. The inset shows a blow up of the rectangular region, indicating the small slope near the magic field. Right panel shows the experimental result of the Rabi spectroscopy, with x -axis showing the difference between the applied microwave frequency and the expected transition frequency between two states under the magic field. If the external field is well calibrated, the remaining atom numbers will be minimum when $f_{\text{MW}} = f_0 \approx 6834678.1$ kHz.

magnetic fields B_{mw} .

A complete description of the dressing picture requires to treat the microwave field \hat{B}_{mw} as a quantized field, and to consider the Hamiltonian of the whole atom-field system, which is^[3]

$$H = H_{\text{BR}} + H_{\text{F}} + H_{\text{AF}} \quad (3.8)$$

$$= H_{\text{BR}} + \hbar\omega(\hat{a}^\dagger\hat{a} + \frac{1}{2}) + \mu_B(g_J\hat{J} + g_I\hat{I}) \cdot \hat{B}_{\text{mw}}. \quad (3.9)$$

The first term is the Breit-Rabi Hamiltonian. The second term H_{F} represents the energy of the microwave field, with photon number $\hat{n} = \hat{a}^\dagger\hat{a}$, where \hat{a}^\dagger and \hat{a} are the creation and annihilation operators, respectively. The third term H_{AF} is the atom-field interaction, where $\hat{B}_{\text{mw}} = \sqrt{\hbar\omega\mu_0/2V}(\vec{e}\hat{a} + \vec{e}^*\hat{a}^\dagger)$ is the field operator with unit polarization vector \vec{e} .

A complete solution of this Hamiltonian yields a “ladder” of energy levels^[3]. Details about the quantized description can be seen in Ref. [3]. Here we simplify the problem by considering a classical field. For a mean photon number $n \gg 1$, which is well satisfied for our experimental parameters, the MW field can be described as a classical field

$$\vec{B}_{\text{mw}}(t) = B_{\text{mw}}\frac{1}{2}(\vec{e}e^{-i\omega t} + \vec{e}^*e^{i\omega t}). \quad (3.10)$$

In addition, we can make the rotating wave approximation, given that our system parameters satisfy the following weak coupling conditions: a monochromatic field mode at ω with a small detuning $\Delta_0 = \omega - \omega_0 \ll \omega_0$, and a small static magnetic field $\mu_B B \ll E_{\text{hfs}}$, and a small microwave magnetic field amplitude $\mu_B B_{\text{mw}} \ll E_{\text{hfs}}$. The resulting Hamil-

tonian in the $|F, m_F\rangle$ basis is

$$\begin{aligned}
 H = & \sum_{m_2} \left(-\frac{1}{2} \hbar \Delta_{1,m_1}^{2,m_2} + g_2 \mu_B m_2 B \right) |2, m_2\rangle \langle 2, m_2| \\
 & + \sum_{m_1} \left(+\frac{1}{2} \hbar \Delta_{1,m_1}^{2,m_2} + g_1 \mu_B m_1 B \right) |1, m_1\rangle \langle 1, m_1| \\
 & + \sum_{m_1, m_2} \left(\frac{1}{2} \hbar \Omega_{1,m_1}^{2,m_2} |2, m_2\rangle \langle 1, m_2| + h.c. \right).
 \end{aligned} \tag{3.11}$$

The diagonal elements represent the energies of the bare states in the rotating frame. The off-diagonal elements denote the coupling between the two states, where the coupling strength is characterized by the Rabi frequency

$$\Omega_{1,m_1}^{2,m_2} = \mu_B B_{\text{mw}} \langle 2, m_2 | \vec{\epsilon} \cdot \vec{J} | 1, m_1 \rangle. \tag{3.12}$$

These couplings can be separated into linearly polarized π transitions sensitive to $\vec{\epsilon} \cdot \vec{e}_z$, corresponding to $\Delta m_F = 0$, and circular polarized σ^\pm transitions sensitive to $\vec{\epsilon} \cdot (\vec{e}_x \pm i\vec{e}_y)/\sqrt{2}$, corresponding to $\Delta m_F = \pm 1$.

Taking the interaction into consideration, the eigenstates of the atoms are no longer the bare states $|F, m_F\rangle$, but a superposition of them. The eigenenergies are shifted compared to the energies given by the Breit-Rabi Hamiltonian (Equation 3.2). When the field frequency ω is resonant to a transition, $\Delta_{1,m_1}^{2,m_2} = 0$, in the rotating frame, the energy shift caused by dressing is $\Delta E = E_{|1,m_1\rangle} - E_{|2,m_2\rangle} = \hbar \Omega_{1,m_1}^{2,m_2}$. The splitting between two energy levels is equal to the Rabi frequency. The effect is known as *avoided crossing*.

If the MW field is far detuned from any possible transition, that is when $|\Omega_{1,m_1}^{2,m_2}| \ll |\Delta_{1,m_1}^{2,m_2}|$ for all combinations of m_1, m_2 , the eigenstates (dressed state) are very close to the bare $|F, m_F\rangle$ states and their energies are well described by summing the AC Zeeman shift contributions from each off-resonant transitions

$$E_{|F, m_F\rangle} \approx E_Z \mp \frac{\hbar}{2} \left(\sum \frac{|\Omega_{1,m_1}^{2,m_2}|^2}{2\Delta_{1,m_1}^{2,m_2}} - \Delta_{1,m_1}^{2,m_2} \right), \tag{3.13}$$

where the sum runs over all levels coupled to $|F, m_F\rangle$ and the minus (plus) sign corresponds to $F = 1$ ($F = 2$).

Note that the magnetic dipole transition between adjacent m_F levels can also be driven by a RF field at typically a few MHz and also cause the AC Zeeman shift, similarly as in the microwave case. Moreover, for linear radio frequency polarization (as in our case), the shifts are almost identical for $|1\rangle$ and $|2\rangle$ and thus do not lead to a shift of the transition frequency and will not be discussed further.

3.3.2 Rabi Oscillations

Following the discussion of atom-field interaction in the last section, let us now discuss the Rabi oscillation, which is important for our experiment, since we use Rabi processes to manipulate the internal state of the atoms (with both single-photon and two-photon transitions). It is worth mentioning that, for the experiments described in this section, the MW field is generated by a rectangular waveguide placed relatively far away from the chip. The MW field gradients are very weak in the far field of such a waveguide and the field can be regarded as spatially homogeneous near the chip with respect to the size of atomic cloud, therefore we can neglect the spatial dependence of the AC Zeeman shift.

3.3.2.1 Single photon Rabi coupling

For simplicity we consider only two levels labelled as $|1\rangle$ and $|2\rangle$ with an energy difference of $\hbar\omega_0$. The radiation field frequency is ω , detuned from the resonant frequency by $\Delta_0 = \omega - \omega_0$. In practice, the oscillating field can be a microwave field (MW) at 6.8 GHz or a radio frequency (RF) field at a few MHz, corresponding to the transition between states in different $|F\rangle$ manifolds or the adjacent states in the same manifold.

Following the Equation 3.11, we can write the Hamiltonian of such a two-level system in the rotating frame,

$$H = \frac{\hbar}{2} \begin{pmatrix} \Delta_0 & \Omega^* \\ \Omega & -\Delta_0 \end{pmatrix}. \quad (3.14)$$

Similar to Equation 3.12, the diagonal elements represent the energies of the bare states in the rotating frame while the off-diagonal elements denote the coupling between the two states. Note that the Hamiltonian is written in the basis of $\{|1\rangle, |2\rangle\}$, however, under the illumination of the coupling field, the two bare states are mixed and are thus not the eigenstates of the system anymore. Therefore if the atoms are initially prepared in the bare state $|1\rangle$, the population will oscillate with frequency Ω_{eff} and the probability of finding atoms in $|2\rangle$ are

$$P_2 = \frac{\Omega^2}{\Omega_{\text{eff}}^2} \sin^2 \left(\frac{\Omega_{\text{eff}} t}{2} \right). \quad (3.15)$$

This is the *Rabi oscillation* between the two levels, and $\Omega_{\text{eff}} = \sqrt{|\Omega|^2 + \Delta_0^2}$ is the *effective Rabi frequency*. In our experiment, we usually measure the relative atom number $n_{\text{rel}} = \frac{N_1 - N_2}{N_1 + N_2}$ as readout, where N_1 and N_2 are the atom numbers in the two states. The Rabi

oscillation gives

$$n_{\text{rel}} = 1 - \frac{\Omega^2}{\Omega_{\text{eff}}^2} + \frac{\Omega^2}{\Omega_{\text{eff}}^2} \cos(\Omega_{\text{eff}} t). \quad (3.16)$$

On resonance, the oscillation frequency is minimal and the populations oscillate fully between $|1\rangle$ and $|2\rangle$. For $\Delta_0 \neq 0$, Ω_{eff} increases and the oscillation amplitude is reduced, such that state $|2\rangle$ is never fully reached. In our experiment, we use the hyperbolic form of Ω_{eff} as a function of Δ_0 to find the resonance condition $\Delta_0 = 0$.

3.3.2.2 Two-photon Rabi coupling with MW and RF fields

A direct transition between states $|1, -1\rangle$ and $|2, 1\rangle$ is not possible due to the selection rules. Therefore we couple the two states via a two-photon process with a MW photon and a RF photon, through an intermediate state $|0\rangle \equiv |2, 0\rangle$. We denote the energy difference between $|i\rangle$ and $|j\rangle$ by $\hbar\omega_{ij}$. The light frequencies of the MW and RF field are denoted by ω_{MW} and ω_{RF} respectively, the corresponding single photon Rabi frequencies are given by $\Omega_{\text{MW(RF)}} = \frac{1}{\hbar} \sqrt{\frac{1}{8}} \mu_B B_{\text{MW(RF)}}$. We assume there is no direct coupling between $|1\rangle$ and $|2\rangle$. The *intermediate detuning* Δ and the *two-photon detuning* δ are defined as (see Figure 3.10)

$$\begin{aligned} \Delta &= \omega_{\text{MW}} - \omega_{10}, \\ \delta &= \omega_{\text{MW}} + \omega_{\text{RF}} - \omega_{12}. \end{aligned}$$

On the experiment, we usually work at a large intermediate detuning $\Delta/2\pi = 500$ kHz so that both coupling fields are off-resonant ($|\Delta|^2 \gg \Omega_{\text{MW}}^2, \Omega_{\text{RF}}^2$) and $|0\rangle$ is not significantly populated. In addition, we choose the two-photon detuning to ensure two-photon resonance $|\delta| \ll |\Delta|$. Under this circumstance, only the two photon transition is resonant and any other transitions in the 8-level system are far off resonance, the system can thus be treated as a two-level system which is coupled by an effective two-photon Rabi frequency and effective detuning^[113]

$$\Omega_{\text{eff}} = \frac{\Omega_{\text{MW}}\Omega_{\text{RF}}}{2\Delta}, \quad (3.17)$$

$$\delta_{\text{eff}} = \delta + \frac{|\Omega_{\text{MW}}|^2 - |\Omega_{\text{RF}}|^2}{4\Delta}. \quad (3.18)$$

The effective detuning accounts for the AC Zeeman shift due to the MW and RF fields. Figure 3.11 shows the experimental results of the two-photon Rabi oscillation in case of $\delta_{\text{eff}} = 0$ and $\delta_{\text{eff}} \neq 0$. The effective Rabi frequency is much slower than the intermediate-detuning $|\Omega_{\text{eff}}| \ll |\Delta|$.

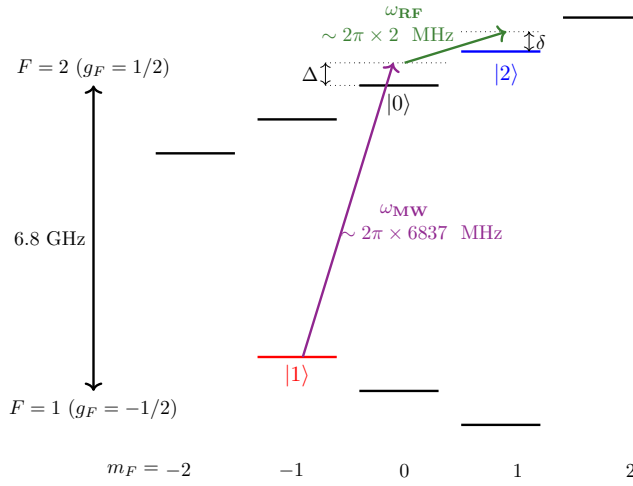


Figure 3.10 **Two photon Rabi transition.** The figure shows the MW and RF couplings with Rabi frequencies Ω_{MW} and Ω_{RF} , respectively, and the definitions of the intermediate-state detuning Δ and the two-photon detuning δ .

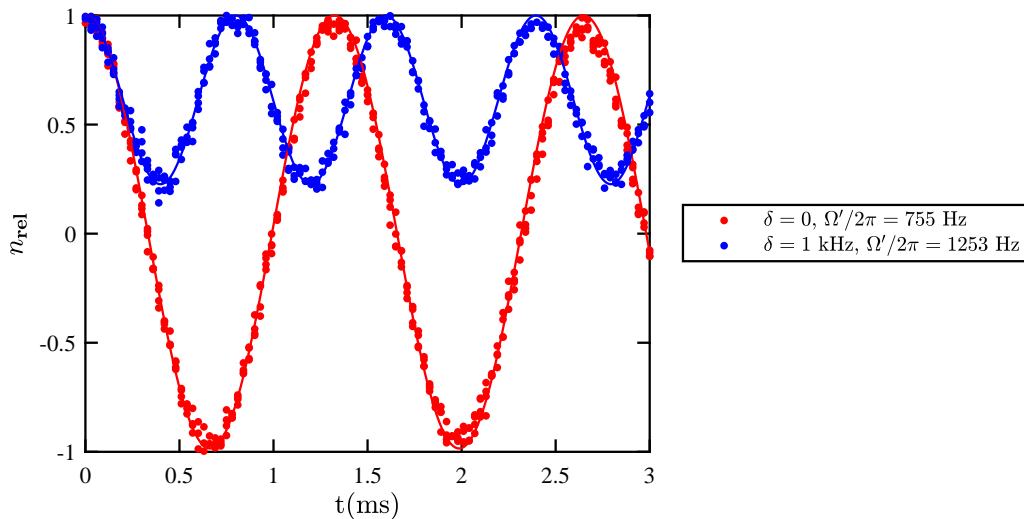


Figure 3.11 **Experimental result of two-photon Rabi oscillations,** with different two-photon detuning δ_{eff} . Solid lines show the fit to the data.

3.3.3 State-dependent potential

In our experiment, a state-dependent potential is created by sending microwave current to the on-chip co-planar waveguide wires, as illustrated in Reference [3]. The generated microwave magnetic near-field has a strong spatial gradient, which leads to a position dependence of the AC Zeeman shift $V_{\text{MW}}(\mathbf{r})$, with opposite signs for the states in manifold $|F = 1\rangle$ and $|F = 2\rangle$ according to Eq. 3.13, resulting in state-selective microwave potentials. In the near field, the effective microwave potential has an equivalent position dependence as the static potential since they are created by the same on-chip wires. The combination of the static and microwave potentials forms the state-dependent trapping potential, which is used to control the spatial mode of the two-component BEC. The overall potential for an atom in this case can be written as

$$U(\mathbf{r}) = V_Z(\mathbf{r}) + V_{\text{mw}}(\mathbf{r}), \quad (3.19)$$

where $V_Z(\mathbf{r})$ is the common potential generated by the static Zeeman shift, $V_{\text{mw}}(\mathbf{r})$ is the differential potential which arises from the AC Zeeman shift, given by

$$V_{\text{mw}}^{|1,-1\rangle}(\mathbf{r}) = +\frac{\hbar}{4} \sum_{m_2=-2}^0 \frac{|\Omega_{1,-1}^{2,m_2}(\mathbf{r})|^2}{\Delta_{1,-1}^{2,m_2}(\mathbf{r})}, \quad (3.20)$$

$$V_{\text{mw}}^{|2,1\rangle}(\mathbf{r}) = -\frac{\hbar}{4} \sum_{m_1=0}^1 \frac{|\Omega_{1,m_1}^{2,1}(\mathbf{r})|^2}{\Delta_{1,m_1}^{2,1}(\mathbf{r})}. \quad (3.21)$$

Here $\Delta_{1,m_1}^{2,m_2}(\mathbf{r})$ denotes the detuning with respect to the transition $|1, m_1\rangle \leftrightarrow |2, m_2\rangle$. Figure 3.12 illustrates the transitions that contribute to the AC Zeeman shift, in case of a general microwave field with all polarization components present. Note that there are three transitions contributing to the shift of state $|1\rangle$ but only two contributing to the state $|2\rangle$. In addition to the difference in sign, the AC Zeeman shifts for two states are also different in the gradient modulus. The latter difference depends on many factors, for example, the detuning of microwave, the strength of three polarization components of the field, the amplitude of the microwave field, *etc.*, all of which can be experimentally controlled to some extent. This provides the flexibility for engineering of the state-dependent potential.

Figure 3.13 shows the distribution of the MW field amplitude with an applied current $I_{\text{mw}} \approx 5$ mA and with blue-detuning $\Delta_0 = 12$ MHz with respect to the $|1, 0\rangle \leftrightarrow |2, 0\rangle$ transition^[19]. In the experiments described in chapter 5 aiming for spin squeezing, we explore different parameter configurations. For typically used parameters, and for mi-

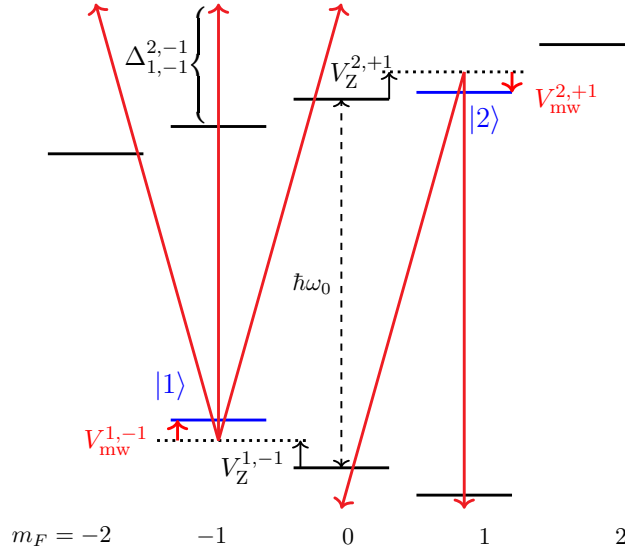


Figure 3.12 **Energy-level diagram of the hyperfine ground state in presence of external static and microwave fields.** This diagram shows the working principle of the state-dependent potentials, where $V_Z^{|F, m_F\rangle}$ represents Zeeman effects due to the static magnetic field and $V_{mw}^{|F, m_F\rangle}$ represents the AC Zeeman shifts due to the magnetic field of a blue-detuned microwave field. The AC Zeeman shifts are only shown for the states $|1\rangle$ and $|2\rangle$ used in our experiment, with opposite signs for $|1\rangle$ and $|2\rangle$. There are three microwave transitions contributing to the shift of $|1\rangle$ and two contributing to $|2\rangle$.

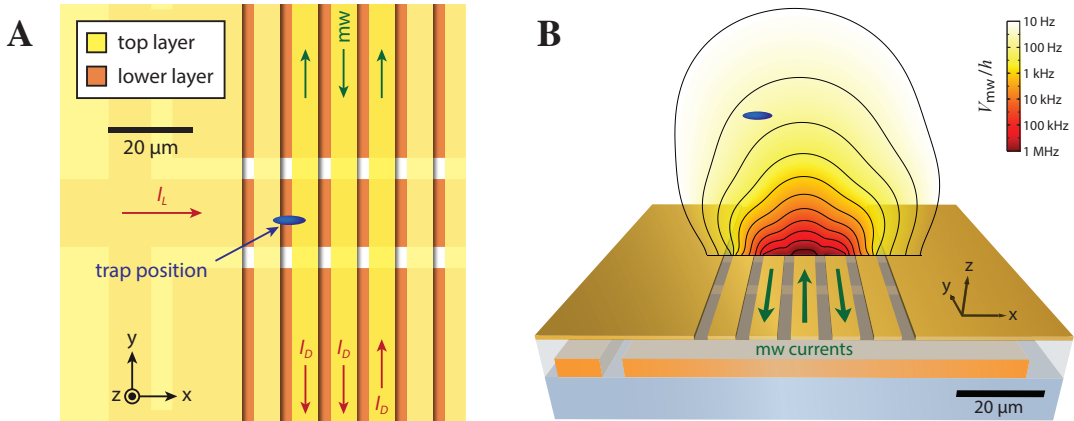


Figure 3.13 **Schematics of the chip wires around the trap position.** (A) A magnified top view of the central region of the five-wire structure. The arrows indicate the flows of the DC and MW currents used to create the static and state-dependent trapping potentials. (B) Angled view of the chip region shown in panel A. The microwave near-field potential V_{mw} for $I_{mw} \approx 5$ mA and $\Delta_{mw} = 2\pi 12$ MHz (blue detuning) is drawn for illustration. In both panels the position and shape (Thomas-Fermi radii) of the BEC is shown to scale in blue. The displacement in the trap bottom for the two internal states is too small to be visible at this scale. Figures adapted from Ref. [50].

crowaves blue-detuned by $\Delta_0 = 10$ MHz, a current of 30 mA will result in a separation of the trap minima for the two states of ≈ 400 nm, which is used to prepare a spin squeezed state, see section 5.3.

3.4 Precise detection of atom numbers

For the collective measurement of the multiple-spin system, a precise detection of atoms in both internal states is required. In our experiment, we take absorption images in order to extract the atom numbers. In this section I will present the imaging system, describe how it works, with emphasis on the calibration of the parameters of the absorption imaging.

3.4.1 Imaging systems

Two imaging systems are implemented in the apparatus. In the primary imaging system, a back-illuminated deep-depletion charge coupled device (CCD) camera ^① is aligned along $-y$ direction. The quantum efficiency of CCD camera at $\lambda = 780$ nm is $Q_e = 0.9$. This primary imaging system, with a magnification of 9.89, is mainly used in the end of the main experiment sequence to detect the atom numbers in the states $|F = 1, m_F = -1\rangle$ and $|F = 2, m_F = 1\rangle$, therefore need to be calibrated precisely (discussion see in the next subsections). In addition to the primary imaging system, there is a secondary imaging system with a CCD camera ^② aligned along the $-x$ -axis with a smaller magnification of 2.23. This system is not as well calibrated as the primary system, and is only used to observe the atoms in the stages of MOT, optical molasses and at the beginning of the magnetic trapping potentials. Detailed illustration of the imaging systems can be found in Ref. [50].

3.4.2 Absorption Imaging

We measure the atom numbers by measuring the atomic density in the time of flight (TOF) with absorption imaging. Absorption imaging requires at least two pictures, taken with and without atoms, respectively. In the first picture, a probe laser beam resonant with the imaging transition is shone onto the atoms, and the atoms absorb photons and cast a shadow onto the CCD camera. The other picture is taken with the same probe light in absence of the atomic cloud, as a reference picture. By comparing the two pictures, the

① Andor Ikon-M

② AVT Guppy F-044B NIR CCD

amount of light absorbed by the cloud can be extracted, known as optical depth OD. In our experiment, we take a third picture with probe light off and without atoms as a dark image, in order to eliminate the contribution of the background light illumination. The corresponding light intensities on the CCD camera in the three acquired images are denoted by I_a , I_{ref} , I_{dark} , respectively. Using those images, we calculate the light intensities with and without the absorption effect for each pixel (x, y) ,

$$I_f(x, y) = I_a(x, y) - I_{\text{dark}}(x, y),$$

$$I_i(x, y) = I_{\text{ref}}(x, y) - I_{\text{dark}}(x, y).$$

The spatial atomic density $n(x, y)$ of the cloud can be reconstructed pixel-by-pixel, based on the Beer-Lambert law^[114]:

$$n_{2D} = -\frac{1}{\sigma} \ln \left(\frac{I_f}{I_i} \right) + \frac{1}{\sigma} \frac{1}{I_{\text{sat}}^{\text{eff}}} (I_i - I_f), \quad (3.22)$$

where σ is the *effective absorption cross-section*, quantifying the probability of a photon being absorbed by an atom. It is defined as $\sigma = \beta\sigma_0$, where the resonant absorption cross-section is given by $\sigma_0 = 3\lambda^2/2\pi$ for wavelength $\lambda = 2\pi c/\omega_0$. The factor β is introduced to correct the effect caused by the presence of additional energy levels and errors in the probe polarization. It is an unknown parameter and needs to be calibrated experimentally. The second term on the right side contains *effective saturation intensity* $I_{\text{sat}}^{\text{eff}} = \alpha I_{\text{sat}}$ which accounts for the saturation of the imaging transition. In a two-level system, the saturation intensity of the transition is $I_{\text{sat}} = \hbar\Gamma\omega_0^3/12\pi c^2$ (for ^{87}Rb cycling transition, $I_{\text{sat}} = 1.67 \text{ mW/cm}^2$). In practice, the quantum efficiency of the CCD camera needs to be taken into account since the intensity of the light beam is derived from the electron number counted on the CCD pixels. Therefore the factor α is introduced to correct I_{sat} , which is unknown and needs to be determined by the experimental calibration.

3.4.3 Image acquisition and fringe removal

In our experiment, we care for the atom numbers in both internal states $|1\rangle \equiv |F = 1, m_F = -1\rangle$ and $|2\rangle \equiv |F = 2, m_F = 1\rangle$. Therefore, we take absorption images in the following steps. First, we illuminate the atomic cloud with a probe laser resonant to the cycling transition $F = 2 \rightarrow F' = 3$ transition, which will probe the atoms in $|2\rangle$ so that an image with the absorption effect of atoms in $|2\rangle$ is taken onto the CCD. After this process, atoms in state $|2\rangle$ are blown away by photon recoil force, leaving only atoms in state $|1\rangle$. We then optically pump all the remaining atoms to $F = 2$ so that an absorption image

of state $|1\rangle$ can be taken in the same manner as before. A reference image is then taken immediately after the two absorption images, in each run of the experiment. The acquired images are shown in Figure 3.14.

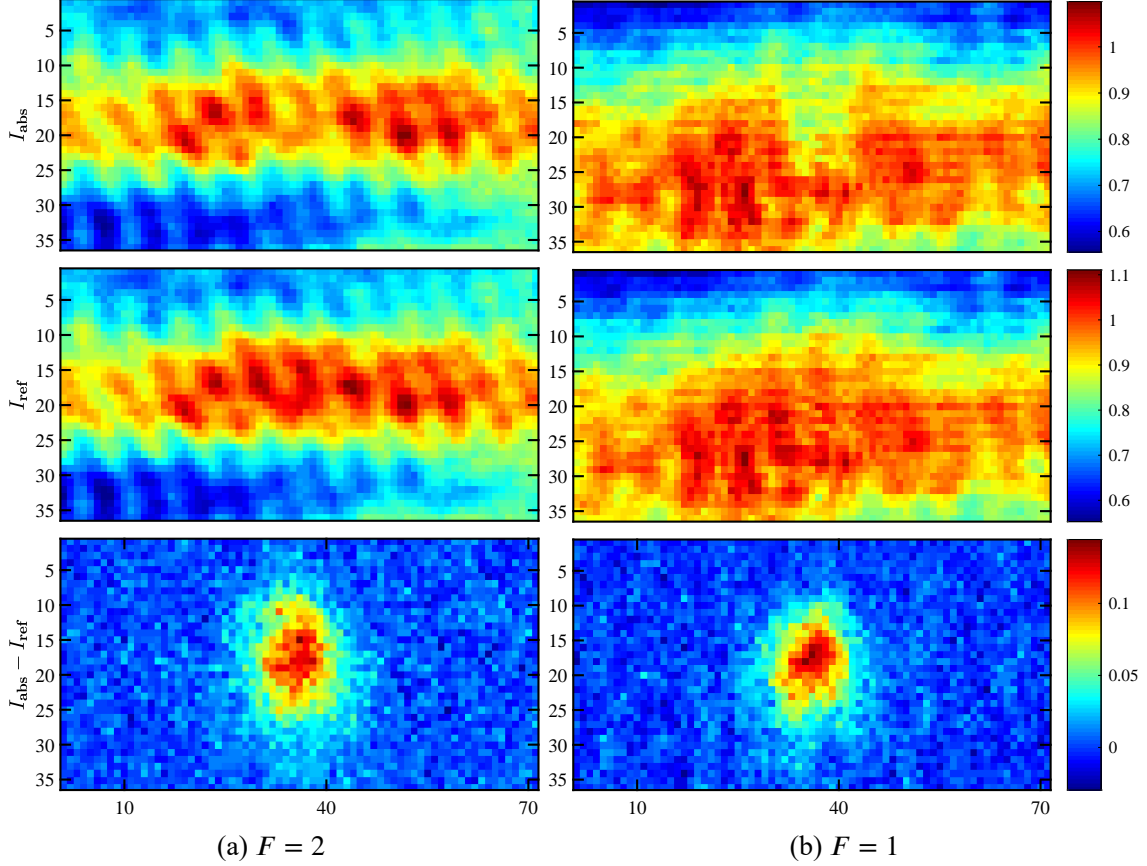


Figure 3.14 **Absorption images for the two internal states.** From top to bottom: the absorption images, the optimal reference images and the intensity difference between the absorption and optimal reference image.

On the absorption images, there exist unavoidable fringes caused by the interference of these optical components in the path of the imaging light, such as the glass windows, the wave plates, the surface of the PBS, *etc.* To minimize this effect, a straight-forward idea is to subtract the fringes using the reference image. However, the mechanical vibrations of these components (for example the vibration caused by the mechanical shutter in front of the CCD) result in a fluctuation of the fringes over time. It means that the fringes on the reference image are not identical to those on the absorption image and thus cannot be eliminated completely by simple subtraction. Moreover, photon shot noise results in shot-to-shot fluctuations even for identical probe light intensity. To reduce the imaging noise caused by these effects, we apply a so-called *fringe removal algorithm*, details can be found in Ref. [115-116]. Briefly summarize, the algorithm groups the acquired reference

images in blocks of 100 consecutive experimental runs. For each absorption image inside one block, an *optimal reference image* is generated by constructing a linear combinations of all reference images available in the whole block. In this way, the algorithm corrects for intensity fluctuations between the absorption image and the reference image, and in addition, reduces the photon shot noise by averaging images.

Figure 3.14 shows a typical absorption image and optimal reference image for each state, which are processed to reconstruct the two-dimensional density distributions of atoms in state $|1\rangle$ and $|2\rangle$. The integration of these densities within a chosen region gives the total atom number in each state, N_1 and N_2 . In most of the measurements presented in this thesis, we manually choose a rectangular region that contains all atoms to integrate the two-dimensional density and count the atom numbers. The regions used for state $|1\rangle$ is usually larger than that of state $|2\rangle$ because the atomic cloud have expanded further between detecting $F = 2$ and $F = 1$, and leads to a larger atom number noise in state $|1\rangle$.

For some of the experiments described in chapter 5, elliptical integration masks of the region are applied when counting the atom numbers to minimize the detection noise. We extract the position and size of the atomic cloud for each image from a 2D Gaussian fit, and use the mean position and mean size over the entire data set to define the integration region. We choose the radius of the integration region so that the region inside the mask contains more than 90% of the atomic distribution. In the measurement of section 5.3, the mask is particularly important, when the spin noise is extremely low due to the spin squeezing and the imaging noise contributes a considerable part of the total noise.

3.4.4 Calibration of the imaging system

For a specific imaging system, the parameters α (β) describing correction of the saturation intensity (absorption cross-section) are unknown and need to be calibrated in order to extract the correct atom number. From Eq. (3.22) we can calculate the corresponding density distributions for each internal state,

$$n_1 = \frac{1}{\beta_1} \left(\frac{1}{\sigma_0} \ln \left(\frac{I_f}{I_i} \right) + \frac{1}{\sigma_0 \alpha_1 I_{\text{sat}}} (I_i - I_f) \right), \quad (3.23)$$

$$n_2 = \frac{1}{\beta_2} \left(\frac{1}{\sigma_0} \ln \left(\frac{I_f}{I_i} \right) + \frac{1}{\sigma_0 \alpha_2 I_{\text{sat}}} (I_i - I_f) \right). \quad (3.24)$$

For each internal state $|i\rangle$, we have two independent parameters β_i and α_i , therefore there are in total 4 parameters $\beta_{1,2}$ and $\alpha_{1,2}$ to be determined. In order to calibrate these parameters, we adopt a series of measurements inspired by Ref. [114,117], as described in the

following.

First, we need to calibrate α_i to insure the detected atom numbers are independent of the light beam intensity^[114]. We scan the probe beam intensity (within a range of the relative saturation $s = I_i/I_{\text{sat}}^{\text{eff}}$ from 1 to 3). For each state $|i\rangle$, with a specific α_i and assumed parameter β_i (since these other unknown parameters do not affect the calibration of α_i , we set them at assumed values to make sure the atom number is reasonable), the measured atom number N_i is a function of the relative saturation s , as shown in Figure 3.15. We calculate the deviation of this set of atom number $\Delta N_i(s)$ and find the α_i that minimizes $\Delta N_i(s)$. We find $\alpha_1 = 1.32$ and $\alpha_2 = 1.49$, as shown in Figure 3.15.

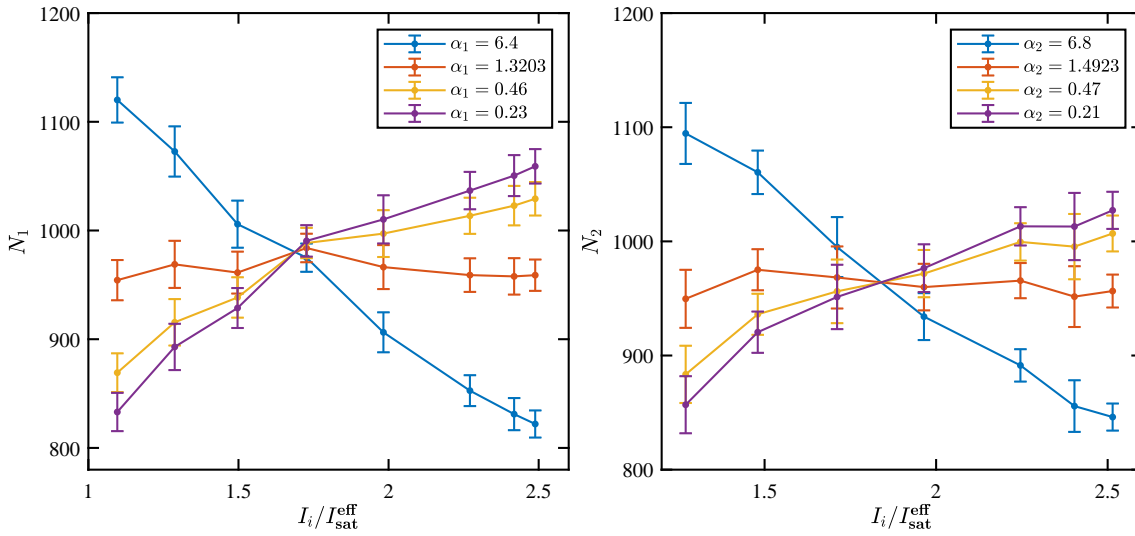


Figure 3.15 **Calibration of α to insure the measured atom number is independent of the beam intensity.** For each state, the atom number is calculated with several values of the unknown parameter α , while keeping the other unknown parameters at assumed values to make sure the atom number is reasonable. The plot represents atom numbers as a function of the incoming intensity. The standard deviation of each data set of ΔN has a minimum at the optimal α . The minimum of ΔN gives $\alpha_1 = 1.32$ and $\alpha_2 = 1.49$, as shown by the red data.

The second experiment aims to determine the ratio β_1/β_2 . This ratio is not necessarily 1 since it depends on the differential detectivity of the two states, which originates from the different atomic densities caused by the longer TOF of atoms in $|1\rangle$. The strategy for this calibration is to make sure that the detected atom number is independent of the relative population $n_{\text{rel}} = \frac{N_1 - N_2}{N}$. We prepare a BEC with all atoms in state $|1\rangle$ and perform a Rabi pulse with varying duration (usually from 0 to 2π pulse) to couple different fractions of atoms to state $|2\rangle$. We find the minimum of covariance $\text{Cov}(N, n_{\text{rel}})$ with the ratio $\beta_2/\beta_1 = 1.043$.

In the end, we determine the absolute values of β_i by measuring the scaling of the projection noise with the total atom number. We prepare BECs with different total atom

numbers $N = N_1 + N_2$ from 200 to 1200 by scanning the stop frequency of RF pulse during the evaporative cooling. The atoms are prepared in an equal superposition of two internal states $|1\rangle$ and $|2\rangle$. For this coherent state, the projection noise is given by

$$N^2 \text{Var}(n_{\text{rel}}) = N^2 \text{Var}\left(\frac{N_1 - N_2}{N}\right) = N^2 \frac{4}{N^2} \text{Var}(N_2) = N.$$

Therefore, the projection noise scales linearly with the total atom number N . In actual experiments the preparation of the coherent state is not perfect, therefore we make a correction $N^2 \text{Var}(n_{\text{rel}}) / \sqrt{1 - \langle n_{\text{rel}} \rangle^2}$ in order to account for the small miscalibration that makes $\langle n_{\text{rel}} \rangle \neq 0$. The linear scaling of the projection noise allows us to finally determine the absolute value of β_i . We fit a linear curve to the data and correct the slope to 1 by fixing β_1 (and therefore β_2 , since the ratio between the two has already been fixed by the second measurement), as shown in Figure 3.16. We obtain $\beta_1 = 1.1189$ and $\beta_2 = 1.0727$.

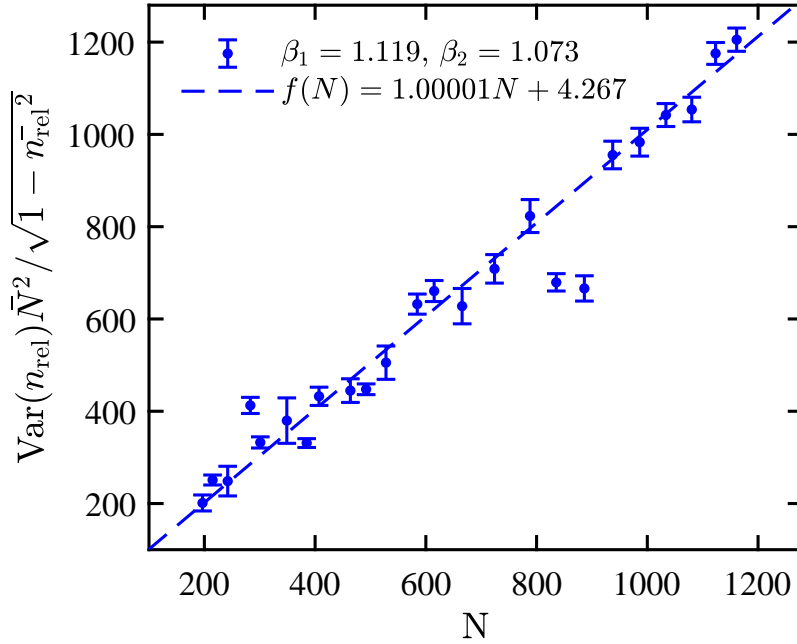


Figure 3.16 **Projection noise of a coherent state scales to the total atom number N .**

3.4.5 Detection Noise

The imaging system cannot detect atom numbers to any arbitrary precision due to the detection noises, which includes the effect of photon shot noise and other technical noise such as the electrical noise of the CCD camera, the noise caused by the optical fringes, *etc.* These noise are uncorrelated, thus add up quadratically

$$\sigma_{N_i, \text{det}}^2 = \sigma_{N_i, \text{SN}}^2 + \sigma_{N_i, \text{tech}}^2,$$

where i represent the internal state $|i\rangle$, $\sigma_{N_i,\text{SN}}$ is the atom number noise caused by the photon shot noise, and $\sigma_{N_i,\text{tech}}$ represents the contribution of other technical noise. The detection noise contributed by photon shot noise can be directly calculated from the imaging light intensities inside the integration region. We extrapolate for each pixel the photon number and count the total photon number inside the integration region N_{photon} . The expected photon shot noise is calculated as $\frac{1}{\sqrt{N_{\text{photon}}}}$ since the photons are uncorrelated, which is then converted into fluctuations of the number of atoms $\sigma_{N,\text{SN}}$. To characterize the total detection noise which also includes other technical noises, we choose a background integration region in the absorption images where no atoms are present, and calculate the shot-to-shot variance of atom number for that region. We observe that $\sigma_{N_i,\text{det}} \approx \sigma_{N_i,\text{SN}}$, which means that the effects of other technical noise are small and can be neglected, and the detection noise in our images is dominated by photon shot noise.

For our standard experimental trap results in noise levels of $\sigma_{N_1,\text{det}} = 4.1$ and $\sigma_{N_2,\text{det}} = 3.6$ atoms (standard deviations) in detecting atoms in $F = 1$ and $F = 2$, respectively. The detection noise in $F = 1$ is larger because the cloud has a longer TOF to expand, requiring a larger integration region. The detection noise corresponds to a noise level of $\sigma_{n_{\text{rel}},\text{det}} = (5.5 \pm 0.4) \times 10^{-3}$ in the relative atom number difference n_{rel} for typically used atom number $N \approx 1000$.

CHAPTER 4 LIMIT OF PHASE COHERENCE IN A TWO-COMPONENT BEC

Phase coherence is of primary importance to perform experiments in the quantum regime, because its finite duration poses stringent limitations on the possible practical applications, for example, the interrogation time of atom interferometer is fundamentally limited by the coherence time of the atomic ensemble. A better understanding of the intrinsic limits to the phase coherence in a BEC is not only relevant for quantum metrology with BECs, but also of fundamental interest^[7]. For these reasons, investigating the phase coherence property is of crucial interest.

In our experiment, we explore the phase coherence of the hyperfine ground states $|1\rangle \equiv |F = 1, m_F = -1\rangle$ and $|2\rangle \equiv |F = 2, m_F = +1\rangle$ in atomic BECs trapped in a magnetic trapping potential on an atom chip^[19,29,102]. With the state-of-the-art techniques in trapping and manipulating atoms, the BEC in magnetic traps is under excellent controllability, from the internal degree of freedom to the external ones. This system provides great opportunities to investigate the decoherence mechanism. Being a well isolated system, it provides a chance to concentrate on the decoherence mechanism intrinsic to a quantum many-body system, rather than on the interactions with the environment^[76,78]. In addition, a BEC has a life time of several seconds, which is a friendly time scale for non-equilibrium dynamics, for example the squeezing dynamics and the collisional effects.

In this chapter, we approach the question of coherence from two directions. Experimentally, the phase noise is monitored, and a ballistic spread of the relative phase is shown, *i.e.*, phase variance grows quadratically with time. Theoretically, we test our model by calculating numerically the phase spread during evolution by solving a master equation using the Monte Carlo wave-function method. The good agreement between the experiment and theoretical simulation confirms the validity of our model, showing decoherence is closely related to the interplay between the elastic collision interactions and the stochastic nature of the inelastic atom losses, which arises intrinsically in a many-body system.

This chapter starts by discussing the atom loss processes in a two-component system in section 4.1, which is important for understanding the decoherence mechanism, as

readers can see in later sections. Then we describe how to measure the phase fluctuations using Ramsey interferometry and to extract the phase noise by data processing. To understand the decoherence, the sources of phase noise are analyzed, from technical noise to the intrinsic noise. We build a theoretical model for relative phase dynamics of interacting and dynamically evolving BECs at zero temperature. The experiments and results presented in this chapter have been published, see Ref. [10].

4.1 Atom losses in a two-component BEC

The atomic losses play an important role in the evolution of the system. The dominant types of losses come from collisions between atoms of the BEC and the residual background gas (one-body losses) and the intrinsic two-body losses originate from inelastic two-body collisions inside BECs. As readers can see in the later sections, a basic understanding of the atom losses and the precise knowledge of loss rates are necessary for the understanding of the physics of intrinsic decoherence in a BEC. In this section I will introduce the atom losses, and how we characterize the loss constants with GPE simulations.

4.1.1 Atomic collisions

Depending on whether the atoms are lost after collision, there are two types of collisions, the elastic and inelastic collisions. The elastic collisions lead to unitary dynamics, such as the one-axis twisting Hamiltonian that allows for example to obtain spin squeezing, discussed in detail in chapter 5. The inelastic collisions introduce atom losses, leading to a limit of the BEC lifetime. Moreover, the collisions occur randomly, causing atom losses to be a stochastic process, which makes any phase fluctuation resulting from it impossible to correct for. This imposes a fundamental limit of the phase coherence in the system, as discussed in more detail in section 4.3.

There are several types of inelastic collisions in the ensemble, leading to one-, two- or three-body losses. One-body losses occur when atoms collide with the background gas atoms and get lost from the trap. Due to the finite vacuum, this loss channel is always present. Two-body losses result from inelastic collisions between two particles of the ensemble, which can happen by two different mechanisms: the spin-exchange collision and the spin-dipole collision. For ^{87}Rb atoms, the extremely weak spin-dipole collision contributes negligibly, and spin-exchange collisions dominate in the losses. During a spin-

exchange collision, atoms of the colliding pair exchange their orientation of individual spin, while preserving total angular momentum. For example, in a BEC of ^{87}Rb , if two atoms of $m_F = 1$ collide with each other, a spin-exchange collision conserves the m_F :

$$|2, 1\rangle + |2, 1\rangle \rightarrow |2, 2\rangle + |2, 0\rangle.$$

This process can occur between atoms in the same internal state and is called *intra-species collision*. After collision, the new pair contains an atom in the state $|F = 2, m_F = 0\rangle$, which is untrappable in our magnetic trapping potential and get lost from the BEC. For a pair of atoms both in state $|F = 1, m_F = -1\rangle$, the conservation of the angular momentum prohibits them from the spin-exchange collisions. In a two-component BEC, collisions can also occur between atoms in different internal states, *i.e.*, *the inter-species collision*

$$|1, -1\rangle + |2, 1\rangle \rightarrow |1, 0\rangle + |2, 0\rangle,$$

with both involved atoms ending up in untrappable states and being lost from the ensemble.

Inelastic collisions among three atoms result in three-body losses. Unlike the two-body inelastic collisions, in three-body collisions the presence of a third particle allows for the formation of molecules. The energy released when two particles form a bound state is converted into kinetic energy of both the molecule and the third particle, and both escape from the trapping potential. For ^{87}Rb atoms, this process occurs in both state $F = 1$ and $F = 2$, resulting in particle losses.

4.1.2 Density-dependent losses

All the collision processes described above depend on the atomic density of the BEC. In particular, losses caused by the inter-species collisions depend on the atomic densities of both states, thus couple atom numbers in two states together. By considering the one, two, and three-body losses, the atom number in each state can be described by the following coupled rate equations

$$\frac{dN_1}{dt} = -k^{(1)}N_1 - k_{11}^{(2)}N_1^2 - k_{12}^{(2)}N_1N_2 - k_{111}^{(3)}N_1^3, \quad (4.1a)$$

$$\frac{dN_2}{dt} = -k^{(1)}N_2 - k_{11}^{(2)}N_2^2 - k_{12}^{(2)}N_1N_2 - k_{222}^{(3)}N_2^3, \quad (4.1b)$$

where N_1 and N_2 represent the atom numbers in state $|1\rangle$ and $|2\rangle$, respectively, and $k^{(m)}$ represents the m -body loss rate. The one-body loss depends strongly on the vacuum pressure, thus $k^{(1)}$ differs from experiment to experiment. Two-body and three-body losses

depend on the density of the ensemble. They together lead to a decay of atom number over time.

Taking the atom losses into consideration, the spatial dynamics of the BEC is different compared to the scenario discussed in section 2.2. In the 2CGPE introduced there, the atom number is conserved, *i.e.*, $N(t) = N$, which is no longer true for long times when atom losses cannot be neglected. To take the losses into account, complex terms must be included on the right hand side of Eqs. (2.17) and (2.18), in order to obtain a decay of $N(t)$. The 2CGPE including losses are thus given by

$$i\hbar \frac{\partial \phi_1}{\partial t} = [T + V + g_{11}N_1|\phi_1|^2 + g_{12}N_2|\phi_2|^2 - i\Gamma_1]\phi_1, \quad (4.2a)$$

$$i\hbar \frac{\partial \phi_2}{\partial t} = [T + V + g_{22}N_2|\phi_2|^2 + g_{12}N_1|\phi_1|^2 - i\Gamma_2]\phi_2, \quad (4.2b)$$

where $T = -\frac{\hbar^2 \nabla^2}{2m}$ is the kinetic energy, V is the trapping potential and g_{12} , g_{11} and g_{22} are the interaction coupling constants. The imaginary part describes the atom loss due to collisions,

$$\Gamma_1 = \hbar/2(K^{(1)} + K_{12}^{(2)}|\phi_2|^2 + K_{111}^{(3)}|\phi_1|^3),$$

$$\Gamma_2 = \hbar/2(K^{(1)} + K_{12}^{(2)}|\phi_1|^2 + K_{22}^{(2)}|\phi_2|^2 + K_{222}^{(3)}|\phi_2|^3),$$

where $K^{(1)}$ is the one-body loss coefficient, $K_{12}^{(2)}$, $K_{22}^{(2)}$ are interspecies two-body loss coefficient and intraspecies two-body loss coefficient respectively, and $K_{111}^{(3)}$, $K_{222}^{(3)}$ are three-body loss coefficients for atoms in state $|1\rangle$ and $|2\rangle$ respectively.

Comparing the Eq. 4.1 and Eq. 4.2, one can easily find that for two/three-body losses, the loss rate $k^{(2)}$ ($k^{(3)}$) depends on both the atom density in the ensemble and loss coefficients $K^{(m)}$.

$$k^{(m)} = K^{(m)} \int \eta(\mathbf{r})^m d\mathbf{r},$$

where $K^{(m)}$ is the loss constant for m -body losses, $\eta(\mathbf{r})$ is the normalized atomic density of the ensemble with $\int \eta(\mathbf{r}) d\mathbf{r} = 1$. Note that the *loss rate* and *loss constant* should be distinguished. The loss rate $k^{(m)}$ is a product of the loss coefficient and the atomic density, while each loss coefficient $K^{(m)}$ is a constant, dependent on the atomic species and the internal states. Only for one-body loss, the loss rate equals to the loss constant, $k^{(1)} = K^{(1)}$.

For the three-body losses, the loss coefficients are very small, with $K_{111}^{(3)} = 5.8 \times 10^{-42} m^6/s^{[118]}$ and $K_{222}^{(3)} = 18(6) \times 10^{-42} m^6/s^{[119]}$. For experiments with very large densities $N > 10^5$, three-body losses still dominate. However in our case the atomic

density is small (with only approximately 1000 atoms), the three-body losses can be neglected. We confirm with GPE simulations that three-body losses have no significant effect on the atom number decay. In the remainder of this thesis we will only consider the one- and two-body losses.

Note that, in our experiment, the thermal fraction in the system can be neglected and the BEC can be well described by a zero-temperature condensate.

4.1.3 Atom loss coefficient measurement

The precise knowledge of the values of these loss coefficients is required to simulate the accurate phase evolution (the relative phase between two states jumps every time when an atom is lost from the condensate, detailed discussion in section 4.4). In the literature, there are already measurements of these coefficients^[44,80], but given the good precision of our experiments we repeat these measurements. In order to decouple the equations and measure the loss coefficients independently, we perform the following series of experiments.

In the first experiment, in order to measure the one-body loss constant we prepare all the atoms in state $|1\rangle$. In this case the loss of atoms happen solely due to one-body losses, happening with the rate $k^{(1)} = K^{(1)}$. We can extract $K^{(1)}$ by fitting the experimentally measured atom number with a simple exponential decay $N_1(t) = N_1(0)e^{-k^{(1)}t}$, shown in Figure 4.1.

The remaining two-body loss constants $K_{22}^{(2)}$ and $K_{12}^{(2)}$ will be determined by comparing the experimental data with GPE simulations in two scenarios. In the second measurement, we prepare a BEC with atoms purely in state $|2\rangle$ (Figure 4.1(b)). In this case, there are two loss channels present: the one-body losses and intra-species two-body losses. Since $K^{(1)}$ has already been determined, there is only one free coefficient to find, the rate of two-body losses $K_{22}^{(2)}$. We simulate the number of atoms N_2 versus time using the GPE for component $|2\rangle$ Eq. (4.1) including losses represented by $K_{22}^{(2)}$ to the best fit to the experimental values in order to extract $K_{22}^{(2)}$. The idea is to use the loss constant as an input of the GPE simulation and compare the simulated decay of atom number with the experimental data. If there is any discrepancy between the simulation and experimental data, one should manually change the input constant by a small step and repeat the simulation again, until the simulated result matches the measured data. For a properly chosen starting point of the input parameter, it only takes a few iterations to find the best match.

In the third experiment, we prepare the BEC in an equal superposition of $|1\rangle$ and $|2\rangle$,

and measure the atom decay in both spin states (Figure 4.1(c)). Now all loss channels are present, but only one unknown loss constant $K_{12}^{(2)}$ remains, which we determine by comparing the 2CGPE simulation (4.2) with the data in a similar way.

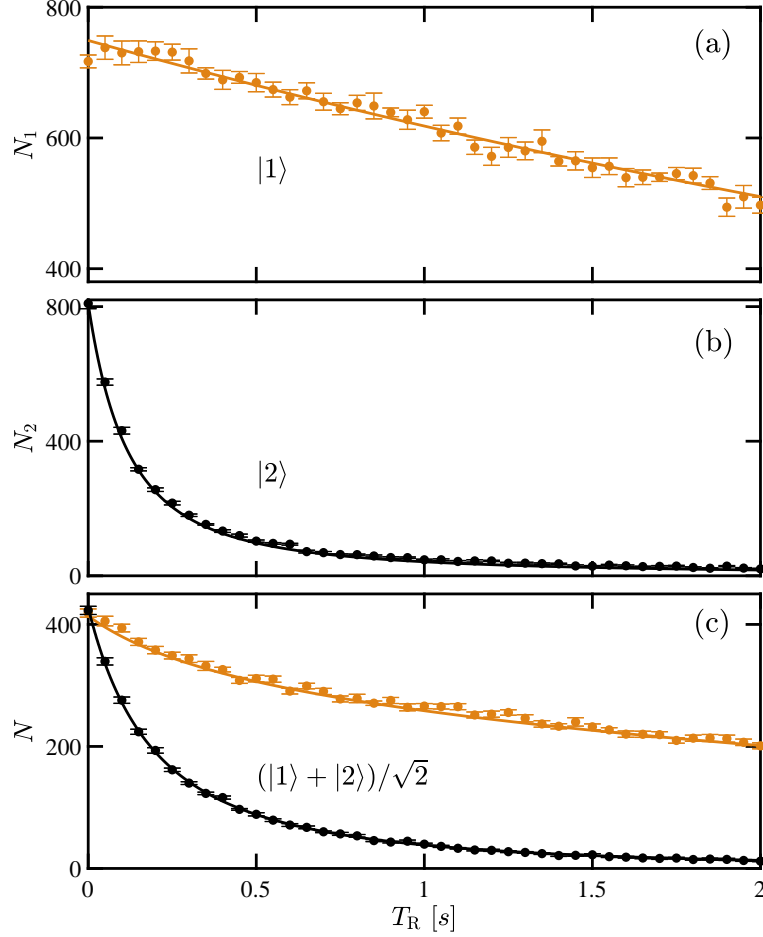


Figure 4.1 **Time evolution of the mean atom number for three different initial states:** all atoms initially in state $|1\rangle$ (top), in state $|2\rangle$ (middle) and in the superposition $(|1\rangle + |2\rangle)/\sqrt{2}$ (bottom). Orange (Black) points show the measured atom number in spin state $|1\rangle$ ($|2\rangle$). Error bars represent one standard error of the mean. Solid lines are from corresponding GPE simulations with loss rate constants $K^{(1)} = 0.17 \text{ s}^{-1}$, $K_{22}^{(2)} = 10.3 \times 10^{-14} \text{ cm}^3 \text{ s}^{-1}$ and $K_{12}^{(2)} = 2.0 \times 10^{-14} \text{ cm}^3 \text{ s}^{-1}$. The measurements shown in this figure are performed in a trap with trapping frequencies $\omega_{(x,y,z)} = 2\pi \times (714, 714, 114) \text{ Hz}$.

Since the extraction of $K_{22}^{(2)}$ and $K_{12}^{(2)}$ needs a few iterations of the above procedures, and solving time-dependent GPE including losses up until $t = 2 \text{ s}$ is rather time expensive, it is important to start with a reasonable guess of the loss coefficients. In order to have a rough estimate of the range of values for $K_{22}^{(2)}$ and $K_{12}^{(2)}$, we first fit the measured atom number decay initially in the superposition $(|1\rangle + |2\rangle)/\sqrt{2}$ with the coupled rate equation Eq. (4.1). The fitted results are shown in Figure 4.2. With the fitted parameters $k_{12}^{(2)}$ and $k_{22}^{(2)}$, and an atomic density $\int \eta(\mathbf{r})^m d\mathbf{r}$ estimated from a ground state solution of the GPE,

we obtain a set of $K_{22}^{(2)}$ and $K_{12}^{(2)}$ as the starting point of the GPE iterations.

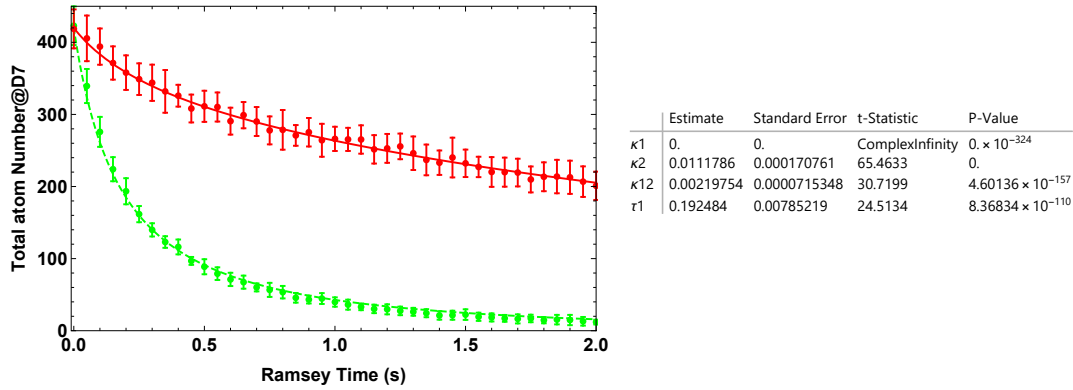


Figure 4.2 **Time evolution of the mean atom numbers** (Red: $\langle N_1 \rangle$; Green: $\langle N_2 \rangle$) for atoms initially in the superposition $(|1\rangle + |2\rangle)/\sqrt{2}$. Each data point is a mean of 10 measurement repetitions and the errorbar shows the standard deviation. The solid curve shows a fit with the coupled rate equation Eq. (4.1). The result can be used to estimate the starting point of the 2CGPE simulation iteration.

To further confirm the result, the above series of measurements and procedures are performed in both a tight and a relaxed trapping potential, with trapping frequencies $\omega_{(x,y,z)} = 2\pi \times (114, 714, 714)$ Hz and $\omega_{(x,y,z)} = 2\pi \times (113, 301, 301)$ Hz, respectively. The measured loss constants show consistency with each other. To compare with the previous knowledge of the loss constants, we summarize the previously measured loss constants, see Table 4.1. The loss rate constants determined in our experiment are $K_{22}^{(2)} = 10.3(3) \times 10^{-14} \text{ cm}^3 \text{ s}^{-1}$ and $K_{12}^{(2)} = 2.0(1) \times 10^{-14} \text{ cm}^3 \text{ s}^{-1}$. Our values differ from previously reported values in Ref. [44] but agree with the ones from Ref. [120-121].

Table 4.1 Loss constants

reference	$K_{12}^{(2)}$ (m ³ /s)	$K_{22}^{(2)}$ (m ³ /s)
Kempen ^[120]	1.9×10^{-20}	
Mertes ^[45]	$7.80(19) \times 10^{-20}$	$11.94(19) \times 10^{-20}$
Egorov2013 ^[44]	$1.51(18) \times 10^{-20}$	$8.1(3) \times 10^{-20}$
Tojo ^[121]		$10.4(10) \times 10^{-20}$
Our work	$2.0(1) \times 10^{-20}$	$10.3(3) \times 10^{-20}$

4.2 Measurement of the phase noise

In our experiment, the phase coherence can be characterized by the spreading of the relative phase between the two components. The relative phase can be easily observed from interference measurements with the following Ramsey sequence. The initial atomic ensemble is a pure BEC of 1000 atoms in state $|1\rangle$. We use a standard magnetic trap, with trap frequencies $\omega_{(x,y,z)} = 2\pi \times (114, 714, 714)$ Hz. To initialize the Ramsey experiment, we apply a two-photon Rabi pulse with a duration corresponding to $\pi/2$ rotation. This creates a two-component BEC in which all atoms are in a coherent superposition of state $|1\rangle$ and $|2\rangle$. Without splitting the two components, we let the system evolve for a given Ramsey time T_R . Afterwards, a second Rabi pulse of area $\pi/2$ is applied to convert the accumulated phase to atom number difference, and we measure the relative atom number as $n_{\text{rel}} = \frac{N_1 - N_2}{N_1 + N_2}$. By scanning the relative phase ϕ_R between the two Rabi pulses, the recorded n_{rel} result in the Ramsey fringe (in phase domain).

By repeating this experimental sequence substantially, one has access to the distribution of the relative phase after an evolution time T_R . By varying the interrogation time, we investigate the phase spread as a function of T_R , see Figure 4.3. One should keep in mind that the phase under investigation is the relative phase between the two components (or the two internal states). For the interferometers in practical application, this relative phase usually carries the information of the physical quantity of interest and any phase spreading will reduce the precision of the measurement. Therefore, the phase decoherence investigated in this chapter sets a limit to the precision of interferometric measurements.

4.2.1 Visibility and contrast

We define two quantities associated to the recorded interference fringes: visibility and contrast. We call visibility, \mathcal{V} , one half of the width of the vertical band containing the interference measurements. We call contrast, \mathcal{C} , the amplitude of the curve $\mathcal{O} + \mathcal{C} \sin(\phi_R - \phi_0)$ fitting the interference measurements.

4.2.1.1 Visibility

The outcome of a single shot of a Ramsey experiment can be described by the following heuristic model

$$n_{\text{rel}}(\phi_R) = \mathcal{V} \sin(\phi_R + \phi), \quad (4.3)$$

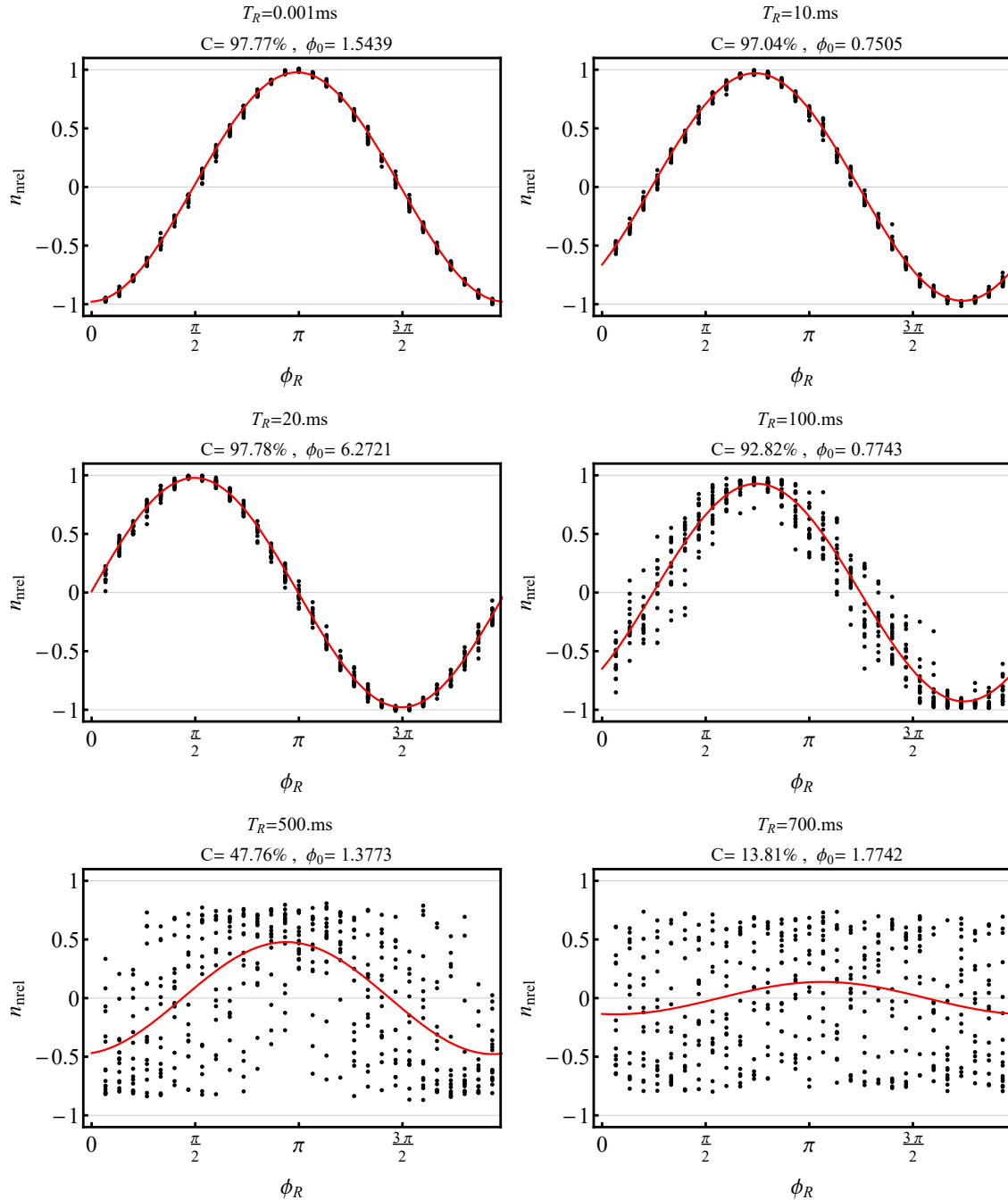


Figure 4.3 **Ramsey interferometer fringes at different T_R** , where each black dot corresponds to one experimental run and the red curve shows a sinusoidal fit of the experimental data to extract the contrast C and the zero-crossing phase ϕ_0 (see text). The fringe at 10 ms shows almost no sign of phase noise while after 100 ms the fringe is smeared out by phase noise and the contrast is reduced.

where \mathcal{V} is the fringe visibility, and ϕ is a classical random variable describing the phase accumulated by the state during the interrogation time T_R , which fluctuates shot to shot due to noise. The phase noise quantified by the standard deviation $\Delta\phi$ is evaluated in the section 4.2.2. The visibility describes the length of the projection of the mean spin on the xy -plane on the generalized Bloch sphere, normalized to the expectation value of the mean spin length

$$\mathcal{V} = \frac{\sqrt{\langle \hat{S}_x \rangle^2 + \langle \hat{S}_y \rangle^2}}{\langle S \rangle}.$$

Note that here \hat{S}_x and \hat{S}_y refer to the collective spin component related to the state after the evolution of a duration T_R , but before the second Rabi pulse.

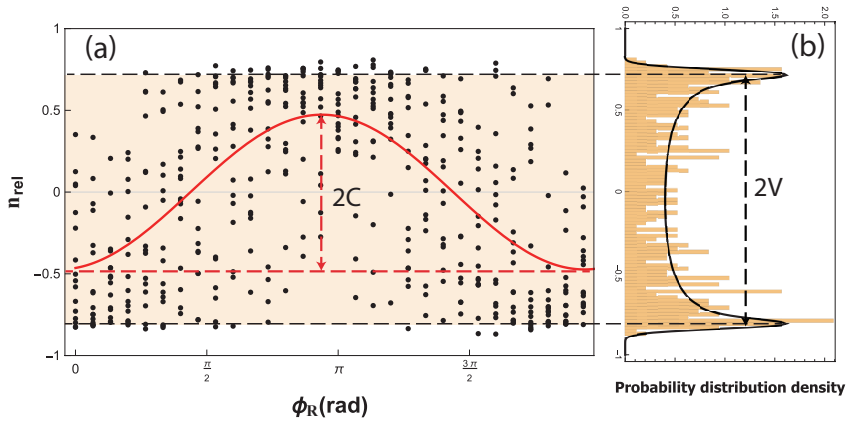


Figure 4.4 **Ramsey Fringe at $T_R = 500$ ms.** (a) Ramsey fringe, where each black dot corresponds to one experimental run. The red curve is a fitted sine function used to extract the contrast C . (b) Histogram of the normalized atom number imbalance. The fit to extract the visibility is performed with a method described in Ref. [122].

The visibility is extracted for each T_R , by fitting the distribution of n_{rel} with a so-called ‘‘BAT’’ method^[122], see Figure 4.4. The visibility can be understood as the normalized spin length, which is the maximum value the Ramsey contrast can achieve in an ideal case in absence of the phase noise. As one can see in Figure 4.4, the visibility determined by the BAT method is actually smaller than the largest n_{rel} the data can reach due to the spin variance. The small wings at the edge of the BAT distribution reflect the projection noise.

The natural ‘breathing’ dynamics between the two components (discussed before in section 2.2.2) is expected to modulate the maximum value that n_{rel} can reach, *i.e.*, the visibility. Meanwhile, the atom losses in the two states are asymmetric, more precisely, the atoms in state $|2\rangle$ are lost much faster than those in $|1\rangle$, which also reduces the visibility to less than 1. The latter effect can be understood by thinking of an optical interferometer,

where the largest contrast is always achieved when the two beam intensities are balanced. Similarly in our system, the asymmetric atom number in the two modes will limit the largest $|n_{\text{rel}}|$. Although the visibility of the fringe (peak-to-peak amplitude) is expected to be reduced by the two effects mentioned above, the reduction of visibility does not imply that the phase coherence in the BEC is lost. Both processes are coherent and in principle do not change the phase distribution. In fact, in presence of decoherence, the quantity which is changed is the ‘contrast’.

4.2.1.2 Contrast

We fit the phase-domain Ramsey fringes to extract contrast with a model

$$n_{\text{rel}}(\phi_{\text{R}}) = \mathcal{O} + C \sin(\phi_{\text{R}} - \phi_0) ,$$

with three free parameters: Ramsey contrast C , the fitted phase at zero-crossing slope ϕ_0 and the offset \mathcal{O} .

One should keep in mind that, while a reduction in the visibility directly causes a reduction in the amplitude of the fitted contrast, a reduction of the contrast can occur in presence of phase noise, even if the visibility is 1. The physical meaning behind the difference between contrast and visibility can be understood from a collective spin point of view. Here we denote the projection of the collective spin vector in the equatorial plane as S_α , and denote the quadrature which is along the equator and perpendicular to α as S_\perp . Again, here \hat{S} refers to the collective spin vector before the second Rabi rotation. When describing a single shot of the interferometric measurement, one typically considers the expectation value $\langle S_\alpha \rangle$, which can be described by $\mathcal{V} = \frac{\langle S_\alpha \rangle}{\langle S \rangle}$, where $\langle S_\alpha \rangle = \sqrt{\langle S_x \rangle^2 + \langle S_y \rangle^2}$. However, the important information about phase noise is contained in the shot-to-shot fluctuations of S_\perp . We denote the fluctuation of the spin along this quadrature as ΔS_\perp . The phase noise is defined as:

$$\Delta\phi = \frac{\Delta S_\perp}{\langle S_\alpha \rangle} = \frac{\Delta S_\perp}{\mathcal{V}\langle S \rangle} . \quad (4.4)$$

where ϕ is the relative phase under investigation and $\Delta\phi$ is the standard deviation of the phase distribution. In the ideal case of a coherent spin state on the equator, the phase uncertainty is only due to the projection noise, and the contrast of a Ramsey fringe is the same as the visibility. In the realistic case, the phase fluctuations due to other sources of noises will smear out the contrast. By assuming a Gaussian distribution of the phase

fluctuations, the interference contrast is in fact^[76]

$$C = \mathcal{V}e^{-\frac{1}{2}\Delta\phi^2}. \quad (4.5)$$

It is interesting to compare the evolutions of the visibility and the contrast. In Figure 4.5, the decay of both quantities is shown. The black dashed line shows the expected maximum value of the visibility, $\mathcal{V}_{\max} = \frac{2\sqrt{N_1 N_2}}{N_1 + N_2}$, which is lower than 1 due to the asymmetric atom losses in the two internal states. The small gap between the extracted visibility and the dashed line can be attributed to the spatial demixing between the wave functions of the two components. The contrasts are extracted from the raw data and the post-processed data after the clock-shift correction, see section 4.3.1.2. The gap between the extracted visibility and contrast helps one to visualize the decoherence process.

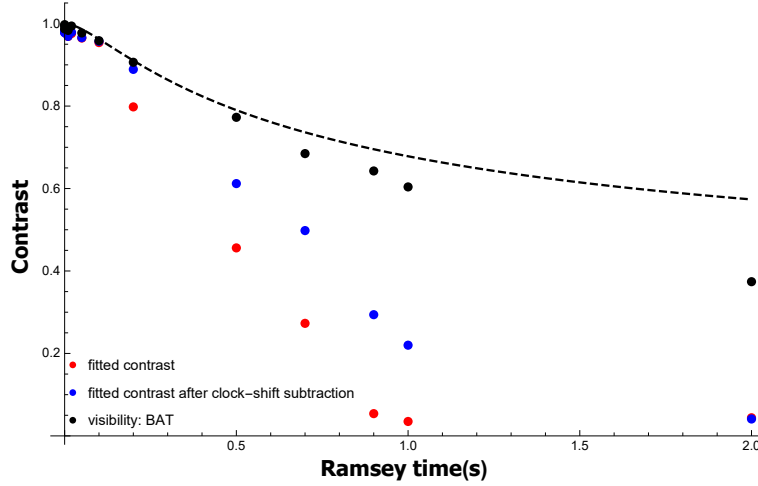


Figure 4.5 **The extracted visibility and contrast.** Each point corresponds to a Ramsey fringe with a particular interrogation time T_R containing more than 200 shots. The dashed line shows $\mathcal{V} = \frac{\sqrt{N_1 N_2}}{N_1 + N_2}$, corresponding to the visibility reduction solely due to the atom losses.

4.2.2 Calculation of phase noise

It is not a trivial task to evaluate the phase noise, especially for long Ramsey time when the noise is so large that the contrast is nearly smeared out and the state starts wrapping around the Bloch sphere. I will describe how we evaluate the phase fluctuations quantitatively for Ramsey time up to 1 s.

4.2.2.1 For $T_R < 0.2$ s

For short Ramsey times $T_R < 0.2$ s, when the phase noise is so small that the contrast $C(t) \approx \mathcal{V}(t) \approx 1$, it is better to measure $\Delta\phi$ directly on the slope of a Ramsey fringe. To do this, we always have two sequences: one is a full Ramsey phase scan and the other is the

noise measurement at the zero-crossing slope. We first record the full fringe in order to determine a zero-crossing phase ϕ_0 , *i.e.*, the point at which the mean of number imbalance n_{rel} is zero ($\langle n_{\text{rel}} \rangle = 0$) and the slope of the fringe reaches its maximum $\partial n_{\text{rel}}/\partial\phi = \mathcal{V}$. We then can experimentally set the Ramsey phase to the value $\phi_R = \phi_0$ and repeat the Ramsey sequence hundreds of times to gather statistics at the zero-crossing point. The measured phase is evaluated as $\phi = \arcsin(n_{\text{rel}}/\mathcal{V})$ for each shot and we collect the phase distribution. From the experimental results, it is shown that the phase has a Gaussian distribution, allowing one to evaluate the phase noise in terms of the standard deviation $\Delta\phi$. The alternative way is to first calculate the standard deviation of n_{rel} and then compute $\Delta\phi$ with error propagation $\Delta\phi = \frac{\partial\phi}{\partial n_{\text{rel}}} \Delta n_{\text{rel}} = \frac{\Delta n_{\text{rel}}}{\mathcal{V}}$, which is consistent with the previously defined phase noise $\Delta\phi = \frac{\Delta S_{\perp}}{\langle S_{\alpha} \rangle}$. Both methods are based on gathered statistics at the middle of the fringe slope and are equivalent to each other.

In practice, due to the imperfect calibration of the phase ϕ_0 , the measured data sometimes show a mean of the n_{rel} deviated from 0, and this shift should be taken care of when calculating. We correct for this effect by making a modification to the slope $\partial n_{\text{rel}}/\partial\phi = \mathcal{V}\sqrt{1 - \langle n_{\text{rel}} \rangle^2}$.

4.2.2.2 For $T_R > 0.2$ s

For long Ramsey times $T_R > 0.2$ s, the phase spread can be larger than 2π , which will render the conversion from n_{rel} to phase ϕ meaningless, since it can cause ambiguities of the phase. For example, a phase $\phi = \phi_0$ and $\phi = \phi_0 + \pi$ will both lead to $n_{\text{rel}} = 0$ and the two phases cannot be distinguished by n_{rel} .

For a more appropriate evaluation, we collect statistics over the whole Ramsey fringe, with a varying ϕ_R from 0 to 2π . From these data, the contrast C and visibility \mathcal{V} can be extracted. As mentioned before, a reduction of the contrast can be either due to the reduction of the visibility, or due to the phase decoherence happening in the system. To disentangle the effects due to decoherence and from the others, we consider the contrast normalized with respect to the visibility, C/\mathcal{V} , which depends only on phase noise. From the definition Eq. (4.5) we can then extract the phase noise from the normalized contrast by

$$\Delta\phi = \sqrt{-2 \ln (C/\mathcal{V})}.$$

The phase noise, as the quantity of our interest, results from the sum of different contributions (*e.g.*, atom number fluctuations, atom losses, finite temperature, technical

noise). There have been works in the literature, based on quantum-optics inspired approaches, predicting that the phase of a condensate in thermal equilibrium will undergo diffusion causing the phase variance to grow linearly in time. A different conclusion is reached in our work. We observe that phase uncertainty $\Delta\phi$ grows linearly with time, as shown in Figure 4.12), which hints at a ballistic spread of phase. We tackle this problem by investigating the origins of different types of noise.

4.3 Noise analysis

Theoretical studies make different predictions for the decoherence mechanisms, and there are many different types of noise sources, whose contribution to the phase fluctuations depends on the system. These noise sources, in general, fall into two categories: the technical noise, coming from the imperfect control of the experiment or perturbations in the environment, and the intrinsic noise arising from the interactions in the many-body system. Intrinsic as well as technical noises are expected to reduce the contrast of the Ramsey fringes. In this section we will analyze the sources of phase noise present in our system one by one.

4.3.1 Intrinsic noise

One advantage of the two-component BEC is that being a well isolated system, providing an opportunity to study the intrinsic noise. In a BEC, the atoms interact with each other through collisions and cause interaction-induced noise, which is intrinsic to the system itself. The spin dynamics of the collective spin due to elastic collisions between atoms can be described by the collective spin Hamiltonian Eq. (2.27). By dropping the offset terms the full Hamiltonian can be simplified to

$$\hat{H} = \hbar\tilde{\chi}\hat{N}\hat{S}_z + \hbar\chi\hat{S}_z^2, \quad (4.6)$$

where $\hat{S}_z = (\hat{N}_1 - \hat{N}_2)/2$ is the z component of the collective spin operator, and $\hat{N} = \hat{N}_1 + \hat{N}_2$ is the total atom number. The parameters

$$\tilde{\chi} = \frac{1}{2\hbar} \left(\frac{\partial^2 E}{\partial N_1^2} - \frac{\partial^2 E}{\partial N_2^2} \right), \quad (4.7)$$

$$\chi = \frac{1}{2\hbar} \left(\frac{\partial^2 E}{\partial N_1^2} + \frac{\partial^2 E}{\partial N_2^2} - 2 \frac{\partial^2 E}{\partial N_2 \partial N_1} \right). \quad (4.8)$$

depend on the energy E of the two interacting components with mean atom number $\langle N \rangle_1$ and $\langle N \rangle_2$ in state $|1\rangle$ and $|2\rangle$, respectively^[49]. Both terms in the Hamiltonian will lead to a spread of the phase.

4.3.1.1 Phase diffusion

Phase diffusion is a typical intrinsic source of noise in a two-component BEC. In our experiment, the phase evolution of a two component BEC is described by Eq. (2.27), which contains a nonlinear term $\chi \hat{S}_z^2$. The effect of this term is to produce spin-squeezing in one direction at a cost of anti-squeezing in the perpendicular direction by introducing one-axis twisting dynamics. The anti-squeezing can be understood as phase diffusion as following. A state with well-defined phase has a spin uncertainty along z -axis ΔS_z , since the relative number of atoms $\hat{M} = \hat{N}_1 - \hat{N}_2$ and the relative phase between the two components of a BEC are conjugate non-commuting variables. The nonlinear term, which can be regarded as $\chi \hat{S}_z \times \hat{S}_z$, leads to a phase evolution around z axis with an coefficient χS_z and translates the spin uncertainty along z -axis $\Delta \hat{S}_z$ to the phase uncertainty. For a coherent spin state with an equal superposition of the two states, where $\text{Var}[\hat{S}_z] = \langle N \rangle / 4$, the phase noise after a time t is^[123].

$$\Delta\phi(t) = \frac{\sqrt{\langle N \rangle}}{2} \chi t, \quad (4.9)$$

where χ is given in Eq. (2.30).

The phase diffusion is important for the phase dynamics and in most cases it cannot be ignored. However, in our case, overlapping components and nearly identical scattering lengths render its contribution very small. For an estimate, considering the parameters of our experiments with $\langle N \rangle = 1000$ atoms in a trap of frequencies (114, 714, 714) Hz, when the two components occupy the same spatial mode, we have $\chi/2\pi \approx 4.8 \times 10^{-4}$ Hz. Therefore, even for a very long interrogation time, for example $T_R = 1$ s, the phase diffusion is approximately $\Delta\phi = 0.047$ rad.

4.3.1.2 Collisional clock-shift

Now we turn to the linear term $\hbar \tilde{\chi} \hat{N} \hat{S}_z$, which arises from the difference between the collisional interaction energies in the two components. The interaction energy scales with the particle number. This term gives an additional rotation around the z -axis of the Bloch sphere and the angle of such rotation is proportional to the parameter $\tilde{\chi}$ and the total atom number \hat{N} of the system. For repeated preparations of BECs, atom number fluctuates

because of the imperfect control during the preparation of the BEC, for example, the shot-to-shot fluctuation of the current that are used for generating the trapping potential, or the shot-to-shot fluctuation of the frequency of the RF field used for evaporative cooling. The atom number fluctuation constitutes an unavoidable source of phase noise.

In the following, we will denote with \hat{N} the total atom number operator, with N the measured atom number in a single shot of the experiment, with $\langle N \rangle$ the mean of different shots, and with ΔN its standard deviation. In our experiment the fluctuations in atom number are typically much smaller than the atom number, $\Delta N \ll \langle N \rangle$.

Let us consider an experimental shot with N different from $\langle N \rangle$. The term $\tilde{\chi}(\langle N \rangle - \hat{N})\hat{S}_z$ in Eq. (2.27) gives an additional deterministic rotation around the z -axis by an angle $\tilde{\chi}(\langle N \rangle - N)t$. This effect is called clock shift. In the experiments aiming for atomic clocks, it constitutes the most important source of frequency shifts and has been studied extensively before as a source of technical noise, both in BECs^[38,79] and thermal clouds^[25,83,124]. Although in some of the mentioned references this effect is regarded as a technical source of noise, the physics behind it is actually very profound, especially when the atom losses, which happen stochastically, are considered. Now let us first ignore the stochastic nature of the atom losses and assume a deterministic change in atom number. In this simplified case, one can estimate the collisional clock-shift phase noise

$$\Delta\phi(t) = \Delta N \tilde{\chi} t , \quad (4.10)$$

where $\tilde{\chi}$ is given in Eq. (2.29). In our experiment, the initial fluctuations in atom number are small enough $\Delta N \approx 40$, therefore $\tilde{\chi}$ can be assumed as a constant for each fixed T_R . This term actually dominates in the Hamiltonian, with $\tilde{\chi}/2\pi \approx 8.6 \times 10^{-3}$ Hz for typical parameters (the two components are spatially overlapped). For a first estimate, it implies $\Delta\phi(t) \approx 2.2$ rad for 1 s.

In this regime, measurements of the phase ϕ will show a linear dependence on the total atom number N because of the N -dependent rotation, see in Figure 4.6(a), which can be extracted by fitting the phase as a function of atom number

$$f(N) = \gamma(T_R)N + \beta , \quad (4.11)$$

where $\gamma(T_R)$ and β are free parameters. If we assume that the one-axis twisting strength χ is 0 and the atom losses are deterministic, the slope of this function is proportional to

$\frac{\int_0^{T_R} \tilde{\chi}(t)N(t)dt}{N(T_R)}$. We can define another parameter to quantify the time-averaged clock shift

$$\alpha(T_R) = \gamma(T_R)/T_R = \frac{\int_0^{T_R} \tilde{\chi}(t)N(t)dt}{N(T_R)T_R}. \quad (4.12)$$

The value we obtain for $\alpha(T_R)$ can be used to quantify the strength of the collisional phase shifts. This parameter is extracted for each interrogation time T_R .

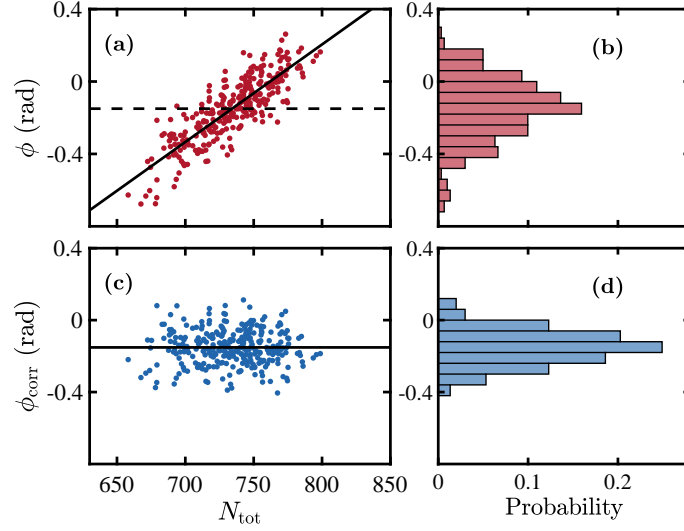


Figure 4.6 Clock-shift effect and correction. Interferometer data (a,c) and histogram (b,d) at fixed time $T_R = 100$ ms and fixed ϕ_R , with the raw data (red) and data after the correction of collisional phase shift (blue). Black curves are a linear fit of the data. The raw ϕ shows a dependence on N , while after correction the slope is zero. (d) shows a reduced phase uncertainty compared to (b) due to the correction.

By subtracting this linear dependence we can post-process the data to reduce the phase fluctuations caused by atom number fluctuations, similar to what is commonly done also in atomic clocks^[25,83,124]. Again, we take different strategies for short and long interrogation times to subtract the clock-shift effect. For $T_R < 0.2$ s, as mentioned before, we collect statistics of n_{rel} on the zero-crossing slope. We can correct each n_{rel} by a simple subtraction, *i.e.*,

$$\phi_{\text{corr}} = \phi_R - (\phi_0 + \gamma(T_R)N). \quad (4.13)$$

The corrected phase $\phi_{\text{corr}} = \phi - \alpha(T_R)T_R N$, as plotted in Figure 4.6(c), shows no dependence on N . For $T_R > 0.2$ s, we measure points over the whole Ramsey fringe $(N, \phi_R, n_{\text{rel}})$ for each T_R . We fit all of these data points using a model that takes all the three parameters

$$f(N) = \gamma N + \phi_R + \beta, \quad (4.14)$$

so that each of the new data points after correction is associated to a corrected relative

atom number

$$n_{\text{rel}}^{\text{corr}} = \sin(\phi - (\varphi_0 + \phi_R + \gamma(T_R)N_{\text{tot}})). \quad (4.15)$$

The corrected dataset is used to construct a new Ramsey fringe. In Figure 4.7, the corrected data and the raw data of a Ramsey measurement are both plotted, and the new fringe shows less phase spreading and higher contrast.

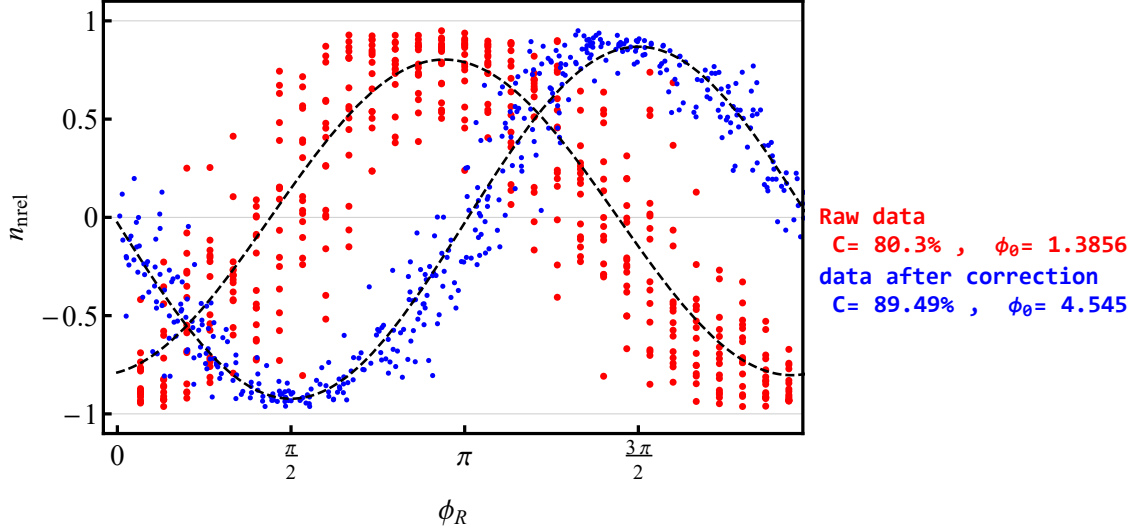


Figure 4.7 **Ramsey fringe before and after clock-shift correction.** The data points (ϕ_R, n_{rel}) for Ramsey time at 200 ms are plotted with the raw data (red) and data after the clock shift correction (blue), respectively. The dashed curves show a sinusoidal fit of the data. The fringe after the clock-shift correction shows less noise and higher contrast.

As we have shown in Figure 4.6(c, d), the clock-shift correction allows to reduce the phase shift and leads to a significant reduction of the observed phase noise. However, this correction only accounts for the coherent part of the effect. Even after the correction, there is still significant residual phase noise, which can be attributed to the random nature of atom loss.

4.3.1.3 Stochastic nature of the atom loss

Now let us consider the stochastic nature of the atom losses, which complicates the phase evolution significantly. Removing one particle from the condensate results in a change of the interaction energy, which is translated into a jump of the phase evolution. As losses are stochastic, these phase jumps occur randomly over time, giving rise to phase noise. This problem has been considered in Ref. [49], where expressions for the interference contrast in several scenarios are given.

An intuitive picture of the stochastic effect can be given as the follows. If there were

no atom losses in the system, or if the atom losses were deterministic, then the clock-shift could be completely corrected by post-processing the data, as it would depend deterministically on the initial atom number (thus it would also depend deterministically on the final atom number). However, neither of the two assumptions is true, because the atom losses are always happening stochastically, randomizing the time evolution of the atom number. Imagine the atom number as a function of time, there could be several different decay “routes” or “trajectories” leading to a same final atom number due to the random nature of the atom losses. Each of the trajectories corresponds to a different accumulation of phase because they experience different jumps of the phase evolution. Each trajectory dephases compared with the others. Moreover, in a realistic scenario there is no way to keep track of the atom number as a function of time because the quantum state will be destroyed once observed, therefore the clock-shift corrections are always based on the information of the final atom number, which is the only experimentally accessible atom number. Therefore, in practice the clock-shift correction can only subtract the “deterministic” part of the clock-shift, using the information of the final atom numbers. In Figure 4.6 and Figure 4.7, the phase fluctuations after the clock-shift correction are indeed decreased significantly compared to the raw data, however there is a considerable amount of residual noise. The residual noise can be attributed to the interplay between elastic collisions and the stochastic nature of the inelastic atom losses.

If we now look back to the Hamiltonian (Eq. (4.6)), we can see that both the linear term and the nonlinear term introduce phase noise, through the collisional phase shift and the phase diffusion. It is important to emphasize that both of these effects would be coherent if the atom losses were deterministic (in this sense they should be called dephasing instead of decoherence). However, if the stochastic atomic loss is taken into account, both terms lead additionally to an incoherent and irreversible phase evolution, since both depend on the atom numbers and their stochastic evolution, as described later by the master equation in section 4.4. This incoherent evolution is responsible for the dominant part of the residual phase fluctuations, finally leading to a fundamental limit of the phase decoherence.

4.3.1.4 Spin-dependent dynamics

Due to the difference in scattering lengths, some spatial dynamics caused by the spin-dependent interactions will set in after the first Rabi pulse. The so-called “breathing” dynamics, as already described in section 2.2.2, is also expected to modulate the contrast

of an interferometric measurement, as indicated by the overlap of the two wave functions. By solving the time-dependent 2CGPE, the spatial orbitals can be obtained. Figure 4.8 shows the simulated overlap between the two orbitals $\int |\phi_1^*(\mathbf{r})\phi_2(\mathbf{r})|^2 d\mathbf{r}$. From this figure we can conclude that the spin-dependent dynamics is not very important in our system, as this dynamics will cause the visibility to be reduced at most from 1 to 0.975. The reason is that the atomic density in our system is low and the values of the scattering lengths a_{12} , a_{11} and a_{22} are very similar to each other, differing by at most 5%. This effect can thus be neglected compared to the phase noise we are concerned about. Therefore, our approximation of each atom as an effective spin 1/2 with identical spatial mode functions for the two states and the whole ensemble as a collective spin is still well justified.

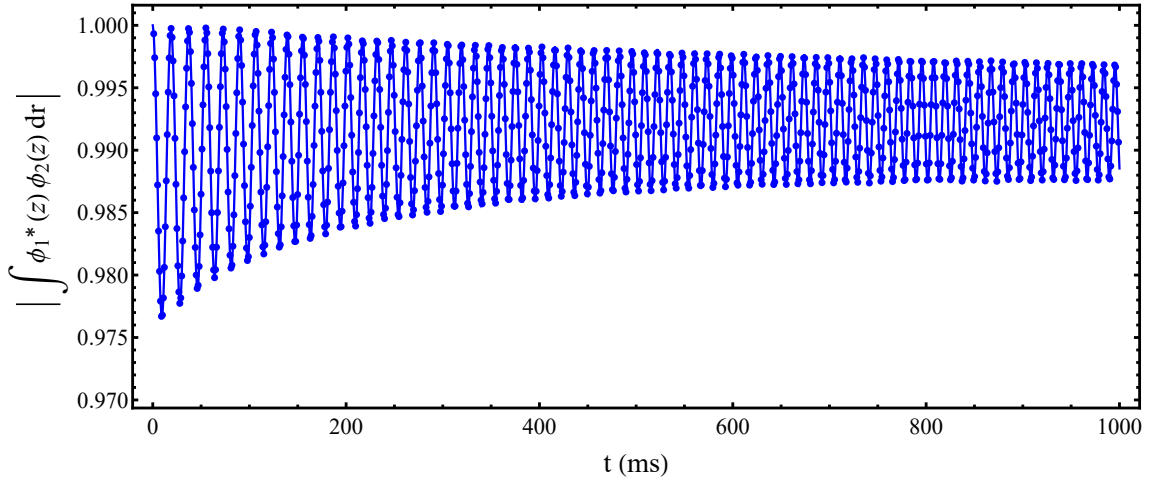


Figure 4.8 **The oscillation of the wave function overlap caused by breathing dynamics.** The wave function is simulated by 2CGPE until 1 s.

4.3.2 Technical noise

In experiments, a significant source of phase noise is the technical noise. This originates mainly from the unavoidable imaging noise existing in the detection system, the shot-to-shot fluctuations of the trapping potential due to the magnetic field fluctuations, and from the phase noise present in the local oscillator, *etc.* All these effects directly result in additional phase noise for the BEC, typically added up quadratically because the relevant technical noise processes are uncorrelated,

$$\Delta\phi_{\text{tech}}^2 = \Delta\phi_{\text{LO}}^2 + \Delta\phi_B^2 + \Delta\phi_{\text{det}}^2 + \dots \quad (4.16)$$

4.3.2.1 Local oscillator noise

In our experiment, all the MW and RF signals are referenced to the local oscillator and any of the frequency noise of these signals will be converted to phase noise of the

second $\pi/2$ pulse in the Ramsey sequence, leading to dephasing. This is the main source of technical noise from which the Ramsey experiments are suffering. The contribution of local oscillator noise can be written as

$$\Delta\phi_{\text{LO}}^2 = \frac{1}{2} \int_0^{+\infty} |H(\omega)|^2 S_\phi(\omega) d\omega ,$$

where $H(\omega)$ is the interferometer transfer function and $S_\phi(\omega)$ is the phase noise density spectrum of the local oscillator. From the specified noise spectrum of the local oscillator sources we obtain $\Delta\phi_{\text{LO}} \approx 10$ mrad at $T_{\text{R}} = 1$ s.

4.3.2.2 Fluctuation of magnetic field

As known from the experience gathered by atomic clock experiments^[6,25,124-125], the fluctuations of the magnetic field directly cause shifts of the hyperfine transition due to the second order Zeeman effect. Consider a fluctuation of the magnetic field $\delta\mathbf{B} = \mathbf{B}_0 - \mathbf{B}_{\text{magic}}$, where \mathbf{B}_0 is the actual offset field at the center of the trapping potential, and $\mathbf{B}_{\text{magic}}$ is the magic field which we desire the magnetic center to be. This shift of magnetic field causes the fluctuation of the static trapping potential, thus changes the frequency of the hyperfine transition between the two states. In this scenario, the distribution of the transition frequency throughout the trap can be characterized by a standard deviation^[125]

$$\Delta\nu_B(\mathbf{r}) = \frac{bm^2}{\mu_B^2} (\omega_x^2 x^2 + \omega_y^2 y^2 + \omega_z^2 z^2 - 2gz + \delta B \frac{\mu_B}{m})^2,$$

where $b = 431$ Hz/G² is the coefficient of the quadratic Zeeman shift, the term $-2gz$ accounts for the displacement of the BEC from the trap center caused by gravity. The magnetic field noise leads to an additional noise of the transition frequency that can be converted to phase noise between the two states. One can calculate the phase noise by error propagation formula and obtain

$$\Delta\phi_B^2 = \left(\frac{\partial\Delta\nu_B}{\partial B} \right)^2 \sigma_B^2.$$

4.3.2.3 Detection noise

As described in section 3.4, our imaging system provides an extremely precise measurement of the atom numbers. However, this does not imply that we should neglect the detection noise. In our experiment, the precision of the photon number collected in each CCD pixel is limited by the photon shot noise. This photon shot noise is later converted

to atom number noise, resulting in a noise of n_{rel} .

$$\Delta\phi_{\text{det}}^2 \approx \Delta n_{\text{rel, det}}^2 \approx \frac{(\sigma_{\text{det},1}^2 + \sigma_{\text{det},2}^2)}{\langle N \rangle^2}.$$

We will denote with N_i the atom number of state $|i\rangle$ in a single shot of the experiment, and with $\sigma_{i,\text{det}}$ its standard deviation. In the experiments presented here, the atom number detection noise has a standard deviation of $\sigma_{\text{det},1} \approx 3.6$ and $\sigma_{\text{det},2} \approx 4.1$ atoms for the two states, resulting in an equivalent phase noise of $\Delta\phi_{\text{det}} \approx 5.3 \times 10^{-3}$ rad for $T_R = 0$ and $\Delta\phi_{\text{det}} \approx 1.9 \times 10^{-2}$ rad for $T_R = 1$ s, which is negligible compared to all other sources of noise. Even though the detection noise is negligible, it's fully accounted for and added to the simulation results together with the other technical sources of noise.

4.3.2.4 Overall estimation of the technical noise

In order to have an overall estimate of technical noise, we perform the Ramsey measurement with non-condensed atoms. The thermal atomic cloud is much more dilute, therefore atom interactions, which is density dependent, is much weaker. With the effects of interactions described by the spin Hamiltonian (Eq. (4.6)) being largely suppressed, the remaining sources of phase noise are mainly the technical ones. Of course, one cannot exclude the interaction-induced noise, but the results can be regarded as an upper bound to the technical noise. To decrease the atomic density as much as possible we perform the experiment not only with a thermal ensemble, but also in the relaxed trap with trapping frequency $\omega_{(x,y,z)} = 2\pi \times (113, 301, 301)$ Hz. The results of this experiment can be well fitted with a linear model $\Delta\phi_{\text{tech}}(t) = 0.1 \text{ (rad/s)} \times t$ for $T_R < 12$ s. The fit is used as an upper bound on the technical noise in our experiment, shown in Figure 4.12 with a black dashed line. We want to emphasize that this technical noise bound is presented in standard deviation, thus shows a linear scale, while the different types of noises only add quadratically as $\Delta\phi^2 = \Delta\phi_{\text{intrinsic}}^2 + \Delta\phi_{\text{tech}}^2$ since they are uncorrelated phase noises. Therefore, actually the technical noise contributes little to the observed phase noise in our experiment.

4.4 Simulation via Monte Carlo wave-function method

Now we know that in our system the most significant noise contribution comes from the atomic interaction and its interplay with the atom losses. We can build a theoretical model to quantitatively describe the phase spread taking these effects into consideration.

The major challenge is how to deal with the stochastic behaviour of the atom losses. This effect can be reproduced in a Monte Carlo wave-function simulation (or quantum trajectory simulation), which is well suited for studying the evolution of the system.

4.4.1 Master equation in a stochastic formulation

The phase dynamics in our system can be described with a master equation, which models the dynamics of the collective spin under the elastic collisions, the stochastic atom losses and the interplay between them^[74]. To adopt the Monte Carlo wave-function method, we define four jump operators to represent the phase jump caused by the four types of significant losses in our system:

$$(\hat{C}_1, \hat{C}_2) = (\sqrt{K^{(1)}}\hat{a}_1, \sqrt{K^{(1)}}\hat{a}_2), \quad (4.17)$$

$$(\hat{C}_3, \hat{C}_4) = (\sqrt{\gamma_{12}}\hat{a}_1\hat{a}_2, \sqrt{\gamma_{22}}\hat{a}_2^2), \quad (4.18)$$

where the jump operators \hat{C}_1 and \hat{C}_2 describe the one-body losses in component $|1\rangle$ and $|2\rangle$, respectively, and \hat{C}_3 and \hat{C}_4 describe the two-body losses in state $|1\rangle$ or $|2\rangle$ (atom losses described in section 4.1). \hat{a}_i is the bosonic operator annihilating atoms in the $|i\rangle$ state. The parameters γ_{ij} are the integrated two-body loss rates, i.e. $\gamma_{ij} = \frac{K_{ij}^{(2)}}{2} \int d\mathbf{r} |\phi_i|^2 |\phi_j|^2$, where $|\phi_j\rangle$ is the wave function of state $|j\rangle$, with $i, j \in 1, 2$. With these operators, the master equation can be written in a stochastic formulation:

$$\frac{d\hat{\rho}}{dt} = -\frac{i}{\hbar} [\hat{H}, \hat{\rho}] + \sum_{k=1}^4 \hat{C}_k \hat{\rho} \hat{C}_k^\dagger - \frac{1}{2} \hat{\rho} \hat{C}_k^\dagger \hat{C}_k - \frac{1}{2} \hat{C}_k^\dagger \hat{C}_k \hat{\rho}, \quad (4.19)$$

where the Hamiltonian \hat{H} is defined in Eq. (2.27). This master equation considers the effects introduced by the clock-shift and the one-axis twisting, as well as the random phase jump due to the atom losses. The dynamics of the system described by this master equation is usually solved by carrying out numerical calculation^[126-127]. The procedure of a Monte Carlo wave-function simulation is usually done as followings.

To make sure that the simulation models our experiment accurately, the starting conditions of the simulation must be set carefully. The simulation starts at $t = 0$ with wave functions satisfying an equal superposition of the two spin states. The initial total number of atoms $N(t = 0)$ is drawn from a Gaussian distribution with mean atom number $\langle N(t = 0) \rangle$ and standard deviation $\sigma_{N(t=0)}$ as observed in the experiment and then partitioned into the two components according to a binomial distribution.

Starting with a state with a chosen total number of particles $N(t = 0)$, the initial

wave function is written as $|\psi(0)\rangle$ (normalized to unity). This wave function undergoes an evolution ruled by a non-Hermitian Hamiltonian, with the random quantum jump \hat{C}_i occurring at a rate $\langle\psi(0)|\hat{C}_i^\dagger\hat{C}_i|\psi(0)\rangle$. The Monte Carlo wave function $\psi(t)$ at the time instant t can be written as state vector in the Fock basis

$$|\psi(t)\rangle = \sum_{N_1=0}^{N(t)} c_{N_1} |N_1, N - N_1\rangle$$

where $N(t)$ is the total atom numbers at time t , $|N_1, N - N_1\rangle$ are the Fock states with N_1 and $N_2 = N - N_1$ atoms occupying the stationary spatial orbitals of state $|1\rangle$ and $|2\rangle$, respectively. In a numerical calculation, we take a time step ϵ , during which the probability of a quantum jump is equal to

$$dp_\epsilon = \epsilon \langle\psi(t)|\hat{C}_i^\dagger\hat{C}_i|\psi(t)\rangle.$$

The randomness of atom losses is mimicked by choosing a random number dp from a uniform distribution between 0 and 1. Depending on whether $dp \leq dp_\epsilon$ or $dp > dp_\epsilon$, atom losses happen or not. In the former case, the quantum jump \hat{C}_i occurs, causing two effects: it replaces $|\psi(t)\rangle$ by $\hat{C}_i|\psi(t)\rangle$ and changes the Hamiltonian \hat{H} correspondingly.

Physically one can understand the above procedure as the followings. The initial wave function $|\psi(0)\rangle$ evolves according to the Hamiltonian Eq. (2.27), with the parameters in \hat{H} corresponding to a total atom number $N(0)$. This evolution is interrupted after a random time τ_1 , when the first m -body collisional process occurs and causes the loss of m particles from the condensate. From this time on, the spin Hamiltonian changes, and wave function evolves in a system with $N - m$ atoms until time τ_2 , when a second particle loss process happens. This process continues until the chosen total evolution time T_R .

Since the losses are stochastic, at each numerical realization, this procedure will yield a particular atom number decay trajectory, thus a particular stochastic realization $|\psi(t)\rangle$. In our simulation we simulate 2000 trajectories for each T_R . Each trajectory gives a possible result of the final states $\{|\tilde{\psi}(T_R)\rangle\}$. With an adequate amount of trajectories, the whole set of final states constitutes the solution of the master equation, i.e. $\sum |\tilde{\psi}(T_R)\rangle\langle\tilde{\psi}(T_R)| \approx \hat{\rho}(T_R)$. In the frame of our model, the phase evolution can then be determined numerically from the wave functions obtained by the above procedure.

4.4.2 Semi-stationary solution

In our simulation we model the spin dynamics by assuming a zero-temperature BEC, that is, we assume that at any time the spatial mode of each internal state can be described

by the single-particle ground state wave function given by the corresponding GPE, and we neglect any thermal excitations out of the mode due to finite temperature or due to the loss processes. These assumptions allows us to compute the spatial orbitals and the key parameters χ , $\tilde{\chi}$ and γ_{ij} in the Hamiltonian by solving the 2CGPE.

For the time scale of interest (up to 1 s), the atomic densities decrease significantly due to atom losses. As a consequence, the parameters χ , $\tilde{\chi}$ and γ_{ij} also change significantly with time. We have learned the loss rates change in time due to two effects: (a) Breathing dynamics. The initial $\pi/2$ Rabi pulse breaks the equilibrium of the system and the clouds start to “breathe”. The overlap and local densities oscillate in time, which makes the two-body loss rates also time dependent. (b) Decrease of the average atom numbers $\langle N_1 \rangle$ and $\langle N_2 \rangle$. Even if there were no breathing dynamics of the clouds, with only simple adiabatic dynamics, the orbitals $\phi_1(r, t)$ and $\phi_2(r, t)$ would still change in time. It happens simply because the mean numbers of atoms, which are the inputs of the GPE, decrease.

The time-dependence of the atom numbers, as well as the parameters $\chi(t)$, $\tilde{\chi}(t)$ and $\gamma_{ij}(t)$, must be taken into account in the master equation. Ideally one should solve the GPE at every time-step when a quantum jump happens, however this is extremely time-consuming and expensive numerically. Therefore, we use *semi-stationary model* to capture the main physics. That is, we assume that the breathing dynamics can be neglected and the atomic densities follow adiabatically the 2CGPE ground states, which applies well in our case given the experimental parameters (nearly identical scattering length). Thus one can solve the stationary GPEs at some chosen instants of time for the mean numbers of atoms in the system and then interpolate the resulting parameters. For each chosen time instant, the time-dependent average numbers of atoms in two states $\langle N_1(t) \rangle$ and $\langle N_2(t) \rangle$ are already known from the experiment, and they agree with the simulations of the 2CGPE, see Figure 4.1, and the Hamiltonian parameters $\chi(t)$ and $\tilde{\chi}(t)$ can be computed using the following stationary 2CGPE with the time dependent average number of atoms $\langle N_1(t) \rangle$ and $\langle N_2(t) \rangle$ as input.

$$\mu_1 \phi_1 = \left(-\frac{\hbar^2 \nabla^2}{m} + U_1 + g_1 N_1(t) |\phi_1|^2 + g_{12} N_2(t) |\phi_2|^2 \right) \phi_1, \quad (4.20)$$

$$\mu_2 \phi_2 = \left(-\frac{\hbar^2 \nabla^2}{m} + U_2 + g_2 N_2(t) |\phi_2|^2 + g_{12} N_1(t) |\phi_1|^2 \right) \phi_2. \quad (4.21)$$

The time-dependence of the orbitals comes into this model from the time-dependence of the average numbers of atoms. Subsequently, one can use the definitions to find the time-

dependent parameters $\chi(t)$, $\tilde{\chi}(t)$, $v(t)$, and loss rate γ_{12} and γ_{22} . The unitary part of the dynamics is generated by

$$H_{\text{adiab}} = \chi(t)S_z^2 + (v(t) + \tilde{\chi}(t))S_z.$$

The losses are included in the master equation with time-dependent loss-rates:

$$\gamma_{22}(t) = K_{22} \int d\mathbf{r} |\phi_2(\mathbf{r}, t)|^4 / 2, \quad (4.22)$$

$$\gamma_{12}(t) = K_{12} \int d\mathbf{r} |\phi_2(\mathbf{r}, t)|^2 |\phi_1(\mathbf{r}, t)|^2 / 2 \quad (4.23)$$

The orbitals $\phi_1(\mathbf{r}, t)$ and $\phi_2(\mathbf{r}, t)$ are solutions of time-dependent GPE equations, with $\langle N_1 \rangle$ atoms in state $|1\rangle$ and $\langle N_2 \rangle$ atoms in state $|2\rangle$.

In Figure 4.9, the loss rates γ_{12} and γ_{22} found from the direct time-dependent GPE simulation are compared with the results of the semi-stationary model. In the semi-stationary model we neglect the breathing dynamics, therefore no fast oscillations is present, but the main physics is captured. For scattering lengths which are close to each other, or for shallow traps, the spatial dynamics has a very small impact. Typically, one needs very tight steep traps (on the order of 2 kHz) and Feshbach resonances to see the effects of the spatial dynamics.

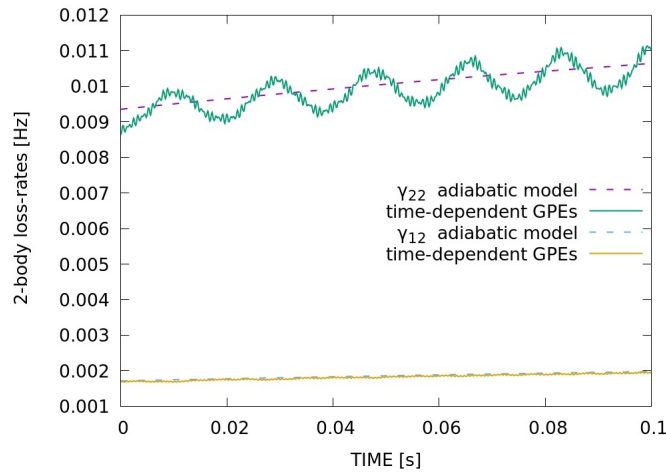


Figure 4.9 **Time-dependent two-body loss rates** $\gamma_{12}(t)$ and $\gamma_{22}(t)$ evaluated for trap with frequencies $\omega_{(x,y,z)} = 2\pi \times (114, 714, 714)$ Hz: results based on solving 2CGPE (solid lines), and semi-stationary model (dashed lines).

Note that such an approach implies that the quantum states with different atom number decay trajectories evolve with the same parameters $\chi(t)$, $\tilde{\chi}(t)$, and $\gamma_{ij}(t)$, all determined by the mean atom number trajectory $\langle N_1(t) \rangle$ and $\langle N_2(t) \rangle$. In other words, the deviations of the parameters $\Delta\chi(t)$, $\Delta\tilde{\chi}(t)$, and $\Delta\gamma_{ij}(t)$ are ignored. However, these are only higher

order effects, and within the accuracy of our model it is sufficient to consider the mean value of these parameters.

4.4.3 Scattering length

The phase noise evaluated from Eq. (4.19) is very sensitive to the initial conditions and to the fundamental constants that enter the master equation as inputs. Besides the loss rates which have been measured again in our experiment, the precise values of the s -wave scattering lengths is of significant importance, especially the difference between a_{11} and a_{22} , which affects the parameter $\tilde{\chi}$ crucially. Values of the scattering length can be found in different Refs. [38,44-45,120,128], as summarized in Table 4.2.

Table 4.2 Previously measured scattering lengths from the literature

reference	a_{12}/a_0	a_{22}/a_0	$(a_{11} - a_{22})/a_0$
Matthews ^[128]		95.54	5.86
Harber ^[38]	98.09	95.47	4.93
Mertes ^[45]	97.66	95.0	5.40
Egorov ^[44]	98.01	95.4	4.96
van Kempen ^[120]	98.175		

To decide which group of values for the scattering lengths should be used as input of the theoretical model, we run the Ramsey sequence with $T_R = 10$ ms with varying initial atom numbers and extract $\tilde{\chi}$. For this short interrogation time, atom losses are negligible, thus $\alpha \approx \tilde{\chi}$. The 2CGPE simulation with values of scattering lengths taken from Ref. [44] shows a good agreement with the experiment, see Figure 4.10.

4.5 Comparison of experiment and theory

What we obtained from the Monte Carlo wave-function simulation is a “database” of stochastic wave functions which have evolved until the final time T_R , but before the second Rabi pulse. To compare the phase noise obtained from our theoretical model with that of the experiment, we mimic Ramsey measurements numerically using these wave-functions. In each “measurement” shot, one wave function is randomly chosen from the whole database and rotated by a “Rabi” pulse to measure n_{rel} , and the measurement is repeated for the same amount of times as the experiment. The resulted data are treated as experimental realizations: they are post-processed to extract contrast, visibility, clock-shift

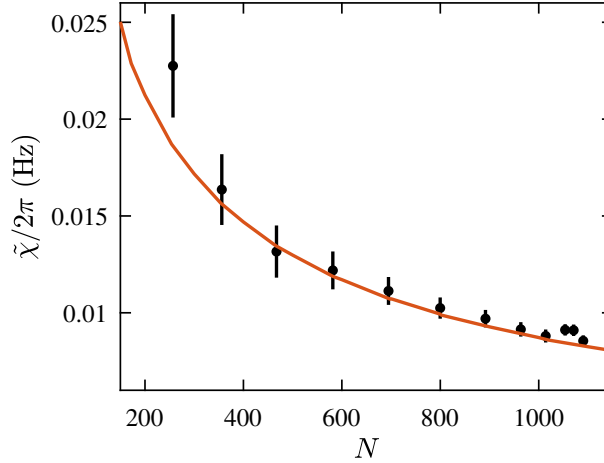


Figure 4.10 **Comparison of the extracted initial $\tilde{\chi}$ between experiment (black dots) and 2CGPE simulation (red line).** For BECs with varying initial atom numbers we extract $\tilde{\chi}$ with a Ramsey sequence of $T_R = 10$ ms.

correction and phase noise, in exactly the same manner as we do in the real measurements.

To verify the validity of the simulation, there are several cross-checks that can be done. An important one is α (defined in the fitting model of the clock-shift, see Eq. (4.12)) as a function of time. It can be both computed by the simulation and from the experimental data. Figure 4.11 shows the comparison and we find a reasonable agreement between theoretical and experimental data.

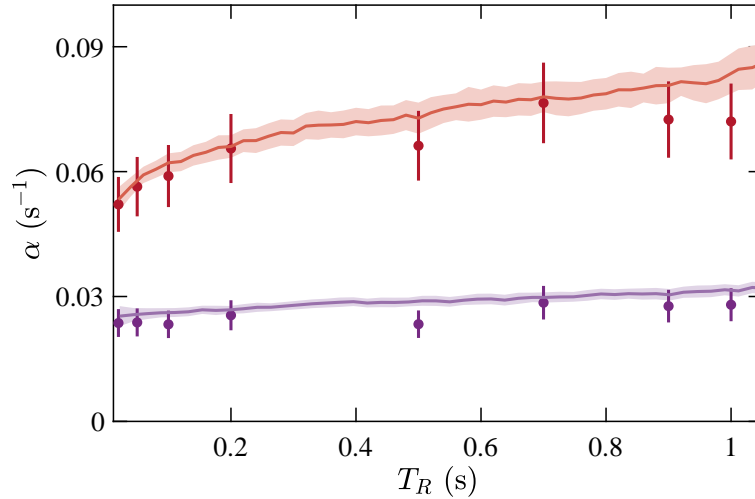


Figure 4.11 **Comparison of the extracted collisional phase shift coefficient $\alpha(t)$ between experiment (dots) and Monte Carlo simulation (solid lines).** The red dots and curves are for the tight trap $\omega_{(x,y,z)} = 2\pi \times (114, 714, 714)$ Hz (red) and the purple ones are for the relaxed trap $\omega_{(x,y,z)} = 2\pi \times (113, 301, 301)$ Hz.

Furthermore, in order to ensure an appropriate comparison with the experiment, we also add the technical noise on top of the simulation results (although we know it is very small). Note that the technical noise in standard deviation is added up quadratically since

the noise sources are uncorrelated. In Figure 4.12, the results of the quantum trajectory simulations are compared with the experimental results. The simulation accurately reproduces the observed increase of phase noise, both before and after the clock-shift correction. We also show in Figure 4.6(e) the simulated and measured collisional phase shift as a function of time.

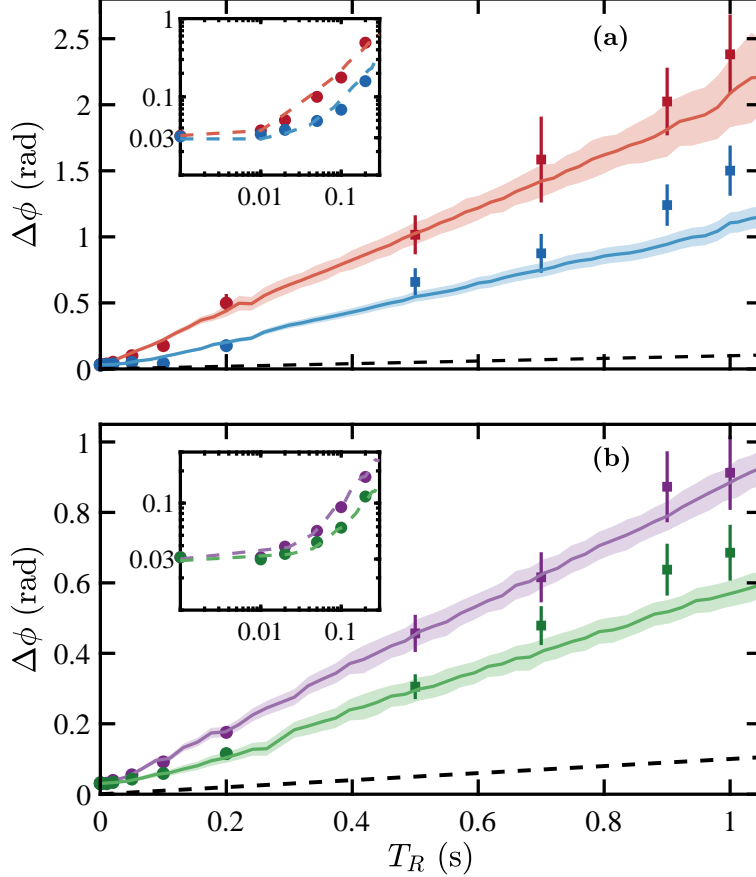


Figure 4.12 **Phase noise as a function of T_R** is shown for a tight trap with $\omega_{(x,y,z)} = 2\pi \times (114, 714, 714)$ Hz (a) and a shallow trap with $\omega_{(x,y,z)} = 2\pi \times (113, 301, 301)$ Hz (b). Experimental results are shown before (red and purple) and after collisional phase shift correction (blue and green). Dots and square symbols represent data at $T_R < 0.2$ s and $T_R > 0.2$ s respectively, evaluated with different methods (see text). Results of quantum Monte-Carlo wave function simulations are given by the solid line with corresponding color. Black dashed lines show the upper bound on technical noise (see text). The insets show the phase noise at $T_R < 0.2$ s in a log-log scale. The minimal phase uncertainty is close to the projection noise of a coherent spin state $\Delta\phi = 1/\sqrt{N} \approx 0.033$ rad.

Our zero-temperature model already accounts for the vast majority of the observed fluctuations. Only for very long T_R it slightly underestimates the phase noise. This shows that the phase coherence is limited mainly by the interplay between atomic collisional interactions (elastic and inelastic). The discrepancy at long T_R can be explained by finite temperature effects. When constructing the theoretical model, we assume a zero-

temperature BEC because we do not observe thermal component in the absorption images for any of the investigated interrogation times. For clarification, the imaging system is capable of detecting thermal fractions in our trapping geometry, as confirmed in independent experiments where we on purpose increase the temperature of the condensates to be closer to the critical temperature. However, in real experimental realizations, the BECs are inevitably at finite temperature with a fraction of non-condensed particles always present. This remaining thermal fraction of atoms represents a fluctuating environment that perturbs the condensate phase through interactions. This might explain why at long T_R the phase noise increases faster than predicted by our theoretical model. Interestingly, the effect of phase spreading due to finite temperature has never been measured in three-dimensional BECs. The investigation of such effects would however be of significance to understand the coherence of BECs and needs to be explored in the future.

To extend the coherence time, one can decrease the gas density, and thereby reduce the collisional rates. We confirmed this by performing the phase noise measurement in a relaxed trap with trap frequencies $\omega_{(x,z)} = 2\pi \times (301, 113)$ Hz. As shown in Figure 4.12(d), the phase noise is indeed strongly reduced. In order to reach the fundamental bound of precision limits in quantum metrology as theoretically described in Refs. [129-130], the unwanted effects of decoherence should be further mitigated. Experimentally, a state-dependent potential could be applied to engineer interactions^[49]. Using this technique, one can minimize $\tilde{\chi}$, thus the collisional phase shift, or tune the interactions so that the quantum states are protected from the decoherence induced by two-body losses, as proposed in Ref. [131].

In conclusion, we measure precisely the growth of the phase noise in a trapped two-component BEC and identify the main decoherence sources. We observe that the coherence is limited by random collisional phase shifts due to the stochastic nature of atom loss. Our experimental findings provide a good understanding of the temporal coherence of a two-component BEC. In contrast to most other systems, where decoherence is dominated by interactions with the environment, in our experiment the atoms are well-isolated, and the observed decoherence effect is intrinsic to such a two-component BEC.

CHAPTER 5 NON-CLASSICAL RAMSEY INTERFEROMETER

For any two-mode interferometer performing with N uncorrelated or classically correlated atoms, the phase uncertainty is limited by the standard quantum limit (SQL)^[11], equal to $1/\sqrt{N}$. Entanglement between the particles, as a type of quantum resource, can be employed in non-classical interferometer to enhance the measurement precision beyond the SQL. Non-classical interferometers have been demonstrated in different systems, with different mechanisms to prepare non-classical states. In our experiment, we mainly use a particular type of entangled states: spin-squeezed states, which we prepare by inducing one-axis twisting (OAT) dynamics^[20]. In the past decade, the OAT mechanisms and related experimental tools have been extensively studied^[17,90,132]. In our group, the experimental generation of spin-squeezing was first demonstrated in Ref. [29]. Later the technique of reconstructing a state tomography to characterize the spin-squeezed state was developed^[133]. An atom interferometer using spin-squeezed state was used to measure the magnetic field and achieved a precision beyond the standard quantum limit^[19]. Recently, we have prepared and measured the entanglement between two parts of a BEC^[104].

Despite these state-of-art techniques to prepare and characterize the spin-squeezing, we are motivated by a need of improving the spin squeezing. A more reliable and higher spin squeezing not only helps to improve the precision of interferometric measurements, but also reflects deeper entanglement in the many-body system. In this chapter, we will present the most recent results of our spin-squeezing experiment, with the best spin-squeezed state achieving a Wineland spin-squeezing parameter of $\xi^2 = -9.8(5)$ dB, which is a significant improvement compared to previous experiments on our apparatus. The strategies for improving the spin-squeezing will be discussed. Moreover, we perform a non-classical Ramsey interferometer with a spin-squeezed state, with interrogation time as long as $T_R = 1$ s. The measurement precision has been investigated as a function of interrogation time, and showed a precision better than classical bound by 7 dB.

5.1 Preparation of spin-squeezed state

In this section, we will give a brief review of the spin squeezing mechanism and of the involved techniques in our experiment.

5.1.1 One-axis twisting Hamiltonian

In our system, the one-axis twisting originates from the collisional interactions between atoms, described by the non-linear term $H_{\text{int}} = \chi \hat{S}_z^2$ in the Hamiltonian Eq. (2.27). Starting with a coherent spin state, atoms are initially uncorrelated and the quantum noise is isotropically distributed among the spin quadratures orthogonal to the mean spin, satisfying the Heisenberg uncertainty relation $\text{Var}(\hat{S}_y)\text{Var}(\hat{S}_z) = |\langle \hat{S}_x \rangle|^2/4$. Under the one-axis twisting Hamiltonian, the state will dynamically evolve into a spin-squeezed state in which atoms in the condensate are entangled^[49]. The quantum noise along a particular quadrature will then be suppressed, at the cost of increasing the noise along the orthogonal quadrature, resulting in a spin-squeezed state with anisotropically distributed spin variance.

An essential feature of our experiment is the ability to control the strength of the non-linearity by tuning the collisional interactions. As it can be seen from the definition of χ , this term originates from the difference between the total intra-species interaction energy and the total inter-species interaction energy. As Eq. (2.32) suggests, the strength χ of the non-linear Hamiltonian depends on the wave-function overlap of the two states. It is nearly zero for identical and overlapping components due to the nearly identical scattering lengths $a_{22} \sim a_{11} \sim a_{12}$, while it increases by several orders of magnitude for completely separated components^[29]. Experimentally, we can use the microwave state-dependent potential (discussed in section 3.3.3) to split the two components, as shown in Figure 5.1.

The ability to spatially separate the two BEC components allows us to control the collisional interactions between them, effectively controlling the coefficient χ of the nonlinear dynamics. We denote the displacement of the two trap minima as Δx_0 . It is important to notice that the displacement between the trap minima Δx_0 is not equal to the *in situ* displacement between the centers of mass of each spin component d , as shown in Figure 5.1. Typically, a splitting of $\Delta x_0 \approx 400$ nm for the the trap potential minima for the two states (much less than the extension of the BEC size of $R \approx 5$ μm) will increase the non-linear term coefficient χ by a factor of more than 2000.

5.1.2 Sequence to prepare the spin-squeezed state

To prepare the spin-squeezing in the system, we use the sequence visualized in Figure 5.2. To give an intuitive picture of the quantum state on the Bloch sphere, the expected Wigner distribution of the corresponding states on the Bloch sphere at different stages are

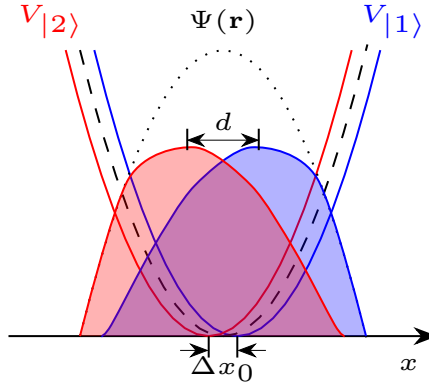


Figure 5.1 **Splitting of the two components.** The schematic for the state-dependent trapping potentials is shown with red (for $|1\rangle$) and blue (for $|2\rangle$), and the corresponding wave functions in the stationary scenario are shown in the same color. The black dashed line shows the original static magnetic trap and the black dotted line shows the wave function of atoms in it. The splitting between two trap minima is denoted as Δx_0 , the in situ displacement between the two wave functions is denoted as d . Δx_0 and d are not necessarily the same. The splitting is exaggerated for visualization, while in real case Δx_0 is approximately a few hundreds of nanometers, which is much smaller compared with the radius of the cloud $\approx 5 \mu\text{m}$.

also given. The Wigner function is calculated for $N = 200$ atoms (see section 2.3.3).

Starting with a BEC of $N \approx 1000$ atoms in state $|1\rangle$ (the state at the north pole of the Bloch sphere), a $\pi/2$ Rabi pulse is first applied to generate an equal superposition of $|1\rangle$ and $|2\rangle$. For convenience, we set the phase-reference frame such that the first rotation is around $+y$ -axis on the Bloch sphere. Therefore, the first rotation, which can be described by the unitary transformation $e^{-i\pi/2\hat{S}_y}$, prepares the state on the equator aligned with the x -axis of the generalized Bloch sphere. Immediately after the first pulse we turn on the state-dependent potential by applying an on-chip MW current, in order to initiate the one-axis twisting dynamics^[29]. We turn on and off the coplanar MW with a smooth ramp taking $350 \mu\text{s}$, which is slow enough to allow for adiabatic microwave dressing of the potential, but not adiabatic with respect to the spatial dynamics. The state-dependent potential will trigger a spatial dynamics of the two components (discussed later in section 5.1.3), causing them to split and recombine periodically. We apply the state-selective potential for a duration T_s , chosen so that the wave functions of the two components are overlapped again when the one-axis twisting Hamiltonian is turned off. During T_s , the non-linear interaction Hamiltonian $H_{\text{int}} = \chi \hat{S}_z^2$ leads to spin-squeezing, and the evolution of the states can be described by $e^{-i\hat{H}t}$. The resulting squeezed state is tilted by the one-axis twisting, thus the squeezed quadrature has an angle with respect to the equator, denoted as θ_0 .

Experimentally, the only observable of the system is the z component of the spin \hat{S}_z ,

which can be measured by detecting the atomic population in the two states. Therefore, a second Rabi pulse is needed to rotate the spin state in order to measure spin component along specific quadratures. Such a Rabi pulse always has two parameters that can be experimentally controlled: duration and phase. We denote the duration with the corresponding angle of rotation θ , and denote its relative phase with the first pulses as ϕ . These two parameters together determine along which quadrature the collective spin is measured. One can understand the second Rabi pulse as two steps: first rotate the state around the $+z$ -axis with an additional angle ϕ , and then rotate the state around $+y$ -axis by an angle θ . In this way the unitary transformation is written $e^{-i\theta\hat{S}_y}e^{-i\phi\hat{S}_z}$. An alternative (maybe easier) way to understand the second Rabi pulse is that it rotates the state by θ angle, around an axis $S_{y+\phi}$ which is in the xy -plane of the Bloch sphere and has an angle ϕ to the $+y$ -axis. In this way the rotation is described by $e^{-i\theta\hat{S}_{y+\phi}}$. Depending on the specific purpose of the experiment, the two parameters are chosen accordingly in order to measure the collective spin along a particular direction. A special case is, for the interferometric measurement, we rotate the spin-squeezed state such that the squeezed quadrature is along the equator, thus minimize the phase uncertainty of the measurement.

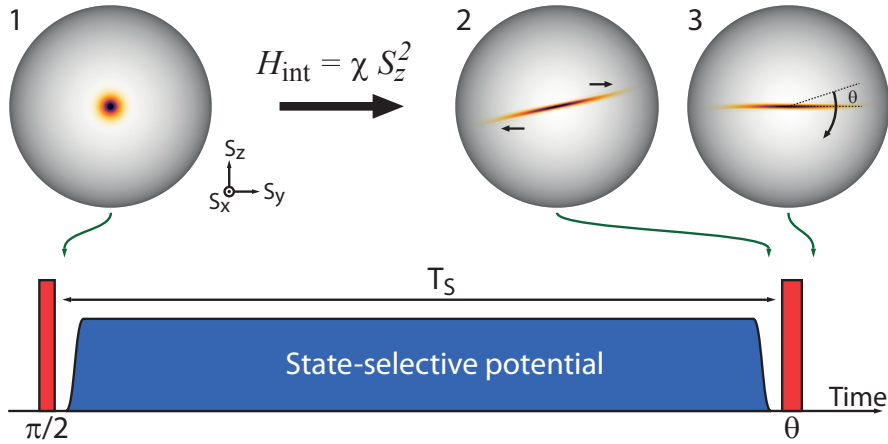


Figure 5.2 Sequence to prepare and characterize a spin-squeezed state. The red pulses represent the Rabi pulses and blue pulse shows the microwave state-dependent potential. Sphere 1 shows the initial coherent state, aligned with the x -axis. Sphere 2 shows the simulated Wigner function of a spin-squeezed state, simulated for $N = 200$ atoms under an evolution of $\chi T_s = 0.003$. To construct the squeezing tomography, different angles of rotation θ around the center of the state are performed with the second Rabi pulse. Figure adopted from^[50].

5.1.3 Spin demixing-remixing dynamics

When the state-dependent trapping potential is turned on to separate atoms in the two spin states, a mirror-symmetrical oscillation of the two atomic clouds along the separation direction will be induced, and the spatial mode of the two components will split and over-

lap periodically. We call this phenomena *demixing-remixing dynamics* (in some context also referred to as spin dipole oscillation^[134]).

In order to show the splitting and recombination of the two spatial modes, we usually perform a Ramsey sequence in the time domain^[29]. We prepare the BEC in an equal superposition of $|1\rangle$ and $|2\rangle$, and then turn on the state-dependent MW potential with a $350\ \mu\text{s}$ ramp. The microwave is on for the entire duration of the Ramsey time, until we turn it off before the final $\pi/2$ Rabi pulse that projects the phase onto atom number populations. By varying the Ramsey interrogation time, we can study the relative atom number $n_{\text{rel}} = (N_1 - N_2)/(N_1 + N_2)$ as a function of T_R , as shown in Figure 5.3(c). We observe fast oscillations, which are the typical interference fringes of a Ramsey sequence, modulated in amplitude by a slow periodic collapse and revival. This collapse and revival indicates that the demixing-remixing dynamics of the two components is coherent. To characterize the optimal times T_R where the contrast has a revival, we fit the experimental data with a modulated oscillation

$$f(T_R) = O + \left(A \left(1 + B \cos(\omega_{\text{slow}} T_R + \phi_0) \right) \right) \cos(\omega_{\text{fast}} T_R) \exp(-\gamma T_R), \quad (5.1)$$

where O , A , B , ω_{fast} , ω_{slow} and γ are fitting parameters, the exponential factor $\exp(-\gamma T_R)$ accounts for the damping of the dynamics. The red curve in Figure 5.3(c) shows a fit according to this model. From the fit, the oscillation frequency ω_{slow} can be extracted to estimate the revival times. At these revival times we can obtain a better estimate of the contrast by performing a Ramsey sequence in the phase domain. The fact that the contrast gets reduced from one revival to the next is also associated with phase spreading (anti-squeezing) of the condensate, as it is also visible from the increasing noise on the fringes. For the first two revivals we typically find a contrast in the range of 95% – 99%. For even longer times, atom losses during this process results in a reduction of the mean-field interactions, which make this dynamics faster and makes the fitting model not as reliable as before.

From the experimental data, it can be observed that the demixing-remixing frequency does not match any of the trap frequencies of the magnetic trap ($(\omega_x, \omega_y, \omega_z) = 2\pi \times (113, 301, 301)$ Hz), but is much slower because of mean-field interactions. This oscillation originates from the combination of the repulsive contact interaction between atomic clouds and the harmonic trapping potential of the state-dependent magnetic traps. For the convenience of understanding, the elastic interaction between the two atom clouds can be regarded as an effective potential. If we approximate the wave function as a

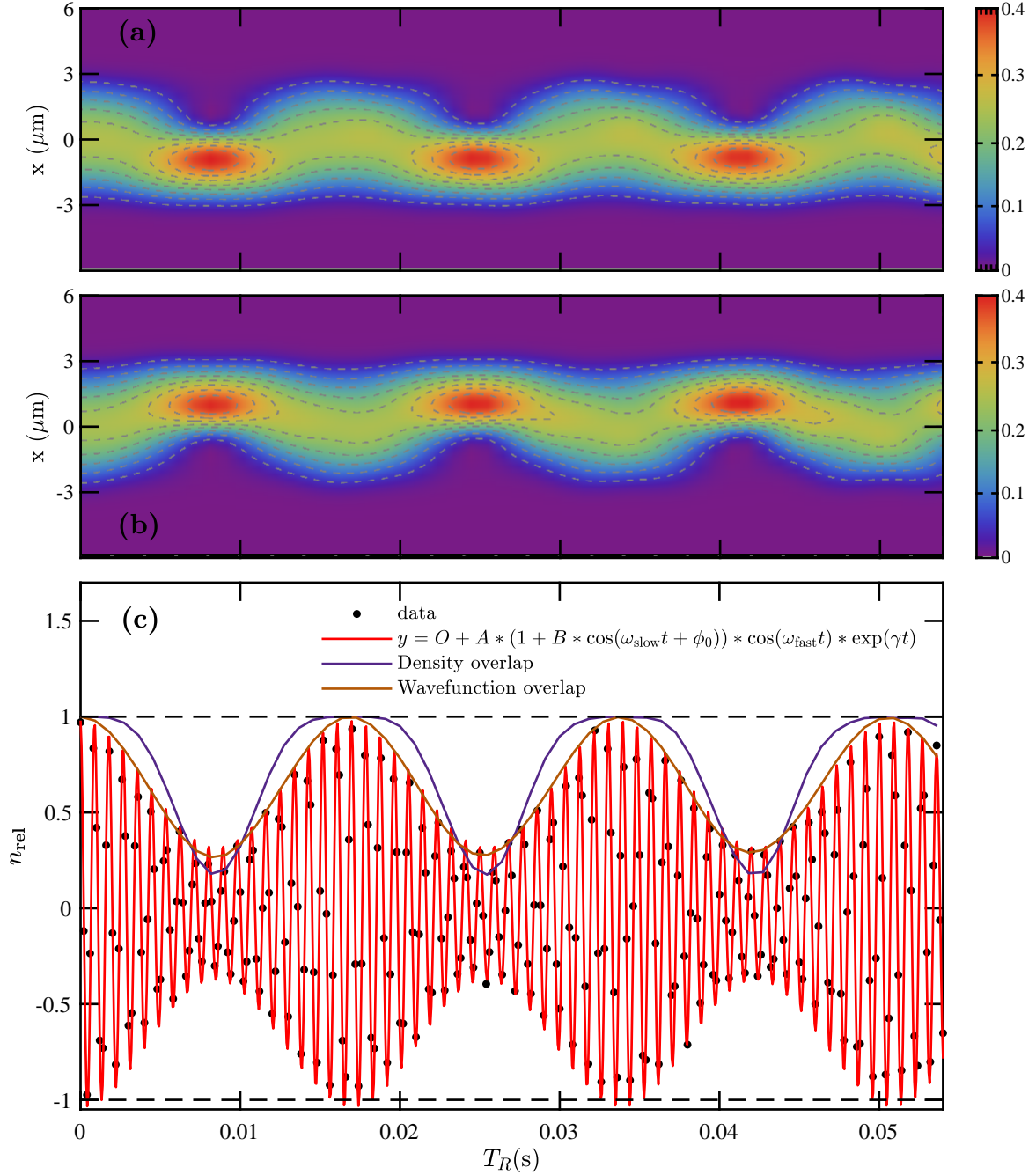


Figure 5.3 Dynamic splitting and recombination. Simulated atomic densities along the splitting direction for the two states Ψ_1 (a) and Ψ_2 (b) during the demixing-remixing dynamics, obtained from a 2CGPE simulation. The trap frequencies are $(\omega_x, \omega_y, \omega_z) = 2\pi \times (113, 301, 301)$ Hz and the displacement is 400 nm (c) Black dots are measured Ramsey fringes as a function of the interrogation time T_R , for a BEC with $N \approx 920$ atoms. During T_R the microwave near-field is applied to generate a state-dependent potential, which causes the two components to split and recombine spatially. As a result, the recorded fringe contrast shows a collapse and revival in addition to the fast oscillation. The red line is a fit of the data with the model given in Eq. (5.1). The time of recombination obtained by fitting are: $T_{1\text{st}} = 16.8$ ms, $T_{2\text{nd}} = 33.6$ ms and $T_{3\text{rd}} = 50.4$ ms, respectively. Data taken on 26.02.2020.

Thomas-Fermi distribution, *i.e.*, with an inverted quadratic function, the effective interaction potential $g(N-1)|\phi(x, d)|^2$ then takes a quadratic form as a function of the coordinate x and the distance between the centers of the two atomic wave functions d . This effective potential term can be regarded as a harmonic oscillator with negative mass, and is proportional to the overlap of the two wave functions. Under the lowest-order approximation, considering that the two atomic clouds are bounded by separated magnetic traps at the same time, the total potential for each one of the two clouds is the combination of a magnetic trap and the effective potential due to the intra-cloud repulsive interaction. Therefore, the oscillation frequency of the atomic clouds is the difference between the eigenfrequency of the magnetic trap and the aforementioned effective negative-mass harmonic oscillator. Under the experimental conditions (500 atoms in each spin state), the eigenfrequency of the effective negative-mass harmonic oscillator is ≈ 61 Hz along the direction where the two clouds are separated. This leads to a theoretical value of $113-61 = 52$ Hz for the demixing-remixing dynamics, which shows a reasonable quantitative agreement with the measured oscillation frequency. However, with increasing displacement between the two traps, some high-order effects can modify the frequency and is not covered in this model.

A more precise prediction of the demixing-remixing dynamics can be obtained with the 2CGPE. The simulation parameters are chosen to be consistent with the experiment, with a splitting along x direction of $\Delta x = 400$ nm. The atom losses and the ramp of the microwave are taken into account in the simulation. The results of the simulation show that the microwave field causes the wave functions ϕ_1 and ϕ_2 to oscillate in opposing directions. In Figure 5.3 we plot the simulated densities along the splitting direction (longitudinal direction) for the two modes $\int |\phi_{1(2)}|^2 dy dz$, the density overlap of the component densities $\int |\phi_1|^2 |\phi_2|^2 d\mathbf{r} / \sqrt{\int |\phi_1|^4 d\mathbf{r} \int |\phi_2|^4 d\mathbf{r}}$ (normalized to 1) calculated from the 2CGPE simulation, and the normalized wave function overlap $\int |\phi_1^* \phi_2| d\mathbf{r}$, which determines the visibility. The comparison with the experimental data shows that the GPE simulation can capture the main oscillation.

5.2 Characterization of spin-squeezing

5.2.1 Spin-squeezing parameters

There are two important parameters used to characterize the spin noise: the number squeezing parameter and the Wineland spin-squeezing parameter. The number squeezing

parameter ζ^2 corresponds to the measured spin variance normalized so that for an ideal coherent state on the equator (a binomial distribution) it holds that $\zeta_{\text{CSS}}^2 = 1$ [20].

$$\zeta^2 = \frac{\text{Var}[S_\theta]}{\langle N \rangle / 4} = \langle N \rangle \sigma_{n_{\text{rel}}}^2, \quad (5.2)$$

where θ is the quadrature along which the spin variance $\text{Var}[S_\theta]$ is measured and $\sigma_{n_{\text{rel}}}^2$ is the measured variance in n_{rel} . Usually, we subtract the detection noise when calculating the number squeezing, with the formula:

$$\zeta^2 = \langle N \rangle (\sigma_{n_{\text{rel}}}^2 - \sigma_{n_{\text{rel},\text{det}}}^2), \quad (5.3)$$

where $\sigma_{n_{\text{rel},\text{det}}}^2 = \frac{\sigma_{N_1,\text{det}}^2 + \sigma_{N_2,\text{det}}^2}{N^2}$ is the variance contributed by the imaging noise, which is determined independently for each dataset. In fact, very precise measurements of the atom numbers N_1 and N_2 are very important for experiments that study spin-squeezing, since it requires the resolution of the relative atom number beyond the atomic shot noise limit. Our experimental setup is highly optimized for this. Relatively long absorption imaging pulses (50 μs) in the saturated regime allow us to lower the primary source of detection noise in our system, the photon shot noise, to very low levels, so that $\sigma_{n_{\text{rel}}}^2 \gg \sigma_{n_{\text{rel},\text{det}}}^2$ for coherent spin states. Typically, the contribution of the detection noise is around $\sigma_{n_{\text{rel},\text{det}}} = (5.5 \pm 0.4) \times 10^{-3}$, corresponding to $\zeta_{\text{det}}^2 = N \sigma_{n_{\text{rel},\text{det}}}^2 \approx 0.025$. Subtracting the imaging noise contribution is not meaningful in the context of interferometry, but it can be useful for the characterization of a quantum state.

Number squeezing does *not* measure metrologically useful squeezing, but only measures noise reduction compared to the projection noise of a coherent state. The precision of an interferometric measurement also depends on the contrast, which determines the error transmission between the interferometric readout (in our case n_{rel}) and the phase. This contrast is not taken into account by the number squeezing parameter. To quantify the metrological usefulness of a quantum state, we use the Wineland squeezing parameter [135] (as mentioned in section 2.5.2)

$$\xi^2 = \frac{\langle N \rangle \text{Var}[S_\theta]}{\langle S_x \rangle^2}, \quad (5.4)$$

where we explicitly choose the frame so that x is the direction of the mean spin, and θ is a rotation angle around x which may be freely chosen in order to measure the spin variance along the squeezed direction. In an experiment, a measurement of $\text{Var}[S_\theta]$ can be performed by first rotating by an angle θ around the $-x$ axis on the Bloch sphere, and then measuring the variance of the atom number imbalance $\sigma_{n_{\text{rel}}}^2$. The spin length $\langle \hat{S}_x \rangle$

is determined from the contrast of an independent Ramsey measurement by performing rotations of the state around the y -axis. The squeezing parameter is then calculated as

$$\xi^2 \approx \frac{\langle N \rangle \sigma_{n_{\text{rel}}}^2}{C^2}, \quad (5.5)$$

The above approximation actually assumes that the interferometric contrast reflects the spin length $C \approx \frac{\langle \hat{S}_x \rangle}{S}$. It is interesting to notice that the contrast also describes the phase noise due to decoherence, as we have discussed in chapter 4. In addition, we do not subtract detection noise when calculating ξ^2 , also because this parameter aims for the description of the interferometric precision. Therefore, in Equation 5.5, technical noise sources such as imaging noise increasing $\text{Var}[S_\theta]$ and the contrast reduction due to the phase noise are all taken into account. Therefore ξ^2 compares the sensitivity of an interferometric experiment to that of a classical interferometer with the same particle number and describes the enhancement. A state with $\xi^2 < 1$ allows one to improve the phase sensitivity of an interferometer σ_ϕ^2 by a factor ξ^2 with respect to the standard quantum limit.

5.2.2 Squeezing Tomography

In order to characterize the prepared spin squeezed states, the technique of performing state tomography was developed in Ref. [133]. The idea behind the tomography is to measure the spin variance $\text{Var}[S_\theta]$ for spin components along different quadratures that are orthogonal to the mean spin. Therefore, after the preparation of a spin-squeezed state as previously described, the second Rabi pulse will rotate the state by a varying angle θ around its center. To ensure a rotation around a correct axis, the phase ϕ of the second pulse is scanned and calibrated by independent Ramsey measurements. Ideally, if the state is on the equator and the rotation axis is properly calibrated, the mean will be $\langle S_\theta \rangle \approx 0$. However, due to the asymmetric losses in the two states during T_s , the ‘‘center of mass’’ of the spin-squeezed state is not on the equator of the Bloch sphere, but slightly above the equator towards the $|1\rangle$ pole. The Rabi pulse with the calibrated phase ϕ actually makes a rotation, not exactly around the center of the spin-squeezed state, but around the projection of $\langle S \rangle$ on the xy -plane. To get a good estimation of the variance, we repeat the measurement for more than 100 times for each rotation angle θ to collect statistics. The measured variance $\text{Var}[S_\theta]$ varies with θ , reflecting the squeezed and anti-squeezed quadratures^[29].

Figure 5.4 shows such a tomography of a spin-squeezed state, with $N = 920 \pm 40$

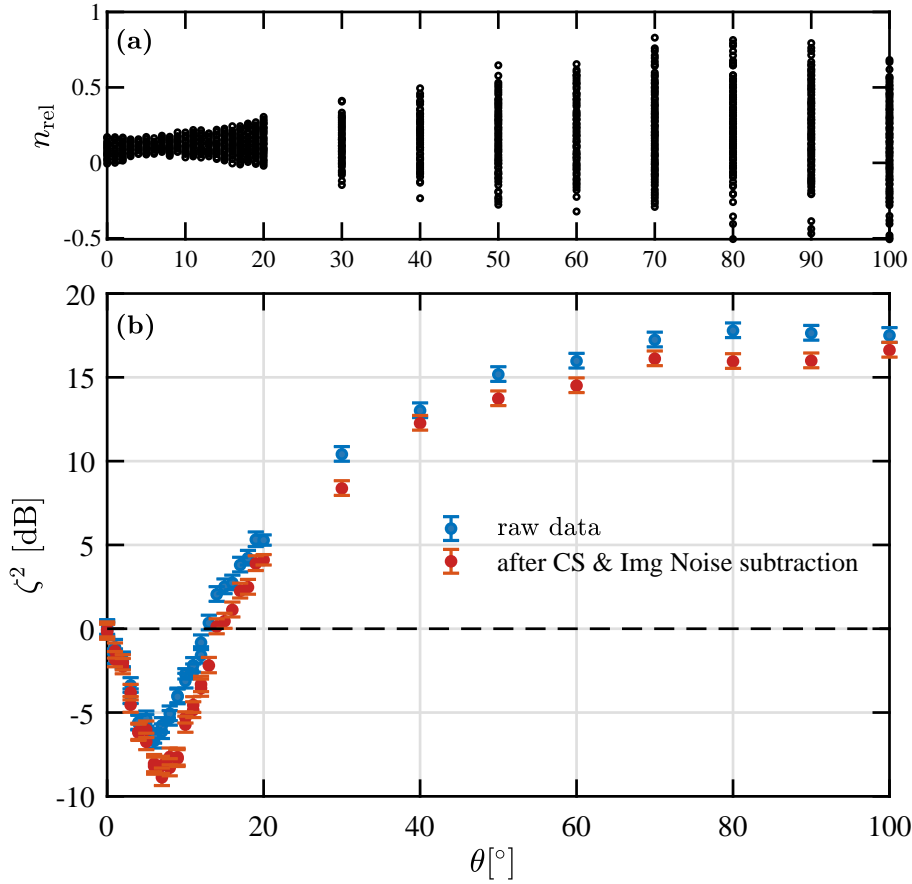


Figure 5.4 **Characterization of a spin-squeezed BEC.** **a)** Distribution of experimental measured n_{rel} for different rotation angles. Each black point corresponds to an individual spin projection measurement. **b)** The spin variance (calculated in terms of the number squeezing) as a function of rotating angle θ . The blue points are calculated with raw data, showing best squeezing to be at $\theta = 6^\circ$. Red points show data after the data processing, including the subtraction of contribution of the imaging noise (see text), and the clock-shift correction (see text in section 4.3.1.2). Error bars indicate statistical uncertainty based on the number of shots used for each data point. The processed data show a best squeezing $\zeta^2 = -8.8 \pm 0.4$ dB at $\theta = 8^\circ$. The Wineland spin-squeezing parameter for this dataset is of $\xi^2 = -7.9(4)$ dB. Data taken on 03.01.2019.

atoms. For different directions in the yz -plane, parametrized by the angle θ , Figure 5.4(a) shows the distribution of the experimental readout n_{rel} for different rotation angles. For each angle, the variance of the data distribution gives the number squeezing reported in Figure 5.4(b). For a turning angle of $\theta = 0^\circ$, the measured collective spin variance along the equator is consistent with projection noise of an ideal coherent spin state, with $\zeta^2 \approx 1$, which confirms that our imaging system is properly calibrated. The red data points show the post-processed data, where the effect of detection noise and the clock-shift noise have been subtracted. The noise subtraction corresponds to a -2.3 dB improvement compared to the raw data at the optimal squeezing angle. For θ from 0° to 14° , noise is observed to be lower than the SQL. The best number squeezing is reached at a turning angle of $\theta_0 = 6^\circ$ with the raw data, and at $\theta_0 = 8^\circ$ after the noise-subtraction. This observation indicates that the phase spreading along the equator effectively turns the state by a small angle. The anti-squeezed direction is at 90° from the optimal squeezed direction, and the measured noise is far above that of a coherent state, with $\zeta_{\text{anti}}^2 \approx 15.6$ dB. In the ideal case, the amount of noise reduction in the squeezed direction should exactly compensate the noise increase in the anti-squeezed direction. The observation of an imbalance, as in our case, indicates the presence of additional phase noise (for example, from sources discussed in chapter 4). The contrast, required to calculate the Wineland squeezing parameter, is obtained from an independent Ramsey measurement, where the state is rotated around the y axis. For this dataset we have $C = \langle S_x \rangle / (N/2) = 0.978 \pm 0.006$. The detection noise is calculated as $N\sigma_{n_{\text{rel}}}^2 = 0.0245$, corresponding to $\zeta_{\text{det}}^2 = -16$ dB, which is not subtracted when calculating the Wineland squeezing parameter. Therefore the metrologically useful squeezing is reduced from the $\zeta^2 = -8.8(4)$ dB to the Wineland squeezing parameter of $\xi^2 = -7.9(4)$ dB.

5.2.3 Entanglement in spin-squeezed states

It has been shown that there is a connection between spin-squeezing and entanglement^[136]; usually spin squeezing in the atomic ensemble reflects the entanglement between atoms. Therefore, apart from quantifying the metrological usefulness of a state, the Wineland squeezing parameter Eq. (5.4) can also be used to witness entanglement. Observing a Wineland parameter $\xi^2 < 1$ indicates the presence of non-classical correlations in a many-body system. Moreover, the entanglement depth can be inferred based on ξ^2 , following the approach Sørensen and Mølmer developed in Ref. [137]. The idea is based on the conclusion that, for entangled system constituting of k spins, there is a minimum

value that ξ^2 can approach. Therefore, reversing this argument, the observation of a given ξ^2 allows one to derive a lower bound on the depth of entanglement required to observe the given values of spin contrast and variance.

Here we need to clarify the definition of entanglement depth. Let us first consider a separable state. In a system of N spins (labelled as $l = 1, 2, \dots, N$), a pure quantum state is separable if it can be written as a product

$$|\Psi_{\text{sep}}\rangle = |\Psi^{(1)}\rangle \otimes |\Psi^{(2)}\rangle \otimes \dots \otimes |\Psi^{(N)}\rangle, \quad (5.6)$$

where $|\Psi^{(i)}\rangle$ is the state of the i th spin. A mixed state is separable if it can be written as a mixture of separable states^[138]

$$\hat{\rho}_{\text{sep}} = \sum_q p_q |\Psi_{\text{sep},q}\rangle \langle \Psi_{\text{sep},q}| \quad (5.7)$$

where q is the label of the pure state and the probabilities p_q satisfy the normalization $\sum_q p_q = 1$. In the case of $N = 2$ particles, any quantum state is either separable or entangled. For $N > 2$, we need further classifications. Multi-particle entanglement is quantified by the number of particles in the largest non-separable subset. In analogy with Eqs. (5.6) and (5.7) a k -separable state can be written as

$$|\Psi_{k \text{ sep}}\rangle = |\Psi_{N_1}\rangle \otimes |\Psi_{N_2}\rangle \otimes \dots \otimes |\Psi_{N_M}\rangle, \quad (5.8)$$

$$\hat{\rho}_{k \text{ sep}} = \sum_q p_q |\Psi_{k \text{ sep},q}\rangle \langle \Psi_{k \text{ sep},q}| \quad (5.9)$$

where the Eqs. (5.8) and (5.9) describe the pure state and mixed state, respectively. Here $|\Psi_{N_l}\rangle$ is a state of $N_l \leq k$ particles where $\sum_{l=1}^M N_l = N$. A state that is k separable but not $k - 1$ separable is called k -particle entangled: it contains at least one state of k particles that cannot be factorized. Such a state has an entanglement depth larger than $k - 1$ ^[136]. Also, k -separable states form a convex set containing the set of k' -separable states with $k' < k$ ^[139].

Figure 5.5 shows the quantified depth of entanglement for the data presented in the previous tomography Figure 5.4. The red lines illustrate the smallest variance attainable in a k -partite entangled state for a given Ramsey contrast, and they have been generated from a numerical minimisation of $\mu \langle \hat{S}_x \rangle + \langle \hat{S}_z^2 \rangle$ ^[137], detailed discussion can be found in Appendix B. The black data point represent our spin-squeezed state, which falls below the curve of spin variance calculated for $k = 128$, indicating an entanglement depth of at least 128.

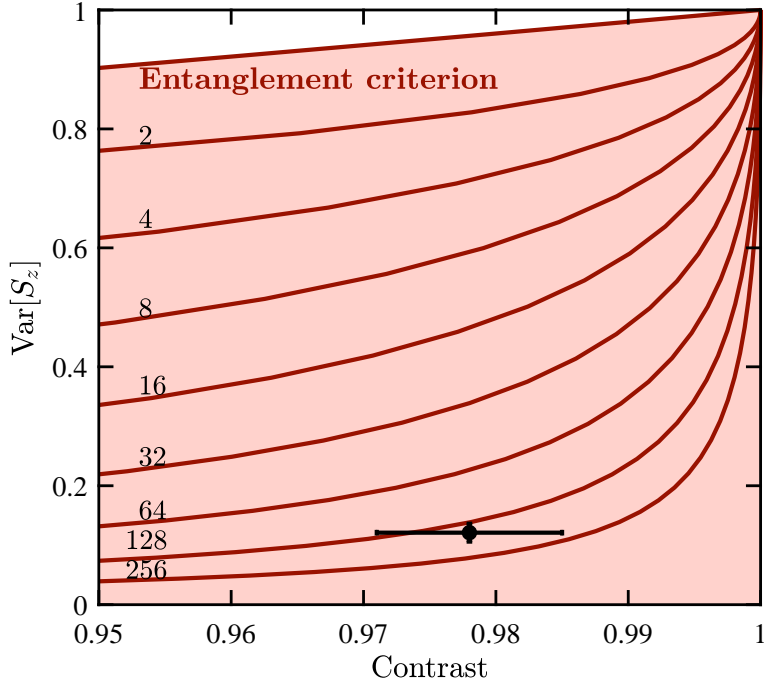


Figure 5.5 **Depth of entanglement in a spin-squeezed BEC.** Depth of entanglement calculated according to Ref. [137]. The red lines correspond to k -particle entanglement for $k = 2, 4, 8, \dots, 256$. The black data point corresponds to the squeezed states with $N = 920 \pm 40$ atoms of Figure 5.4, and it falls on the line for $k \approx 128$.

5.3 Exploration towards better spin squeezing

It is critical for future work of multi-partite entanglement experiment to improve the spin-squeezing. Several experimental improvements were made, as explained one by one in this section.

5.3.1 Microwave potential configurations

There are several experimental parameters that determine the microwave potential. From Eq. (3.20), the differential microwave potential is given by

$$V_{\text{mw}}^{|1,-1\rangle}(\mathbf{r}) - V_{\text{mw}}^{|2,1\rangle}(\mathbf{r}) = \frac{\hbar}{4} \sum_{m_2=-2}^0 \frac{|\Omega_{1,-1}^{2,m_2}(\mathbf{r})|^2}{\Delta_{1,-1}^{2,m_2}(\mathbf{r})} + \frac{\hbar}{4} \sum_{m_1=0}^1 \frac{|\Omega_{1,m_1}^{2,1}(\mathbf{r})|^2}{\Delta_{1,m_1}^{2,1}(\mathbf{r})}, \quad (5.10)$$

where the Rabi frequencies $|\Omega_{1,-1}^{2,m_2}(\mathbf{r})|$ and $|\Omega_{1,m_1}^{2,1}(\mathbf{r})|$ depend on the amplitude of the microwave field. It is shown that the differential microwave potential scales linearly with the power of the field and reversely with the microwave detuning, both of which can be easily controlled experimentally.

The amplitude of the microwave current determines the near-field microwave gradients which displaces the trap minima for the two spin components. By applying a larger

microwave current to the on-chip coplanar waveguide, one can increase the separation of the spatial modes of the two spin states to gain a larger χ . However, the capability of the chip wire to carry microwave current is limited (as one does not want to burn the wire). Another knob to turn is the detuning of the microwave field, Δ_0 , with reference to the $|1, 0\rangle \rightarrow |2, 0\rangle$ transition. In our experiment we usually use a blue-detuned field.

The splitting distance between two trap minima can be predicted with a simulation based on the ‘atom-chip toolbox’, which contains a numerical model of the wire patterns on the chip. This code, based on MATLAB, was originally developed in^[3], and allows us to simulate accurately the static and state-dependent magnetic potentials resulting from the DC and MW currents. In Figure 5.6, we plot the simulated Δx_0 for different settings of microwave parameters with a two-dimensional image, where the color indicates the splitting distance. Based on the predicted splitting distance, further simulation with a stationary 2CGPE can be used to predict the overlap between the atomic densities of the two states, which determines the strength of the one-axis twisting. The overlap between two wave functions does not depend on Δx_0 linearly due to the miscibility of Rb atoms, as one can see in Figure 5.7(b). In our experiment, we used to apply a microwaves current of $I_{\text{mw}} = 21$ mA, with frequency blue detuned by $\Delta_0 = 12$ MHz, which allowed us to split the two trap minima by 140 nm. Reducing the detuning to 10 MHz and increasing the current to 30 mA can lead to a twice smaller overlap between the atomic densities, and result in a stronger one-axis twisting with a gain in the non-linearity χ by a factor of up to 2000.

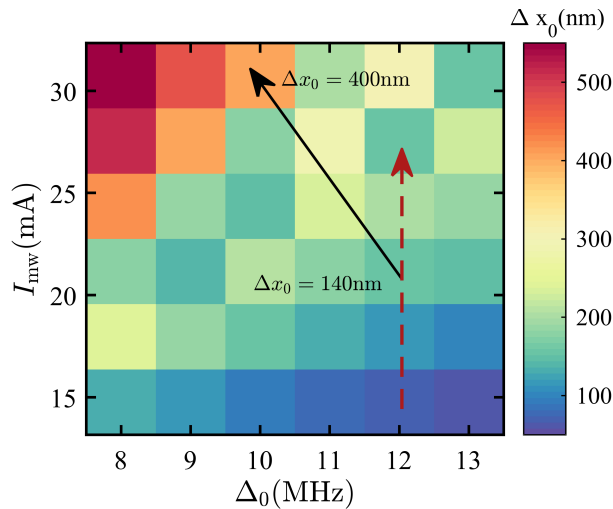


Figure 5.6 **Splitting distance for different Microwave configurations.** The simulated displacement between two trap minima Δx_0 is plotted as a function of the microwave current and the detuning. The old parameters and new parameters are indicated with a black arrow. The red dashed arrow indicates the parameters tested experimentally, as shown in Figure 5.8.

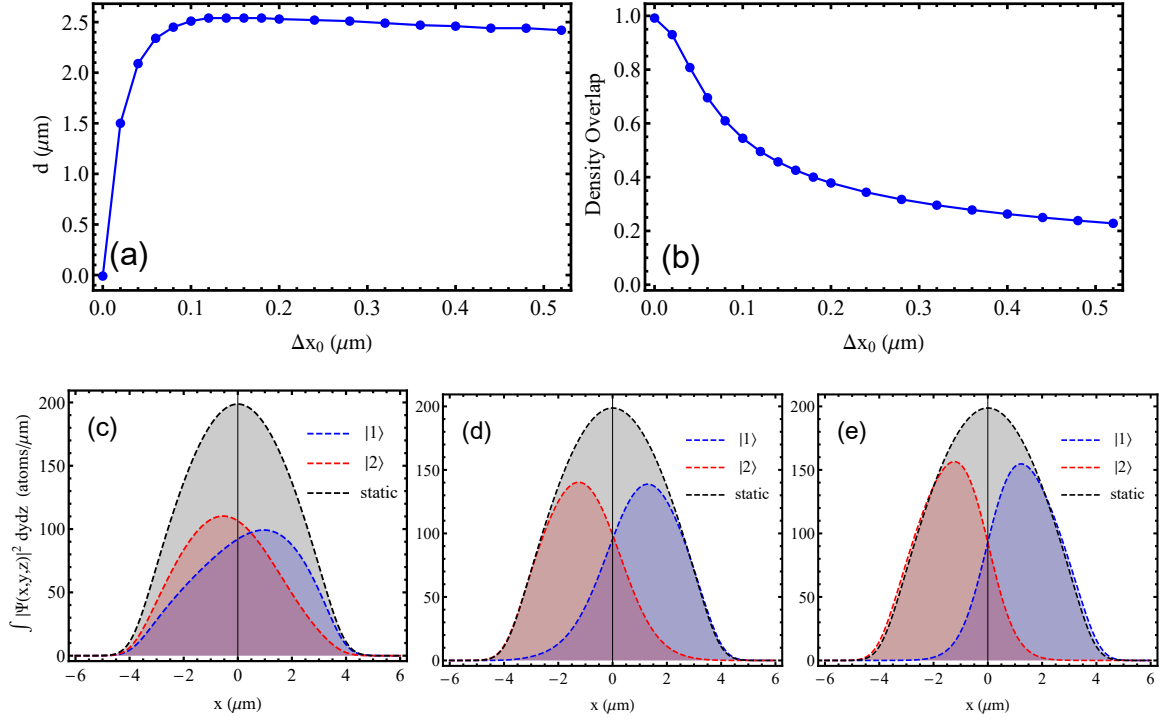


Figure 5.7 **Different splitting cases.** (a) The simulated in situ distance between wave functions of two states d as a function of Δx_0 . (b) The simulated density overlap between wave functions of two states $\int |\phi_1|^2 |\phi_2|^2 d\mathbf{r} / \sqrt{\int |\phi_1|^4 d\mathbf{r} \int |\phi_2|^4 d\mathbf{r}}$ (normalized to 1), as a function of Δx_0 . The wave functions are simulated by solving stationary 2CGPE, assuming 500 atoms in each state. The bottom panels show the density profiles along the splitting direction, in three different cases (assuming $\Delta_0 = 12$ MHz): (c) $I_{\text{mw}} = 15$ mA, $\Delta x_0 = 66$ nm; (d) $I_{\text{mw}} = 21$ mA, $\Delta x_0 = 140$ nm; (e) $I_{\text{mw}} = 30$ mA, $\Delta x_0 = 400$ nm.

In order to confirm the prediction of the simulation, we experimentally measure the spin demixing-remixing dynamics with a Ramsey sequence, as described before, for varying microwave current I_{mw} . As verified in Figure 5.8, where the slow oscillation reflects the state wave function splitting and combination, the contrast at the demixing instant becomes smaller for larger current, indicating a smaller overlap between the wave functions for the two states. In addition to a larger splitting, stronger field also has the advantage of a faster demixing-remixing dynamics. As discussed in section 5.1.3, the effective collisional interaction potential is proportional to the density overlap between the two states, and contributes negatively to the oscillation frequency of the demixing-remixing dynamics. Therefore, a larger spatial splitting of the two states also causes a faster demixing-remixing dynamics, which is clearly indicated in Figure 5.8 by the period of the modulation. Increasing the current from $I_{\text{mw}} = 17$ mA to $I_{\text{mw}} = 24$ mA causes the first revival time $T_{1\text{st}}$ to be earlier by ≈ 13.5 ms. The fact that the microwave potential is needed for a shorter time would also benefit the preparation of the spin-squeezed states, since the potential technical noise caused by the amplitude and the frequency fluctuations of the

microwave field would be reduced.

As a conclusion, in the previous experiments we used microwave blue detuned by $\Delta_0 = 12$ MHz, and applied a microwave current amplitude of $I_{\text{mw}} = 21$ mA, which allowed us to split the two trap minima by 140 nm, and thereby to increase χ by a factor of 10^3 . Recently, we have further optimized the configuration of the microwave field: we decreased the detuning to $\Delta_0 = 10$ MHz and increased the microwave current amplitude to 30 mA, which allows us to split the potential minima for the two states by 400 nm. This allows a gain in the non-linearity χ by a factor of up to 2000. In addition, the new configuration of the state-dependent potential yields faster splitting and recombination, leading to a shorter squeezing time with $T_s = T_{2nd} = 33.6$ ms. The new parameters allow us to obtain a gain in spin-squeezing by ≈ -2 dB compared to the old settings. The best squeezing with the old parameters was $\xi^2 = -6.8(4)$ dB^[105], whereas with the new microwave parameters we have achieved spin squeezing below -8 dB reproducibly, as can be seen in Table 5.2.

5.3.2 Relaxed trapping potential

With the new parameters, the preparation of a spin-squeezed state still takes a time duration of $t_{2nd} \approx 33.6$ ms, during which the phase fluctuations described in chapter 4 will emerge and harm the spin-squeezing, not only in terms of quadrature-specific spin noise along the optimal angle, but also of the overall fidelity for the state. In chapter 4, we have learned that the phase noise originates from the random collision between atoms and can be largely reduced by decreasing the collisional rates in a relaxed trap. However, a relaxed trap has a major drawback that the reduced atomic density results in weaker one-axis twisting dynamics due to the density dependence of the strength of the non-linearity χ . This can be confirmed by numerically computing χ with a time-dependent 2CGPE simulation: as plotted in Figure 5.9, $\chi(t)$ for a relaxed trap is smaller than for a standard trap. Note that due to the spin demixing-remixing dynamics, χ is time-dependent and shows a periodic oscillation.

Therefore, relaxing the trap is beneficial when considering the phase noise, but can have drawbacks. Different effects compete with each other, which makes it complicated to evaluate the gain and loss theoretically. To find out whether the relaxed trap helps, in the recent experiments we implemented a trap with trapping frequency of $(\omega_x, \omega_y, \omega_z) = 2\pi \times (113, 301, 301)$ Hz and compared the results with the previously used trap with $(\omega_x, \omega_y, \omega_z) = 2\pi \times (114, 714, 714)$ Hz. The results of spin squeezing in the two

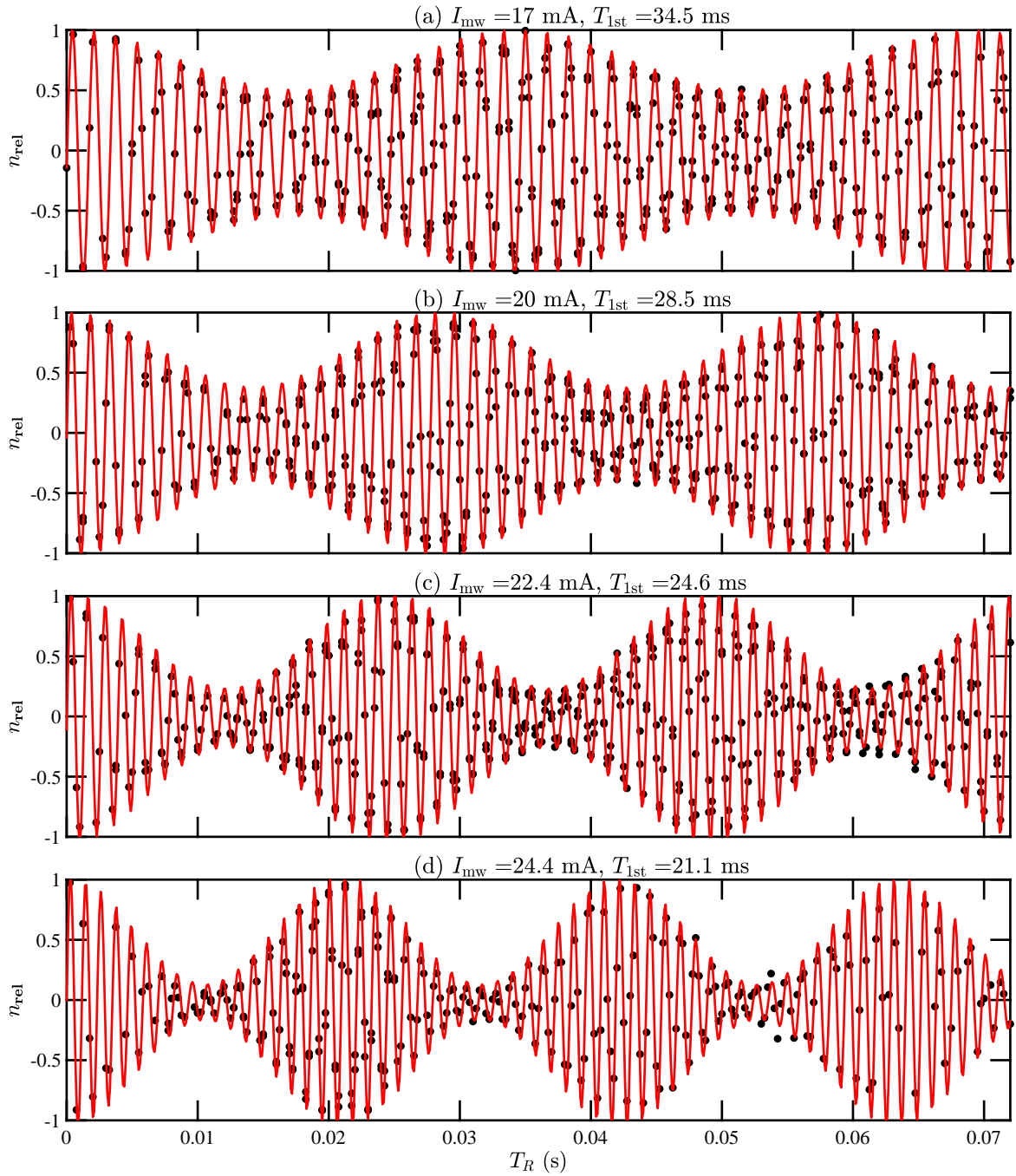


Figure 5.8 **Demixing-remixing dynamics for different Microwave current.** The measured Ramsey fringes as a function of the interrogation time T_R , for different microwave current. The microwave detuning is fixed at $\Delta_0 = 12 \text{ MHz}$. The atom number is 1000 ± 100 for all measurements in this figure. Measurements are performed in a trap with $(\omega_x, \omega_y, \omega_z) = 2\pi \times (114, 714, 714)$. Data taken on 25.12.2018.

traps are given in Table 5.1. Although the measured spin noise along the squeezed direction is similar in both traps, the spin noise along the anti-squeezed quadrature reflects the advantage of the shallow trap: $\zeta_{\text{anti}}^2 = 14.2$ dB in the shallow trap, which is 2.2 dB better than the tight trap, indicates a reduced overall noise of the quantum state. This advantage is not that much evident when we only consider the application of the spin-squeezed state in interferometric measurements, but it is very important when it comes to the observation of entanglement between atoms (for example, when measuring the witness of an Einstein-Podolsky-Rosen entanglement, as mentioned in section 6.2.2), since the spin noise along the anti-squeezed direction will also contribute to the criteria or witness.

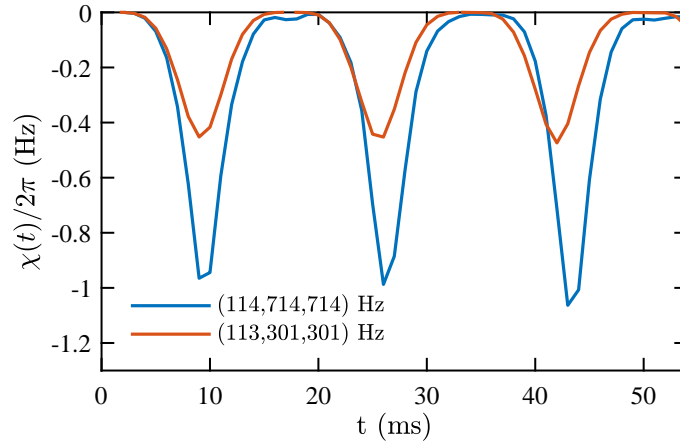


Figure 5.9 **Time-dependent non-linearity.** The simulated time-dependent parameter $\chi/2\pi$ as a function of the time t , for traps with $(\omega_x, \omega_y, \omega_z) = 2\pi \times (114, 714, 714)$ Hz (blue) and $(\omega_x, \omega_y, \omega_z) = 2\pi \times (113, 301, 301)$ Hz (red). The simulation assumes the splitting between trap minima is 400 nm and an initial state with 500 atoms in each spin state.

Table 5.1 **Comparison of the spin squeezing in two traps.** Measurement of our spin-squeezed state in two traps, characterized by the mean atom number $\langle N \rangle$, the number squeezing along the squeezed quadrature θ_0 (dB) and the anti-squeezing quadrature $\theta_0 + \pi/2$.

Trap frequency	$\langle N \rangle$	$\zeta_{\theta_0}^2$ (dB)	$\zeta_{\theta_0 + \pi/2}^2$ (dB)
$2\pi \times (114, 714, 714)$ Hz	870 ± 47	-8.7 ± 0.5	16.4 ± 0.4
$2\pi \times (113, 301, 301)$ Hz	900 ± 42	-9.1 ± 0.5	14.2 ± 0.4

5.3.3 Spin-Echo technique

During the preparation of spin squeezing, the system suffers from the technical noise and intrinsic noise, both harm the spin squeezing. To protect the state from the uncontrolled shot-to-shot phase fluctuations (for example the fluctuating microwave potential or fluctuating collisional interactions), Spin-Echo technique can be applied. The sequence is different from the normal preparation sequence, as visualized in Figure 5.10. A π Rabi

pulse (spin-echo pulse) is applied in the middle of the state-dependent potential. Usually, we turn on the state-selective potential for two periods of the splitting and recombination $T_{2\text{nd}} \approx 2T_{1\text{st}}$, and this π -pulse is applied at the first revival time $T_{1\text{st}}$ so that the sequence is symmetric. The spin echo pulse effectively swaps the internal states of atoms, and in the subsequent evolution, the phase shift caused by the collisional clock shift will be partly compensated for. Moreover, the offset of n_{rel} caused by asymmetric losses of the two states is also compensated, resulting in a state closer to the equator, compared to a state that is evolved without the spin echo pulse. With this protocol, we observe a spin-squeezed state similar to the typical state prepared without the echo pulse, but less noisy along the anti-squeezed direction by around 1 dB, which confirms that with the spin-echo pulse the state preparation is less sensitive to phase fluctuations.

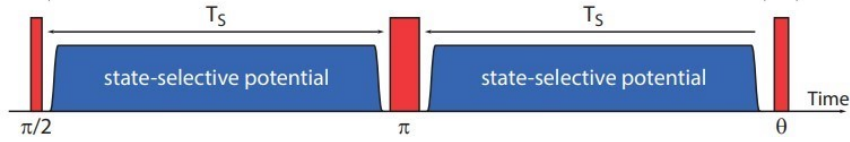


Figure 5.10 **Sequence to prepare a spin-squeezed state with spin echo technique.** The figure shows Rabi pulses (red) and on-chip microwave pulses (blue). The duration of the Rabi pulses are exaggerated for visualization, in fact it is on the order of a few hundreds of microseconds, much shorter than T_s .

5.3.4 Atom number stability

There are several other improvements that contribute to the better spin squeezing. The most important one is that we have improved *the stability of the atom number*, by updating the optics system of the set up and implementing the stabilization of laser intensity of the cooling light. This way we achieved an atom number more stable than before with $\Delta N = 40$. The shot-to-shot noise due to the atom number dependent phase fluctuation is thus largely reduced.

Experimentally, improvement are also made by implementing a longer imaging pulse of $150 \mu\text{s}$, three times longer than before. The detection noise, contributed mainly by the photon shot noise, is then reduced from 5×10^{-3} to 3×10^{-3} .

5.3.5 Summary

To compare the improved spin-squeezing with the previous experiments, we summarize the characterization of spin-squeezed states taken on different days in Table 5.2 before and after changes were implemented to the experiment. Each measurement is taken with

more than 100 shots per measurement, which provides enough statistics to determine the variance for a distribution. We summarize the mean atom number $\langle N \rangle$, the contrast C , and the squeezing parameters ζ^2 and ξ^2 . Due to the different chosen parameters, the optimal angle θ_0 are different and determined independently. Listed uncertainties are the fit uncertainty for C , statistical uncertainty for ζ^2 and ξ^2 .

With the new microwave parameters and other improvements mentioned above, we have achieved a best spin squeezed state measured with $\xi^2 = -9.8(5)$ dB and reproducibly measure spin squeezing at about -8 dB. The significantly improved and more reliable spin squeezing in the system finally allow us to perform a Ramsey interferometer beyond SQL, as discussed in next section, and also lead us to further experiments measuring the entanglement between two spatially separated BECs, as mentioned in the outlook part, section 6.2.2.

Table 5.2 Comparison of the spin-squeezed state on different times. Measurement of our spin-squeezed state on different days, characterized by the mean atom number $\langle N \rangle$, the contrast C and the squeezing factor ξ^2 . The settings listed are the microwave current I_{mw} , detuning Δ_0 , and if spin echo technique is applied. The dataset with mark was performed previously by my colleagues.

Dataset	$\langle N \rangle$	C (%)	ζ^2 (dB)	ξ^2 (dB)	$(\omega_x, \omega_y, \omega_z)/2\pi$	setting
16-12-2011*	1429	98.4(6)	-4.8(5)	-4.3(4)	(114, 714, 714)	15 mA, 12 MHz, no spin echo
02-10-2015*	580	97.1(8)	-7.0(4)	-6.8(3)	(114, 714, 714)	21 mA, 12 MHz, no spin echo
01-01-2019	940	95.9(8)	-8.3(4)	-7.5(3)	(114, 714, 714)	24.4 mA, 12 MHz, no spin echo
03-01-2019	920	97.8(6)	-8.8(4)	-7.9(4)	(114, 714, 714)	30 mA, 12 MHz, no spin echo
04-03-2020	840	97.1(3)	-10.4(5)	-9.8(5)	(113, 301, 301)	30 mA, 12 MHz, with spin echo
18-03-2020	920	96.1(3)	-9.0(5)	-8.2(5)	(113, 301, 301)	30 mA, 10 MHz, no spin echo
12-11-2020	900	96.5(3)	-9.1(5)	-8.4(5)	(113, 301, 301)	30 mA, 10 MHz, with spin echo

5.4 Non-classical interferometer with a spin-squeezed state

With the improved spin squeezing, we are able to implement the non-classical interferometer with a phase precision beyond SQL. The experimental sequence contain several stages: first we prepare the spin-squeezed state as previously described; after the preparation of spin-squeezed state, it will be rotated by an angle around its center, to align the squeezed quadrature perpendicular with the equator, so that the state is most insensitive to the phase noises; then we wait for an interrogation time T_R before the final $\pi/2$ Rabi pulse is applied to read out the accumulated phase. In order to investigate the temporal

behavior of the precision, we perform such sequence with varying T_R and record the phase sensitivity. Figure. 5.11 shows the result of such a non-classical interferometer and the result of a classical interferometer performed with a coherent spin state as a comparison.

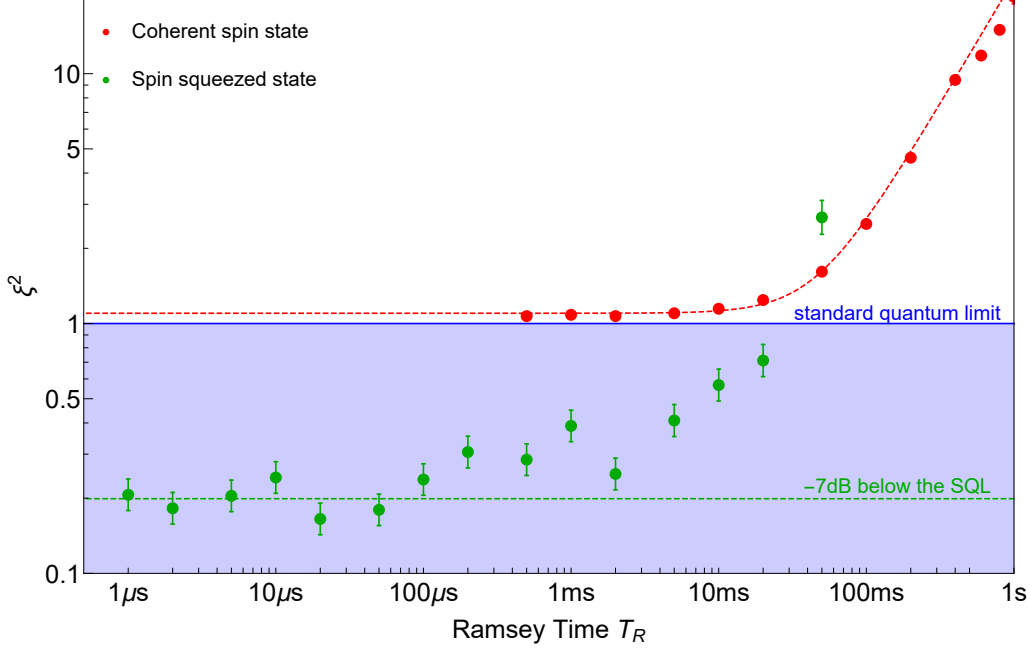


Figure 5.11 **Phase uncertainty of non-classical and classical interferometer.** The measured phase uncertainty (Wineland spin squeezing parameter) as a function of the interrogation time T_R , for interferometers with a spin-squeezed state (green data points) and coherent spin state (red data points) as input. The trapping frequency is $2\pi \times (114, 714, 714)$ Hz, atom number are all 1000 ± 100 . Data taken on 21.01.2019.

At a short time, the advantage of the non-classical state is evident, as one can see from the Wineland squeezing parameter, showing an interferometric sensitivity 7dB beyond the SQL. Compared with previous experiment performed in this set up in which a sensitivity of 4.0 dB beyond SQL^[19], it is significantly improved. The Wineland squeezing parameter of the classical interferometer is at 1, as one would expect. When the interrogation time gets longer, the effect of decoherence emerges, and the phase sensitivity gradually gets worse. The coherence time of a spin-squeezed state is at the same magnitude with the coherent spin state, at several tens of milliseconds. This result again confirms that the previously discussed fundamental limit of the phase coherence poses a limit of phase sensitivity on both of the classical and non-classical state interferometers.

CHAPTER 6 CONCLUSIONS AND OUTLOOKS

6.1 Conclusions

In this thesis, we have investigated the internal state interferometer based on ultracold ^{87}Rb atoms from two aspects: the phase coherence property and the spin-squeezing in the system.

In the first series of experiments, we measure precisely the growth of the phase noise in a trapped two-component BEC and identify the main decoherence sources. We demonstrate that the coherence is limited by random collisional phase shifts due to the stochastic nature of atom loss. A theoretical model is built to describe this decoherence mechanism and numerical simulation is performed based on a Monte-Carlo wave function method. The simulated result shows a good agreement with the experiment. This is the first experimental observation of decoherence caused by homogeneous effects arising within the many-body system itself. Moreover, it poses a fundamental limit since all neutral atomic gases have particle losses in common (in particular, three-body collisions are unavoidable due to the chemical metastability of BECs). In addition, the good agreement between experimental data and the 2CGPE simulation also allows us to extract the two-body loss constants. Our findings are relevant for experiments on many-particle entanglement and quantum metrology^[7] as well as trapped-atom clocks and interferometers where the atomic interactions play important roles^[26].

In the second series of experiments, we explore and improve the spin squeezing in our system. Several strategies, including optimizing the configurations of microwave state-dependent potential, relaxing the static trapping potential and implementing the spin echo pulse, allow us to achieve a spin-squeezed state with Wineland spin-squeezing parameter $\xi^2 = -9.8(5)$ dB, significantly improved compared to previous results in our experiment. The improvement of the spin squeezing finally allows us to demonstrate an entanglement-enhanced atom interferometry beyond the SQL by 7 dB. And we show that the fundamental limit of the phase coherence also exists for the non-classical interferometer. The improvement of spin squeezing is not only important for improving measurement precision of internal interferometry, but also provide the potential of exploring many-body entanglements such as the Einstein-Podolsky-Rosen (EPR) entanglement in ultracold atomic ensembles.

6.2 Outlook

In this section, we discuss further experiments that could be performed with our experimental setup in the near future. We also briefly present a few initial results of current experimental progress, which is carried out by our team at the time of this writing, but not completed or published yet.

6.2.1 Control of the phase coherence with state-dependent potential

Following the study of the phase coherence in the two-component BEC in chapter 4, naturally one will think about eliminating the decoherence caused by the atom number dependent rotation term $\tilde{\chi} \hat{N} \hat{S}_z$ in the Hamiltonian Eq. (2.27). One possible way to realize this is to minimize the parameter $\tilde{\chi}$ by engineering the intra-species atomic interactions with state-dependent traps. It is worth mentioning that, the state-dependent trap used in this scenario is slightly different from the one we use to engineer χ , as discussed in section 5.1.1, where the trapping potentials for two states are split in order to increase χ . Here, in order to minimize $\tilde{\chi}$, one needs to relax the trapping potential for state $|1\rangle$ while keeping the trap frequency for $|2\rangle$ fixed, thus to modulate the atomic density in only one internal state. In this way, the intra-species collision energy in state $|1\rangle$ can be artificially tuned to compensate that of state $|2\rangle$, so that $\tilde{\chi}$ is cancelled. A schematic of the state-dependent trap in this scenario is shown in Figure 6.1.

One problem we meet is that, the one-axis twisting term will also be amplified since the wave function overlap between two internal states is reduced, although not as dramatically as in chapter 5. In fact, in a test experiment, we have observed an increased phase noise due to the phase diffusion along the anti-squeezed quadrature, with a quantified spin squeezing with $\zeta^2 \approx 3$ dB. Therefore further investigations are needed before the realization of this proposal.

The ability to tune the interaction energies will allow us to minimize $\tilde{\chi}$ so that the quantum state is protected from the decoherence induced by two-body losses, as proposed in^[131]. In this way, we can further mitigate the dominant term of the phase noise and hopefully can reach the fundamental bound of precision limit in quantum metrology as theoretically described in^[129-130].

Interestingly, this technique can also be helpful to create highly entangled states beyond spin squeezed states, or even towards Schrödinger cat states, which are never observed in our experiment before. The highly entangled states are fragile against the atom

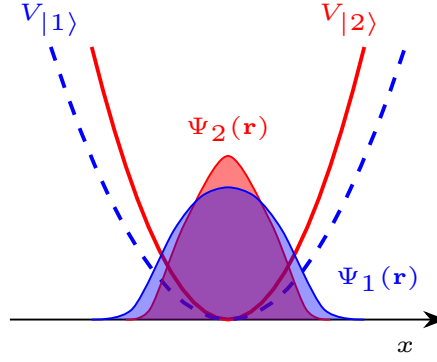


Figure 6.1 **State-dependent trap to tune $\tilde{\chi}$.** We implement the near-field microwave gradient so that the trap frequency of state $|2\rangle$ is fixed while trap for state $|1\rangle$ is relaxed. This way the self interactions of the two states can be artificially tuned and balanced.

losses due to the phase dependence of atom number, and will benefit from minimizing the density-dependent term $\tilde{\chi}\hat{S}_z$ in the full Hamiltonian Eq. (2.27). Therefore the ability to tune the parameter $\tilde{\chi}$ is probably a critical step towards Schrödinger cat states.

6.2.2 EPR entanglement between two spatially separated BECs

An ongoing work of our experiment is to demonstrate entanglement between two spatially separated BECs. In our group, results obtained so far include spin-squeezing and many-particle entanglement^[29], the observation of Bell correlations in a BEC^[109], and entanglement between different spatial regions of the same cloud^[104]. However, these entanglement measurements only concerned atoms in a single cloud, while entanglement between two spatially separated BECs that are individually addressable has not yet been observed. Such a system offers the possibility to perform local manipulations and measurements on each BEC and to study the nonlocal quantum correlations between them, such as the Einstein-Podolsky-Rosen (EPR) steering^[27].

If two spin systems A and B are entangled strongly enough, the measurement outcome of A can be used to predict the measurement result of a non-commuting observable in system B. Therefore for system B, an observer predict the outcome of two orthogonal, non-commuting spin measurements, with a product of the inferred spin variances below the Heisenberg uncertainty bound. EPR steering requires entanglement, whereas entanglement is not sufficient for EPR steering. The EPR steering criterion takes the form^[105]

$$E_{\text{EPR}}^{A \rightarrow B} = \frac{4\text{Var}(g_z\hat{S}_z^A + \hat{S}_z^B)\text{Var}(g_y\hat{S}_y^A + \hat{S}_y^B)}{|\langle \hat{S}_x^B \rangle|^2} < 1, \quad (6.1)$$

$$E_{\text{EPR}}^{B \rightarrow A} = \frac{4\text{Var}(g_z\hat{S}_z^B + \hat{S}_z^A)\text{Var}(g_y\hat{S}_y^B + \hat{S}_y^A)}{|\langle \hat{S}_x^A \rangle|^2} < 1, \quad (6.2)$$

where $\hat{S}_i^A (i = x, y, z)$ are collective spin operators of system A , and similar for \hat{S}_i^B , g is a factor that can be manually chosen and optimized. EPR steering is relevant for quantum metrology because it allows one to perform collective spin measurements for two orthogonal, non-commuting components with a precision beyond the standard quantum limit at the same time. It can thus be used to sense small spin rotations with high precision.

EPR entanglement between two BECs can be generated by the sequence described in the following. We first create strong entanglement between atoms in one BEC, using the same technique as we have present in this thesis (discussed before in section 5.1.1). Now that we have improved the spin squeezing to a better level, the creation of strong entanglement is compatible with experimental capabilities. After the preparation of entanglement, we need to coherently split the BEC into two. One strategy is to drive Rabi transitions via microwave field so that atoms in state $|F = 1, m_F = -1\rangle$ is coupled to state $|F = 2, m_F = 0\rangle$ and atoms in state $|F = 2, m_F = 1\rangle$ is coupled to the state $|F = 1, m_F = 0\rangle$. Experimentally, microwave fields at the two needed transition frequencies can be applied at the same time to implement such an out-coupling procedure. The two new internal states are all magnetic untrappable states, the atoms will start falling due to the gravity immediately after being out-coupled. We denote the new cloud which is falling down as system B , and the states $|2, 0\rangle$ and $|1, 0\rangle$ as the spin component $|1\rangle_B$ and $|2\rangle_B$ of the new BEC system B . In this way, two independent BECs A and B are created, and both are prepared in an equal superposition of spin up and spin down.

Apart from pursuing the out-coupling in the experiment, a few additional ingredients are needed to measure entanglement between two BECs. One challenge is to individually address the two BECs with microwave and radio-frequency fields in order to perform high-fidelity coherent rotations of collective spin in one system without perturbing the other system, which is critical for performing measurements of different combinations of spin quadratures. In order to find $E_{\text{EPR}} < 1$, the orientation of the spin quadratures needs to be carefully calibrated, with the required angular resolution of spin rotations on the two BECs on the order of a few degrees. Besides, the atoms start dropping immediately after they are out coupled to the system B , which means the individual rotations of B can only be performed during the TOF. The spatial inhomogeneity of the microwave-field will therefore cause a spatial gradient in Rabi transition frequency, and makes the individual rotation of system B less efficient. This effect can be minimized by applying large microwave power to gain a quicker Rabi frequency. For the readout, state-selective imaging

of both states independently is straightforward to implement. A potential problem is that, in order to measure the EPR criteria for a large enough splitting, the duration of time-flight should be long enough, which in turn requires a large view range of the detection CCD. This problem can be tackled by installing a camera with a smaller magnification.

Our current work in this direction indicates that we can indeed realize entanglement and the stronger EPR steering between the two Bose-Einstein condensates. This realizes the famous gedanken experiment in a massive many body system. This work is still ongoing at the time of this writing and will be published in the near future elsewhere.

BIBLIOGRAPHY

- [1] The LIGO Scientific Collaboration. A gravitational wave observatory operating beyond the quantum shot-noise limit[J]. *Nature Phys.*, 2011, 7: 962-965.
- [2] Wynands R, Weyers S. Atomic fountain clocks[J]. *Metrologia*, 2005, 42: S64.
- [3] Treutlein P. Coherent manipulation of ultracold atoms on an atom chip[D/OL]. Ludwigs-Maximilians-Universität, München, 2008. <http://nbn-resolving.de/urn:nbn:de:bvb:19-91532>.
- [4] Reichel J, Vuletić V. Atom chips[M/OL]. Weinheim, Germany: Wiley-VCH, 2011. DOI: 10.1002/9783527633357.
- [5] Treutlein P, Hommelhoff P, Steinmetz T, et al. Coherence in microchip traps[J]. *Phys. Rev. Lett.*, 2004, 92: 203005.
- [6] Szmuk R, Dugrain V, Maineult W, et al. Stability of a trapped-atom clock on a chip[J/OL]. *Phys. Rev. A*, 2015, 92: 012106. <https://link.aps.org/doi/10.1103/PhysRevA.92.012106>.
- [7] Pezzè L, Smerzi A, Oberthaler M K, et al. Quantum metrology with nonclassical states of atomic ensembles[J]. *Rev. Mod. Phys.*, 2018, 90(3): 035005.
- [8] Ketterle W, Miesner H J. Coherence properties of bose-einstein condensates and atom lasers [J]. *Phys. Rev. A*, 1997, 56(4): 3291.
- [9] Wiseman H, Thomsen L. Reducing the linewidth of an atom laser by feedback[J]. *Phys. Rev. Lett.*, 2001, 86(7): 1143.
- [10] Li Y, Pawłowski K, Décamps B, et al. Fundamental limit of phase coherence in two-component bose-einstein condensates[J]. *Phys. Rev. Lett.*, 2020, 125(12): 123402.
- [11] Wineland D J, Bollinger J J, Itano W M, et al. Squeezed atomic states and projection noise in spectroscopy[J]. *Phys. Rev. A*, 1994, 50(1): 67-88.
- [12] Walther P, Pan J W, Aspelmeyer M, et al. De broglie wavelength of a non-local four-photon state[J]. *Nature*, 2004, 429(6988): 158-161.
- [13] Mitchell M W, Lundeen J S, Steinberg A M. Super-resolving phase measurements with a multiphoton entangled state[J]. *Nature*, 2004, 429(6988): 161-164.
- [14] Sackett C A, Kielpinski D, King B E, et al. Experimental entanglement of four particles[J]. *Nature*, 2000, 404(6775): 256-259.
- [15] Leibfried D, Barrett M D, Schaetz T, et al. Toward heisenberg-limited spectroscopy with multiparticle entangled states[J]. *Science*, 2004, 304(5676): 1476-1478.
- [16] Giovannetti V, Lloyd S, Maccone L. Quantum metrology[J/OL]. *Phys. Rev. Lett.*, 2006, 96: 010401. <https://link.aps.org/doi/10.1103/PhysRevLett.96.010401>.
- [17] Gross C, Zibold T, Nicklas E, et al. Nonlinear atom interferometer surpasses classical precision limit[J/OL]. *Nature*, 2010, 464(7292): 1165. DOI: 10.1038/nature08919.
- [18] Giovannetti V, Lloyd S, Maccone L. Advances in quantum metrology[J/OL]. *Nature Photon.*, 2011, 5(4): 222. DOI: 10.1038/nphoton.2011.35.

BIBLIOGRAPHY

- [19] Ockeloen C F, Schmied R, Riedel M F, et al. Quantum metrology with a scanning probe atom interferometer[J/OL]. *Phys. Rev. Lett.*, 2013, 111(14): 143001. DOI: 10.1103/PhysRevLett.111.143001.
- [20] Kitagawa M, Ueda M. Squeezed spin states[J/OL]. *Phys. Rev. A*, 1993, 47: 5138-5143. <http://link.aps.org/doi/10.1103/PhysRevA.47.5138>.
- [21] Appel J, Windpassinger P J, Oblak D, et al. Mesoscopic atomic entanglement for precision measurements beyond the standard quantum limit[J]. *Proceedings of the National Academy of Sciences*, 2009, 106(27): 10960-10965.
- [22] Louchet-Chauvet A, Appel J, Renema J J, et al. Entanglement-assisted atomic clock beyond the projection noise limit[J]. *New J. Phys.*, 2010, 12(6): 065032.
- [23] Leroux I, Schleier-Smith M, Vuletić V. Orientation-dependent entanglement lifetime in a squeezed atomic clock[J/OL]. *Phys. Rev. Lett.*, 2010, 104(25): 250801. DOI: 10.1103/PhysRevLett.104.250801.
- [24] Leroux I D, Schleier-Smith M H, Vuletić V. Implementation of cavity squeezing of a collective atomic spin[J/OL]. *Phys. Rev. Lett.*, 2010, 104(7): 073602. DOI: 10.1103/PhysRevLett.104.073602.
- [25] Mainault W, Deutsch C, Gibble K, et al. Spin waves and collisional frequency shifts of a trapped-atom clock[J]. *Phys. Rev. Lett.*, 2012, 109(2): 020407.
- [26] Laudat T, Dugrain V, Mazzoni T, et al. Spontaneous spin squeezing in a rubidium bec[J]. *New J. Phys.*, 2018, 20(7): 073018.
- [27] Wiseman H M, Jones S J, Doherty A C. Steering, entanglement, nonlocality, and the einstein-podolsky-rosen paradox[J/OL]. *Phys. Rev. Lett.*, 2007, 98: 140402. <https://link.aps.org/doi/10.1103/PhysRevLett.98.140402>.
- [28] Sørensen A S. Bogoliubov theory of entanglement in a Bose-Einstein condensate[J/OL]. *Phys. Rev. A*, 2002, 65(4): 043610. DOI: 10.1103/PhysRevA.65.043610.
- [29] Riedel M F, Böhi P, Li Y, et al. Atom-chip-based generation of entanglement for quantum metrology[J/OL]. *Nature*, 2010, 464: 1170-1173. DOI: 10.1038/nature08988.
- [30] Einstein A. Quantentheorie des einatomigen idealen Gases. Zweite Abhandlung[J]. *Sitzung der physikalisch-mathematischen Klasse vom 8. Januar, 1925*.
- [31] Anderson M H, Ensher J R, Matthews M R, et al. Observation of Bose-Einstein condensation in a dilute atomic vapor[J/OL]. *Science*, 1995, 269: 198-201. DOI: 10.1126/science.269.5221.198.
- [32] Davis K B, Mewes M O, Andrews M R, et al. Bose-Einstein condensation in a gas of sodium atoms[J]. *Phys. Rev. Lett.*, 1995, 75: 3969-3973.
- [33] Bradley C C, Sackett C A, Tollett J J, et al. Evidence of Bose-Einstein condensation in an atomic gas with attractive interactions[J]. *Phys. Rev. Lett.*, 1995, 75: 1687-1690.
- [34] Metcalf H J, van der Straten P. *Laser cooling and trapping*[M/OL]. 1st ed. Springer-Verlag Berlin Heidelberg New York, 1999. DOI: 10.1007/978-1-4612-1470-0.
- [35] Metcalf H J, van der Straten P. *Laser cooling and trapping of atoms*[J/OL]. *Journal of the Optical Society of America B Optical Physics*, 2003, 20: 887-908. DOI: 10.1364/JOSAB.20.000887.

BIBLIOGRAPHY

- [36] Ketterle W, Druten N J V. Evaporative cooling of trapped atoms[J/OL]. *Advances in Atomic Molecular and Optical Physics*, 1996, 37: 181-236. DOI: 10.1016/S1049-250X(08)60101-9.
- [37] Myatt C, Burt E, Ghrist R, et al. Production of two overlapping bose-einstein condensates by sympathetic cooling[J]. *Phys. Rev. Lett.*, 1997, 78(4): 586.
- [38] Harber D M, Lewandowski H J, McGuirk J M, et al. Effect of cold collisions on spin coherence and resonance shifts in a magnetically trapped ultracold gas[J/OL]. *Phys. Rev. A*, 2002, 66: 053616. <https://link.aps.org/doi/10.1103/PhysRevA.66.053616>.
- [39] Hänsel W, Hommelhoff P, Hänsch T W, et al. Bose–einstein condensation on a microelectronic chip[J/OL]. *Nature*, 2001, 413: 498 EP -. <http://dx.doi.org/10.1038/35097032>.
- [40] Schumm T, Hofferberth S, Andersson L M, et al. Matter-wave interferometry in a double well on an atom chip[J]. *Nature Physics*, 2005, 1: 57 EP -.
- [41] Dalfovo F, Giorgini S, Pitaevskii L P, et al. Theory of Bose-Einstein condensation in trapped gases[J]. *Rev. Mod. Phys.*, 1999, 71: 463-512.
- [42] Leggett A J. Bose-Einstein condensation in the alkali gases: Some fundamental concepts[J]. *Rev. Mod. Phys.*, 2001, 73: 307-356.
- [43] Giorgini S, Pitaevskii L P, Stringari S. Condensate fraction and critical temperature of a trapped interacting bose gas[J]. *Phys. Rev. A*, 1996, 54: R4633-R4636.
- [44] Egorov M, Opanchuk B, Drummond P, et al. Measurement of *s*-wave scattering lengths in a two-component Bose-Einstein condensate[J]. *Phys. Rev. A*, 2013, 87: 053614.
- [45] Mertes K M, Merrill J W, Carretero-González R, et al. Nonequilibrium dynamics and superfluid ring excitations in binary bose-einstein condensates[J/OL]. *Phys. Rev. Lett.*, 2007, 99: 190402. <https://link.aps.org/doi/10.1103/PhysRevLett.99.190402>.
- [46] Sakurai J J, Napolitano J. *Modern quantum mechanics*[M]. 2nd ed. Cambridge University Press, 2017.
- [47] Yurke B, McCall S L, Klauder J R. SU(2) and SU(1,1) interferometers[J]. *Phys. Rev. A*, 1986, 33: 4033-4054.
- [48] Raghavan S, Pu H, Meystre P, et al. Generation of arbitrary Dicke states in spinor Bose-Einstein condensates[J/OL]. *Optics Communications*, 2001, 188: 149-154. DOI: 10.1016/S0030-4018(00)01163-9.
- [49] Li Y, Treutlein P, Reichel J, et al. Spin squeezing in a bimodal condensate: spatial dynamics and particle losses[J]. *European Physical Journal B*, 2009, 68: 365-381.
- [50] Ockeloen C F. *Quantum metrology with a scanning probe atom interferometer*[D]. University of Basel, 2014.
- [51] Wigner E. On the quantum correction for thermodynamic equilibrium[J]. *Phys. Rev.*, 1932, 40: 749-759.
- [52] Husimi K. Some formal properties of the density matrix[J]. *Proceedings of the Physico-Mathematical Society of Japan. 3rd Series*, 1940, 22(4): 264-314.
- [53] Dowling J P, Agarwal G S, Schleich W P. Wigner distribution of a general angular-momentum state: Applications to a collection of two-level atoms[J/OL]. *Phys. Rev. A*, 1994, 49: 4101-4109. DOI: 10.1103/PhysRevA.49.4101.

BIBLIOGRAPHY

- [54] Holland M J, Burnett K. Interferometric detection of optical phase shifts at the heisenberg limit [J]. *Phys. Rev. Lett.*, 1993, 71: 1355-1358.
- [55] Lücke B, Scherer M, Kruse J, et al. Twin matter waves for interferometry beyond the classical limit[J/OL]. *Science*, 2011, 334(6057): 773-776. DOI: 10.1126/science.1208798.
- [56] Luo X Y, Zou Y Q, Wu L N, et al. Deterministic entanglement generation from driving through quantum phase transitions[J]. *Science*, 2017, 355(6325): 620-623.
- [57] Lange K, Peise J, Lücke B, et al. Entanglement between two spatially separated atomic modes [J]. *Science*, 2018, 360(6387): 416-418.
- [58] Andrews M, Townsend C, Miesner H J, et al. Observation of interference between two bose condensates[J]. *Science*, 1997, 275(5300): 637-641.
- [59] Shin Y, Saba M, Pasquini T, et al. Atom interferometry with bose-einstein condensates in a double-well potential[J]. *Phys. Rev. Lett.*, 2004, 92(5): 050405.
- [60] Albiez M, Gati R, Fölling J, et al. Direct observation of tunneling and nonlinear self-trapping in a single bosonic josephson junction[J]. *Phys. Rev. Lett.*, 2005, 95(1): 010402.
- [61] Anderson B P, Kasevich M A. Macroscopic quantum interference from atomic tunnel arrays [J]. *Science*, 1998, 282(5394): 1686-1689.
- [62] Cataliotti F, Burger S, Fort C, et al. Josephson junction arrays with bose-einstein condensates [J]. *Science*, 2001, 293(5531): 843-846.
- [63] Hagley E W, Deng L, Kozuma M, et al. Measurement of the coherence of a Bose-Einstein condensate[J]. *Phys. Rev. Lett.*, 1999, 83(16): 3112.
- [64] Stenger J, Inouye S, Chikkatur A P, et al. Bragg spectroscopy of a bose-einstein condensate[J]. *Phys. Rev. Lett.*, 1999, 82(23): 4569.
- [65] Bloch I, Hänsch T W, Esslinger T. Measurement of the spatial coherence of a trapped Bose gas at the phase transition[J]. *Nature*, 2000, 403(6766): 166.
- [66] Dettmer S, Hellweg D, Ryytty P, et al. Observation of phase fluctuations in elongated bose-einstein condensates[J]. *Phys. Rev. Lett.*, 2001, 87(16): 160406.
- [67] Greiner M, Bloch I, Mandel O, et al. Exploring phase coherence in a 2d lattice of bose-einstein condensates[J]. *Phys. Rev. Lett.*, 2001, 87(16): 160405.
- [68] Hofferberth S, Lesanovsky I, Fischer B, et al. Non-equilibrium coherence dynamics in one-dimensional Bose gases[J]. *Nature*, 2007, 449(7160): 324.
- [69] Kitagawa T, Imambekov A, Schmiedmayer J, et al. The dynamics and prethermalization of one-dimensional quantum systems probed through the full distributions of quantum noise[J]. *New J. Phys.*, 2011, 13(7): 073018.
- [70] Cirac J, Gardiner C, Naraschewski M, et al. Continuous observation of interference fringes from bose condensates[J]. *Phys. Rev. A*, 1996, 54(5): R3714.
- [71] Castin Y, Dalibard J. Relative phase of two Bose-Einstein condensates[J]. *Phys. Rev. A*, 1997, 55: 4330-4337.
- [72] Wright E M, Walls D, Garrison J. Collapses and revivals of bose-einstein condensates formed in small atomic samples[J]. *Phys. Rev. Lett.*, 1996, 77(11): 2158.

BIBLIOGRAPHY

- [73] Villain P, Lewenstein M, Dum R, et al. Quantum dynamics of the phase of a bose–einstein condensate[J]. *J Mod Opt*, 1997, 44(10): 1775-1799.
- [74] Sinatra A, Castin Y. Phase dynamics of bose-einstein condensates: Losses versus revivals[J]. *The European Physical Journal D-Atomic, Molecular, Optical and Plasma Physics*, 1998, 4(3): 247-260.
- [75] Sinatra A, Castin Y, Witkowska E. Coherence time of a bose-einstein condensate[J]. *Phys. Rev. A*, 2009, 80: 033614.
- [76] Castin Y, Sinatra A. Spatial and temporal coherence of a bose-condensed gas[M]. Berlin, Heidelberg: Springer Berlin Heidelberg, 2013: 315-339.
- [77] Graham R. Decoherence of bose-einstein condensates in traps at finite temperature[J]. *Phys. Rev. Lett.*, 1998, 81(24): 5262.
- [78] Castin Y, Sinatra A. Temps de cohérence d’un condensat de bose–einstein dans un gaz isolé harmoniquement piégé[J/OL]. *Comptes Rendus Physique*, 2018, 19(5): 316–336. <http://dx.doi.org/10.1016/j.crhy.2018.04.001>.
- [79] Hall D S, Matthews M R, Wieman C E, et al. Measurements of relative phase in two-component bose-einstein condensates[J]. *Phys. Rev. Lett.*, 1998, 81(8): 1543.
- [80] Egorov M, Anderson R P, Ivannikov V, et al. Long-lived periodic revivals of coherence in an interacting bose-einstein condensate[J/OL]. *Phys. Rev. A*, 2011, 84: 021605(R). <https://link.aps.org/doi/10.1103/PhysRevA.84.021605>.
- [81] Ivannikov V, Sidorov A I. Phase diffusion in trapped-atom interferometers[J]. *J. Phys. B: At. Mol. Opt. Phys.*, 2018, 51(20): 205002.
- [82] Deutsch C, Ramirez-Martinez F, Lacroûte C, et al. Spin self-rephasing and very long coherence times in a trapped atomic ensemble[J]. *Phys. Rev. Lett.*, 2010, 105(2): 020401.
- [83] Sortais Y, Bize S, Nicolas C, et al. Cold collision frequency shifts in a 87 rb atomic fountain[J]. *Phys. Rev. Lett.*, 2000, 85(15): 3117.
- [84] Köhl M, Hänsch T W, Esslinger T. Measuring the temporal coherence of an atom laser beam [J/OL]. *Phys. Rev. Lett.*, 2001, 87: 160404. <https://link.aps.org/doi/10.1103/PhysRevLett.87.160404>.
- [85] Lewandowski H J, Harber D M, Whitaker D L, et al. Observation of anomalous spin-state segregation in a trapped ultracold vapor[J/OL]. *Phys. Rev. Lett.*, 2002, 88: 070403. <https://link.aps.org/doi/10.1103/PhysRevLett.88.070403>.
- [86] Solaro C, Bonnin A, Combes F, et al. Competition between spin echo and spin self-rephasing in a trapped atom interferometer[J/OL]. *Phys. Rev. Lett.*, 2016, 117: 163003. <https://link.aps.org/doi/10.1103/PhysRevLett.117.163003>.
- [87] Kleine Büning G, Will J, Ertmer W, et al. Extended coherence time on the clock transition of optically trapped rubidium[J/OL]. *Phys. Rev. Lett.*, 2011, 106: 240801. <https://link.aps.org/doi/10.1103/PhysRevLett.106.240801>.
- [88] Jones S J, Wiseman H M, Doherty A C. Entanglement, einstein-podolsky-rosen correlations, bell nonlocality, and steering[J/OL]. *Phys. Rev. A*, 2007, 76: 052116. <https://link.aps.org/doi/10.1103/PhysRevA.76.052116>.

BIBLIOGRAPHY

- [89] Bennett C H, Brassard G, Crépeau C, et al. Teleporting an unknown quantum state via dual classical and einstein-podolsky-rosen channels[J]. *Phys. Rev. Lett.*, 1993, 70: 1895-1899.
- [90] Estève J, Gross C, Weller A, et al. Squeezing and entanglement in a Bose-Einstein condensate [J/OL]. *Nature*, 2008, 455: 1216. DOI: 10.1038/nature07332.
- [91] Bookjans E M, Hamley C D, Chapman M S. Strong quantum spin correlations observed in atomic spin mixing[J/OL]. *Phys. Rev. Lett.*, 2011, 107(21): 210406. DOI: 10.1103/PhysRevLett.107.210406.
- [92] Gross C, Strobel H, Nicklas E, et al. Atomic homodyne detection of continuous-variable entangled twin-atom states[J/OL]. *Nature*, 2011, 480(7376): 219-223. DOI: 10.1038/nature10654.
- [93] Bücker R, Grond J, Manz S, et al. Twin-atom beams[J/OL]. *Nature Physics*, 2011, 7: 608-611. DOI: 10.1038/nphys1992.
- [94] Lücke B, Peise J, Vitagliano G, et al. Detecting multiparticle entanglement of dicke states[J/OL]. *Phys. Rev. Lett.*, 2014, 112: 155304. <https://link.aps.org/doi/10.1103/PhysRevLett.112.155304>.
- [95] Hamley C D, Gerving C S, Hoang T M, et al. Spin-nematic squeezed vacuum in a quantum gas [J/OL]. *Nature Phys.*, 2012, 8: 305. DOI: 10.1038/nphys2245.
- [96] Behbood N, Ciurana F M, Colangelo G, et al. Generation of macroscopic singlet states in a cold atomic ensemble[J/OL]. arXiv:1403.1964v2, 2014. <http://arxiv.org/abs/1403.1964v2>.
- [97] Schleier-Smith M H, Leroux I D, Vuletić V. States of an ensemble of two-level atoms with reduced quantum uncertainty[J]. *Phys. Rev. Lett.*, 2010, 104(7): 073604.
- [98] Sewell R J, Koschorreck M, Napolitano M, et al. Magnetic sensitivity beyond the projection noise limit by spin squeezing[J]. *Phys. Rev. Lett.*, 2012, 109: 253605.
- [99] Bohnet J G, Cox K C, Norcia M A, et al. Reduced back-action for phase sensitivity 10 times beyond the standard quantum limit[J/OL]. arXiv:1310.3177, 2013. <http://arxiv.org/abs/1310.3177>.
- [100] Wasilewski W, Jensen K, Krauter H, et al. Quantum noise limited and entanglement-assisted magnetometry[J]. *Phys. Rev. Lett.*, 2010, 104(13): 133601.
- [101] Muessel W, Strobel H, Linnemann D, et al. Scalable Spin Squeezing for Quantum-Enhanced Magnetometry with Bose-Einstein Condensates[J]. *Phys. Rev. Lett.*, 2014, 113(10): 103004.
- [102] Böhi P, Riedel M F, Hoffrogge J, et al. Coherent manipulation of Bose-Einstein condensates with state-dependent microwave potentials on an atom chip[J/OL]. *Nature Phys.*, 2009, 5: 592-597. DOI: 10.1038/nphys1329.
- [103] Riedel M F. Multi-particle entanglement on an atom chip[D/OL]. Ludwig-Maximilians-Universität, München, 2010. <http://nbn-resolving.de/urn:nbn:de:bvb:19-126195>.
- [104] Fadel M, Zibold T, Décamps B, et al. Spatial entanglement patterns and einstein-podolsky-rosen steering in bose-einstein condensates[J]. *Science*, 2018, 360(6387): 409-413.
- [105] Fadel M. Many-particle entanglement, einstein-podolsky-rosen steering and bell correlations in bose-einstein condensates[D]. University of Basel, 2018.

BIBLIOGRAPHY

- [106] Guo S F, Chen F, Liu Q, et al. Faster state preparation across quantum phase transition assisted by reinforcement learning[J/OL]. *Phys. Rev. Lett.*, 2021, 126: 060401. <https://link.aps.org/doi/10.1103/PhysRevLett.126.060401>.
- [107] Böhi P, Riedel M F, Hänsch T W, et al. Imaging of microwave fields using ultracold atoms[J/OL]. *Appl. Phys. Lett.*, 2010, 97(5): 051101. DOI: 10.1063/1.3470591.
- [108] Böhi P A. Coherent manipulation of ultracold atoms with microwave near-fields[D/OL]. Ludwig-Maximilians-Universität, München, 2010. <http://nbn-resolving.de/urn:nbn:de:bvb:19-120953>.
- [109] Schmied R, Bancal J D, Allard B, et al. Bell correlations in a Bose-Einstein condensate[J]. *Science*, 2016, 352(6284): 441-444.
- [110] Hoffrogge J. Mikrowellen-Nahfelder auf Atomchips[D]. Ludwig-Maximilians-Universität, München, 2007.
- [111] Steck D A. Rubidium 87 D line data[J/OL]. available online at <http://steck.us/alkalidata>, revision 2.1.4, 23 December 2010. <http://steck.us/alkalidata>.
- [112] Breit G, Rabi I I. Measurement of nuclear spin[J/OL]. *Phys. Rev.*, 1931, 38: 2082-2083. DOI: 10.1103/PhysRev.38.2082.2.
- [113] Anderson R. Nonequilibrium dynamics and relative phase evolution of two-component Bose-Einstein condensates[D/OL]. Swinburne University, Melbourne, 2010. <http://hdl.handle.net/1959.3/94427>.
- [114] Reinaudi G, Lahaye T, Wang Z, et al. Strong saturation absorption imaging of dense clouds of ultracold atoms[J/OL]. *Opt. Lett.*, 2007, 32: 3143. DOI: 10.1364/OL.32.003143.
- [115] Ockeloen C F, Tauschinsky A F, Spreeuw R J C, et al. Detection of small atom numbers through image processing[J/OL]. *Phys. Rev. A*, 2010, 82(6): 061606. DOI: 10.1103/PhysRevA.82.061606.
- [116] Ockeloen C F. Probing fluctuations in a lattice of mesoscopic atomic ensembles[D/OL]. University of Amsterdam, 2010. <http://dare.uva.nl/en/scriptie/365438>.
- [117] Muessel W, Strobel H, Joos M, et al. Optimized absorption imaging of mesoscopic atomic clouds[J/OL]. *Applied Physics B: Lasers and Optics*, 2013, 113: 69-73. DOI: 10.1007/s00340-013-5553-8.
- [118] Burt E A, Ghrist R W, Myatt C J, et al. Coherence, correlations, and collisions: What one learns about Bose-Einstein condensates from their decay[J]. *Phys. Rev. Lett.*, 1997, 79: 337-340.
- [119] Söding J, Guéry-Odelin D, Desbiolles P, et al. Three-body decay of a rubidium Bose-Einstein condensate[J]. *Appl. Phys. B*, 1999, 69(4): 257-261.
- [120] van Kempen E G M, Kokkelmans S J J M F, Heinzen D J, et al. Interisotope determination of ultracold rubidium interactions from three high-precision experiments[J/OL]. *Phys. Rev. Lett.*, 2002, 88: 093201. <https://link.aps.org/doi/10.1103/PhysRevLett.88.093201>.
- [121] Tojo S, Hayashi T, Tanabe T, et al. Spin-dependent inelastic collisions in spin-2 bose-einstein condensates[J/OL]. *Phys. Rev. A*, 2009, 80: 042704. <https://link.aps.org/doi/10.1103/PhysRevA.80.042704>.

BIBLIOGRAPHY

- [122] Geiger R. Senseur inertielle à ondes de matière aéroportée: 2011PA112207[D]. Université Paris Sud - Paris XI, 2011.
- [123] Sinatra A, Castin Y. Binary mixtures of bose-einstein condensates: Phase dynamics and spatial dynamics[J]. *The European Physical Journal D*, 2000, 8(3): 319.
- [124] Gibble K, Chu S. Laser-cooled cs frequency standard and a measurement of the frequency shift due to ultracold collisions[J/OL]. *Phys. Rev. Lett.*, 1993, 70: 1771-1774. <https://link.aps.org/doi/10.1103/PhysRevLett.70.1771>.
- [125] Rosenbusch P. Magnetically trapped atoms for compact atomic clocks[J/OL]. *Appl. Phys. B*, 2009, 95(2): 227-235. DOI: 10.1007/s00340-009-3451-x.
- [126] Dalibard J, Castin Y, Mølmer K. Wave-function approach to dissipative processes in quantum optics[J]. *Phys. Rev. Lett.*, 1992, 68: 580-583.
- [127] Carmichael H. *An Open Systems Approach to Quantum Optics*[M]. New York: Springer, 1991.
- [128] Matthews M R, Hall D S, Jin D S, et al. Dynamical response of a bose-einstein condensate to a discontinuous change in internal state[J/OL]. *Phys. Rev. Lett.*, 1998, 81: 243-247. <https://link.aps.org/doi/10.1103/PhysRevLett.81.243>.
- [129] Demkowicz-Dobrzański R, Czajkowski J, Sekatski P. Adaptive quantum metrology under general markovian noise[J]. *Phys. Rev. X*, 2017, 7(4): 041009.
- [130] Czajkowski J, Pawłowski K, Demkowicz-Dobrzański R. Many-body effects in quantum metrology[J]. *New J. Phys.*, 2019, 21(5): 053031.
- [131] Pawłowski K, Fadel M, Treutlein P, et al. Mesoscopic quantum superpositions in bimodal Bose-Einstein condensates: Decoherence and strategies to counteract it[J/OL]. *Phys. Rev. A*, 2017, 95: 063609. <https://link.aps.org/doi/10.1103/PhysRevA.95.063609>.
- [132] Haine S A, Lau J, Anderson R P, et al. Self-induced spatial dynamics to enhance spin squeezing via one-axis twisting in a two-component bose-einstein condensate[J/OL]. *Phys. Rev. A*, 2014, 90: 023613. <https://link.aps.org/doi/10.1103/PhysRevA.90.023613>.
- [133] Schmied R, Treutlein P. Tomographic reconstruction of the Wigner function on the Bloch sphere [J]. *New J. Phys.*, 2011, 13(6): 065019.
- [134] Bienaimé T, Fava E, Colzi G, et al. Spin-dipole oscillation and polarizability of a binary bose-einstein condensate near the miscible-immiscible phase transition[J]. *Phys. Rev. A*, 2016, 94: 063652.
- [135] Wineland D J, Bollinger J J, Itano W M, et al. Squeezed atomic states and projection noise in spectroscopy[J]. *Phys. Rev. A*, 1994, 50: 67-88.
- [136] Sørensen A, Duan L M, Cirac J I, et al. Many-particle entanglement with bose-einstein condensates[J]. *Nature*, 2001, 409: 63 EP -.
- [137] Sørensen A S, Mølmer K. Entanglement and extreme spin squeezing[J]. *Phys. Rev. Lett.*, 2001, 86: 4431-4434.
- [138] Werner R F. Quantum states with Einstein-Podolsky-Rosen correlations admitting a hidden-variable model[J]. *Phys. Rev. A*, 1989, 40: 4277-4281.
- [139] Gühne O, Tóth G. Entanglement detection[J]. *Phys. Rev*, 2009, 474(1): 1 - 75.

APPENDIX A TYPICAL TRAPS ON ATOM CHIP

Depending on the current configurations we can generate different types of magnetic traps based on the atom chip^[3]. Here we discuss typical magnetic trapping potentials that are used in our experiment.

A simplest wire trap can be created by combining an on-chip wire structure that carries DC current and a homogeneous bias field perpendicular to the wire. For example, a wire along x -direction carrying current I_x creates a magnetic field with concentric circular field lines whose centres lie on the wire. If an bias field B_y is applied along y -direction, fields will cancel at a distance from the wire,

$$z_0 = \frac{\mu_0 I}{2\pi B_y},$$

therefore form a two-dimensional quadrupole confinement in the yz plane. Note that in such a quadrupole trap atoms will suffer from the Majorana spin flips since the magnetic field at trap center $B_0 = 0$. The problem of the Majorana spin flips can be solved by removing the zero field at trap center with an additional homogeneous bias field B_x along x -direction. The resulted trap is called an *Ioffe-Pritchard trap*, providing two-dimensional quadratic confinement in the yz -plane, with $B_0 \neq 0$ at trap center.

To aim for a three-dimensional harmonic trap, we add another current along y direction, crossing the existing straight wire perpendicularly. The generated magnetic field will modulate the field on axis $z = z_0$ and provide an axial confinement along x -direction. Now we have a three-dimensional trap, which is generally called *Dimple trap*. Such Dimple traps can be describe as a harmonic potential

$$V = m(\omega_x^2 x^2 + \omega_y^2 y^2 + \omega_z^2 z^2)/2.$$

The new current along y -axis can be easily obtained by either bending the wire ends or adding additional crossing wires. In our experiment, the Dimple trap is formed by three central wires of the five-wire structure on the science chip and a crossing wire (named ‘Long-Ioffe’) in the lower gold layer. What is special about the three central wires is that, besides the static field, they constitutes a microwave co-planar wave guide with microwave connectors soldered onto the base chip (as shown in Figure 3.2). By using a bias tee to apply DC currents as well as the microwave current to these three wires, this particular tool provides the capability to create state-dependent potential (see in section 3.3).

Three-dimensional traps can also be created with “Z”-shape structures on chip. In this case the transverse confinement is provided by the central part of the “Z” wire in combination with the bias field, while the axial confinement comes from the bent wire parts. There are two Z-shape wire used in the experiment, which we refer to as a “IoffeZ” and “LongIoffe-Z” depending on the length for distinguishment.

let us now discuss the specific magnetic traps used over the experimental sequence. Their name and parameters are summarized in Table A.1, including the position of the trap minimum, the trap frequency, the magnetic field B_0 at trap center, the geometrically mean of the trap frequency $\hbar\omega_{ho}$, the critical temperature in the trap $k_B T_c^0$, the chemical potential μ_c , and the trap depth, in order to give an intuitive picture of how the atoms are transferred step by step during the sequence. Note that the trap minimum is with respect to the origin of coordinate system. These parameters are all from simulation rather than the experiment. The simulation is based on an atom chip simulation kit developed with MATLAB, see in reference^[3], and can be used to simulate all the chip-related traps.

Table A.1 Parameters of the traps

trap name	$(x, y, z)(\mu m)$	$(f_x, f_y, f_z)(kHz)$	$ B_0 (G)$	$\omega_{ho}(Hz)$	$k_B T_c^0(kHz)$	$\mu_c(kHz)$	depth(MHz)
Ioffe-1	[-1125, 0, 454]	[0.02, 0.06, 0.08]	9.6	42.3	2.66	1.12	134
Ioffe-2	[-1125, 0, 59]	[0.013, 4.4, 4.45]	2.3	633.8	27.6	16	30
Ioffe-3	[-1125, 0, 48]	[0.006, 1.8, 1.8]	2.1	271.6	11.8	5.87	9.5
LongIoffe-4	[-775, 0.5, 46]	[0.002, 1.87, 1.87]	2.03	191.2	8.3	3.67	6.4
Dimple-5	[-43, -4, 51]	[0.49, 2.26, 2.35]	2.26	1365.7	22	12.3	6.2
Dimple-6	[-5, -2, 45]	[0.2, 1.75, 1.78]	2.59	849	10.1	4.8	0.6
Dimple-7	[12, -1.8, 41]	[0.11, 0.71, 0.71]	3.229	387.3	3.63	1.42	0.1
Dimple-8	[12, -1.8, 41]	[0.11, 0.30, 0.30]	3.229	217.1	2.1	0.73	

“Ioffe” traps build a bridge between the very dilute optical molasses and the dense cloud in later tight magnetic traps. “Ioffe” traps are generated by a current on a Z-shaped wire (named Ioffe-Z) which lies on the lower layer of the science chip. The quadratic confinement in transverse direction comes from the combination of the central part of the wire, carrying $I_{Ioffe-Z}$ and a static field B_y . Axial confinement is provided by the bent parts of Ioffe-Z wire. Similar to Ioffe traps, the “LongIoffe” trap is generated by another longer Z-shaped wire (Long Ioffe-Z wire).

“Dimple” traps are the most important traps in our experiment, since they are where the evaporative cooling and main experiments takes place. Dimple-5 is where the first

RF ramp takes place, with a trap depth of Hz and an exponential RF ramp from $14 \rightarrow 2.2 \text{ MHz}$ during 2 s . We then transfer atoms to the ‘Dimple-6’ to perform the second RF ramp from $2.2 \rightarrow 1.84 \text{ MHz}$ during 1 s . Here we already have a BEC but not as cold as desired. To further cool down the atoms, we transfer the BEC to ‘Dimple-7’ and apply a RF pulse with a frequency at approximately 2.27 MHz , which can be tuned to determine the temperature and atom number in the final BEC. It is particularly interesting to compare the scales of energy in the Dimple traps where the evaporative cooling takes place. In Table A.2 we compare the following parameters in the unit of frequency: the starting frequency and stop frequency of the RF ramp, the trap frequency, the geometrically mean of the trap frequency $\hbar\omega_{\text{ho}}$, the critical temperature in unit of kHz and nanoKelvin, and the trap depth.

Table A.2 RF ramps and parameters of relevant traps during the evaporative cooling

RF Ramp	happen in trap	ω_{ho} (Hz)	$k_B T_c^0$ (kHz)	T_c^0 (nK)	trap depth (MHz)
RF-1: $14 \text{ MHz} \rightarrow 2.2 \text{ MHz}$	Dimple-5	1365.7	22	1050	6.2
RF-2: $2.2 \text{ MHz} \rightarrow 1.84 \text{ MHz}$	Dimple-6	849	10.1	500	0.63
RF-3: 2.27 MHz	Dimple-7	387.3	3.63	174	0.1

Dimple-7 is also the final trap where the main science sequence takes place. Transverse confinement comes from ‘‘Long-Ioffe’’ carrying $I_L = 180 \text{ mA}$ in x-direction plus a static field $B_y = 7.2 \text{ G}$. Longitudinal confinement is provided by the ‘‘Dimple’’ wires carrying $I_{\text{D,left}} = 2 \text{ mA}$, $I_{\text{D,signal}} = 2 \text{ mA}$, $I_{\text{D,right}} = -2 \text{ mA}$ each. The sign represent the direction of the current and a minus sign means the current is sent along $-y$ direction. An additional bias field $B_x = 3.2 \text{ G}$ along X direction is added to remove the zero field at trap center. Under these parameters, the final trap is an elongated cigar-shaped trap with trap frequencies $\omega_{(x,y,z)} = 2\pi \times (114, 714, 714) \text{ Hz}$. It gives us the convenience to treat the condensate as a three-dimensional BEC in a cylindrical coordinates, as done in our GPE simulations. The purpose of asymmetry in the I_{D} currents is to locate the trap on one side of the co-planar wave guide, in this way the atoms experience a gradient when microwave currents are sent through the central wire.

In our experiments, it is interesting to relax the final trap to the achieve weaker interactions. Therefore we have another experiment trap Dimple-8, created by the same structures with $I_L = 80 \text{ mA}$, $B_y = 3.2 \text{ G}$ and $I_{\text{D,left}} = 2 \text{ mA}$, $I_{\text{D,signal}} = 2 \text{ mA}$, $I_{\text{D,right}} = -2 \text{ mA}$. The trap frequency is $\omega_{(x,y,z)} = 2\pi \times (113, 301, 301) \text{ Hz}$. Note that, the Long-Ioffe current I_L and the bias field B_y are decreased simultaneously, in order to

keep the ratio of the two fixed ($B_y/I_L = 40 \text{ G/A}$, same as that in Dimple-7), so that the distance between the trap center and the chip does not change.

APPENDIX B ENTANGLEMENT DEPTH

In many-body systems, entanglement can be reflected by criteria such as entanglement depth. Entanglement depth describes the smallest number of particles in a partition of the system, in which each atom can be proven to be entangled with one another. It indicates the separability of the state with respect to partitions, although it's still controversial whether it makes statement about the strength of entanglement. In our experiment, the spin squeezing indicates the presence of entanglement between atoms. Usually we quantify the depth of entanglement based on the Wineland squeezing parameter ξ^2 , following the strategy Sørensen and Mølmer developed in Ref. [137].

We assume that in the system there exists a partition containing k entangled spins. Sørensen and Mølmer found that there is a minimum value that ξ^2 that can be achieved, and therefore, the observation of a ξ^2 below this minimum value indicates that there must be another partition in the system that containing more than k spins that are entangled. For convenience we define the frame such that the state is oriented with the optimized squeezed angle is along z direction. The problem is to derive the entanglement depth k of the state, knowing experimentally $\text{Var} [\hat{S}_z]$ and $\langle \hat{S}_x \rangle$, both experimentally measured quantities.

The strategy, following that paper, is the following. For integer spins $S = k/2$ (with even k), the state minimizing $\text{Var} [S_z]$ for a given $\langle S_x \rangle$ has vanishing $\langle S_y \rangle$ and $\langle S_z \rangle$, and therefore is also minimizing the second moment $\langle S_z^2 \rangle$. For this reason, this state can be found by minimizing

$$\mu \langle S_x \rangle + \langle S_z^2 \rangle, \quad (\text{B.1})$$

where μ is the Lagrange multiplier constraining the value of $\langle S_x \rangle$. Numerically the approach consists in diagonalizing the operator $\mu S_x + S_z^2$ for different μ 's. The resulting eigenvector associated to the smallest eigenvalue is the state of interest, which is used to evaluate the mean spin length $\langle S_x \rangle$ and the corresponding bound on the second moment $\langle S_z^2 \rangle$. If the experimentally determined spin variance is smaller than this bound, then there are more than k entangled particles in the system, and the procedure can be iterated with the next integer spins until the measured variance is above the bound. The case of half-integer spins (odd k) is more subtle, since the state minimizing $\langle S_z^2 \rangle$ is not minimizing $\text{Var} [S_z]$, and we will not discuss it here.

In Figure 5.5, the convex lines are obtained as described, by plotting the minimum variance $\text{Var} [S_z]$ attainable for different k and $\langle S_x \rangle$. Note that for a given point in the plot there is a minimum $S = k/2$ for which it is allowed. This provides a graphical method to find the entanglement depth of a many-body system, from given experimental measured ξ^2 .

ACKNOWLEDGEMENTS

博士生涯即将结束，至此五年寒暑辛劳都随风去，感恩有机会一窥险峰之高，身是恒河沙中一粒，但见过星河浩淼，便是幸运。五年的科研经历充满挑战，也不乏激动人心的时刻。求学期间承蒙许多老师与同学的指导与帮助，在此衷心表示感谢。

首先要感谢我的导师唐传祥教授对我的精心指导。唐老师为我提供了宽松的科研环境，鼓励我追寻自己所热爱的研究方向，在我研究进展不顺利时予我鼓励，在我取得成绩时勉励我更进一步。从本科毕设到博士生涯，与唐老师师徒六年的时间里，他始终处处为我的学术发展考虑，为我提供资源与帮助。作为一个学者，他严谨的治学态度，儒雅谦和的处世方式和对学生的爱护值得我终身学习。

感谢清华物理系的尤力教授，作为联合指导教师，他是我在学术道路上主要的领路人。尤老师具有开阔的学术视野，对物理有着深刻理解，他对科学研究的热情，以及乐观的性格始终影响着我。

本文的主要工作在巴塞尔大学完成。感谢中国留学基金委在我访学期间给予我的资金支持。在瑞士巴塞尔大学物理系进行联合培养的两年多的时间里，我在冷原子实验方面获得了宝贵的研究经验。我想借此机会真诚地感谢那些对论文中的工作做出贡献的人。首先我要感谢我访问期间的指导老师 Philipp Treutlein 教授，他在我的教育和生活中给予了我不断的支持。他是一位优秀的科学家，具有强烈的创新精神和对于物理的敏锐直觉。我们可以从他身上学到很多优秀的品质，但最宝贵的还要属他对物理的无限热情。

另外要感谢在巴塞尔大学物理系联合培养期间的团队成员，Tilman Zibold 博士，Matteo Fadel 博士，Boris Décamps 博士和 Paolo Colciaghi 的贡献。作为实验室的高级研究员，Tilman 经验丰富，知识渊博，如果没有他丰富的实验经验，我们的工作进展不会如此顺利。他对待研究工作总是严谨而诚实，这种品质也深深影响着我。同样要感谢 Matteo 和 Boris，他们都为本文中的实验工作做出了贡献，尤其是 Boris，他在早期为退相干机制方面研究打下了基础。我从这些早期的团队成员身上学到了大量的知识和实验技能，与他们的讨论也让我受益匪浅。我还要感谢我的师弟 Paolo，与他共同工作的两年中，我们在实验室中取长补短，他良好的幽默感也为我们的科研生活增色不少。我还要感谢我访问期间的所有同事的支持和帮助。另外，我要特别感谢我们的理论合作者 Krzysztof Pawłowski 博士，如果没有和他的合作，没有那些在线讨论和大量的电子邮件，我们也无法如此深入地理

ACKNOWLEDGEMENTS

解实验系统中发生的物理现象。我也要感谢 Alice Sinatra, 与她的讨论也使人受益匪浅。

另外我还要感谢在 You Lab 工作期间, 对我给予过帮助和支持的郑盟锟副教授与刘永椿副教授。在郑老师的指导下我初步接触了冷原子实验并习得了相关的电子学、光学的技能。在刘老师的支持下我完成了自己的第一个实验工作, 积累了实验技能。感谢在磁力计实验室与我共同工作过的刘贝、许安宁、鲍亦澄等人, 以及 You Lab 共事过的全体老师和同学的帮助和支持。

最后, 感谢我的父母和妹妹, 感谢我的挚友们, 家庭的温暖和朋友的爱永远给我最大的勇气。感谢我的恋人李相良, 总是尊重我、支持我、鼓励我, 与你在一起的时光总是充满快乐。

The past five years of my Ph.D. have been a challenging, exciting, wonderful as well as unforgettable experience for me. I started my Ph.D. program in Department of Engineering Physics, Tsinghua University in 2016. I was soon attracted by the beauty of ultracold atom experiments and made up my mind to change my topic to the field of quantum metrology. Therefore I joined the group of Prof. Li You and worked there for two years, mainly on a magnetometer project. Since August 2018, I joined the research group of Prof. Philipp Treutlein in the university of Basel as a visiting Ph.D. student with the support from the Chinese Scholarship Council, and stayed there for more than two years, during which I carried out the experiments presented in this dissertation. In this five-year journey, there are many people who have contributed to my education and life, who I would like to take this customary opportunity to sincerely acknowledge.

First and foremost, I would like to acknowledge my advisor Prof. Chuanxiang Tang, who has encouraged me to pursue my research interest and was always open to whatever decision I made that might benefit the development of my academic career. His rigorous attitude on research and his modest personality also deserve admiration.

I would like to thank my co-advisor Prof. Li You, who has a broad academic vision and a insightful, high-level view about the field. His enthusiasm for scientific research and his optimistic personality have always influenced me.

I would like to acknowledge my supervisor Prof. Philipp Treutlein in the University of Basel, for providing me with a terrific chance to carry out experiments and get trained in his research group. He has given me constant support both in the project and also in my life during my time in Basel. He is an excellent scientist who is innovative and possesses a good intuition, and as a supervisor he is extremely kind and supportive. There are a lot of

ACKNOWLEDGEMENTS

good qualities one can learn from him, but nothing is more precious than his inexhaustible enthusiasm for physics.

I would like to acknowledge the contribution of our team members in the BEC lab in Treutlein group. I am grateful to Dr. Tilman Zibold, who is a very experienced and knowledgeable senior scientist. Without his rich experience in the lab, our experiment would not have progressed as smoothly as it did. He is also honest and direct, and has shown me how important those qualities are for performing good research. Same gratitude goes to Dr. Matteo Fadel and Dr. Boris Décamps, who had made contributions to the work. In fact Boris is the one who has kickstarted the preliminary work of the research on the phase coherence in our system. I have learned volume of knowledge and experimental skills from these pioneer researchers and the discussions with them are always beneficial. I'd like to thank Paolo Colciaghi who joined the team several months later than me. We have performed lots of measurements together and learned from each other in the lab. I also appreciate his good sense of humor, since his jokes saved a lot of days when the experimental set up also tried to make jokes with us.

It is also my honor to collaborate with Dr. Krzysztof Pawłowski, a brilliant theoretical physicist and a good friend of our group. I would not have understood the physics in our system so deep without the theoretical discussion with him. I appreciate all the Skype meetings and volumes of Emails during the collaboration. I am also thankful to Alice Sinatra for the luminous discussions in Paris and for the power of role model she provided as a female scientist.

I would like to acknowledge all my colleagues in the Treutlein group during my stay in Basel. Those days we spent together on mountains discussing interesting physics and the time we spent talking besides or in the Rhine, or playing frisbee in the park, will all become precious memory.

During the first two years of my Ph.D program in Tsinghua University, I have accumulated experimental experience in the You lab. Under the guidance of Prof. Meng Khoon Tey, I had a first glance into the cold atom experiment and immediately got attracted. I acquired relevant skills on electronics and optics, and carried out my first experimental project (although not presented in this thesis) with the support of Prof. Yongchun Liu. I would like to thank them for their help and support. I would like to thank Dr. Bei Liu, Anning Xu and Yicheng Bao, who worked together with me in the the magnetometer lab, as well as all the other colleagues in You Lab for their help and support.

ACKNOWLEDGEMENTS

Finally I would like to acknowledge my parents, Chaodong Li and Yunyue Bai, and my sister Yilin Li, whose love always supports me no matter where I am. I hope that they will be at least a little bit proud of me. I would like to thank Xiangliang Li for sharing my life. He is not only my partner and my best friend, but also a physicist I admire. For over four years in the past, we have been experiencing our Ph.D. time together, and I have witnessed his passion for physics, his intelligence and all his hard work. I thank him for his constant support and love for me.

声 明

本人郑重声明：所提交的学位论文，是本人在导师指导下，独立进行研究工作所取得的成果。尽我所知，除文中已经注明引用的内容外，本学位论文的研究成果不包含任何他人享有著作权的内容。对本论文所涉及的研究工作做出贡献的其他个人和集体，均已在文中以明确方式标明。

签 名： 李奕瑶 日 期： 2021.6.21

个人简历、发表的学术论文与科研成果

个人简历

1994年10月21日出生于河南省西峡县。

2012年9月考入清华大学工程物理系工程物理专业，2016年7月本科毕业并获得工学学士学位。

2016年9月免试进入清华大学工程物理系攻读核科学与技术博士学位至今。

在学期间完成的相关学术成果

学术论文:

- [1] Y. Li, K. Pawłowski, B. Décamps, P. Colciaghi, M. Fadel, P. Treutlein, and T. Zibold, Fundamental limit of phase coherence in two-component Bose-Einstein condensates[J]. Physical Review Letters 125, 123402 (2020)

专利:

- [2] 刘永椿, 李奕璠, 尤力, 等. 基于磁致伸缩材料光学腔的精密磁场探测方法及系统: 中国, CN108896936B[P]. 2020-07-10.